

Multiscale Simulation of Polycrystals Mechanics

D. Raabe, F. Roters, S. Zaefferer, C. Zambaldi, E. Demir,
N. Zaafarani, M. Diehl, P. Eisenlohr

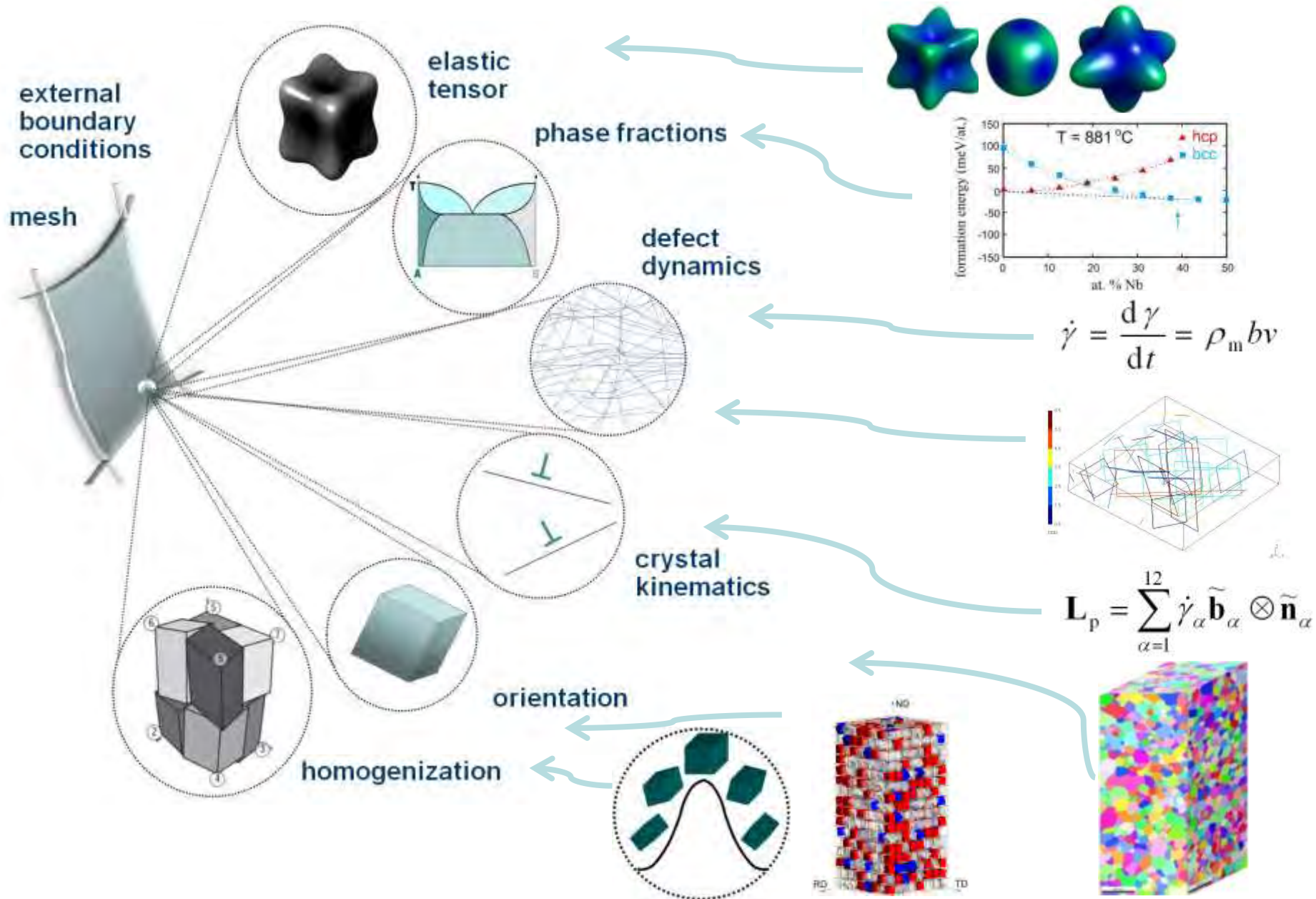
Max-Planck Institut für Eisenforschung
Düsseldorf, Germany

WWW.MPIE.DE
d.raabe@mpie.de



- **Multiscale Crystal Plasticity FEM**
- **Micrometer scale**
 - Indentation
- **Millimeter scale**
 - Grain boundaries
- **Macroscale**
 - Engineering forming simulations
- **Challenges**
 - Bauschinger effects
 - Damage initiation
 - Hybrid simulations
 - FFT solvers
 - Thermomechanical processing
- **Conclusions**

Multiscale crystal plasticity FEM



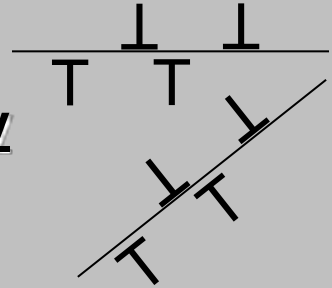


1

dyadic flow law based on dislocation rate theory

1. set
internal
variables

Taylor, Kocks, Mecking, Estrin, Kubin,...

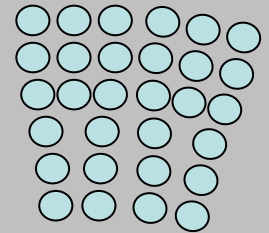


2

plastic gradients, size scale and orientation gradients (implicit)

2. set
internal
variables

Nye-Krüner,....

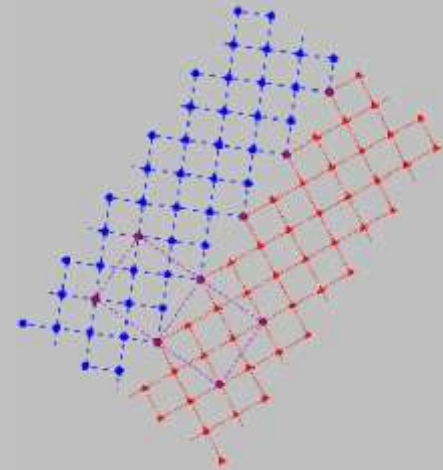


3

grain boundaries

3. set
internal
variables

activation concept:
energy of formation upon slip penetration: conservation law



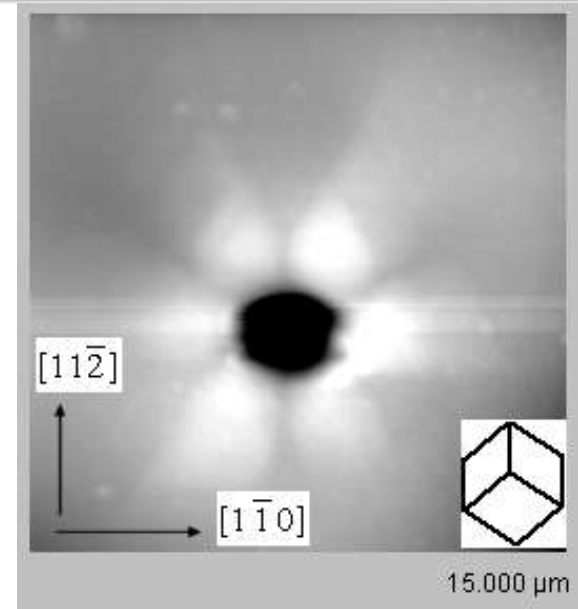
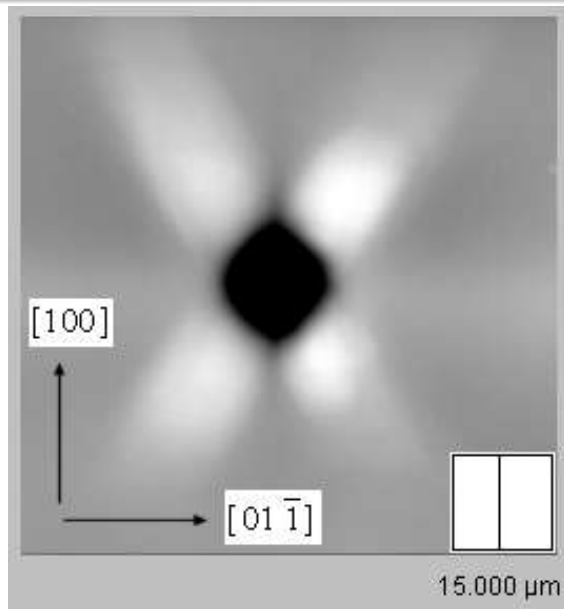
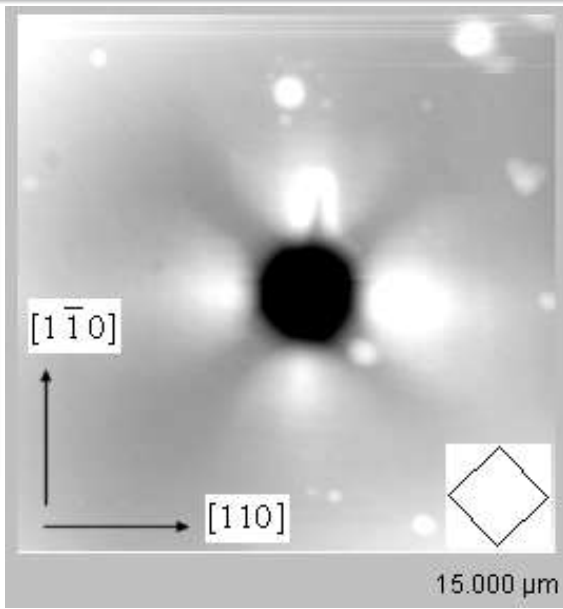


- **Multiscale Crystal Plasticity FEM**
- **Micrometer scale**
 - Indentation
- **Millimeter scale**
 - Grain boundaries
- **Macroscale**
 - Engineering forming simulations
- **Challenges**
 - Bauschinger effects
 - Damage initiation
 - Hybrid simulations
 - FFT solvers
 - Thermomechanical processing
- **Conclusions**

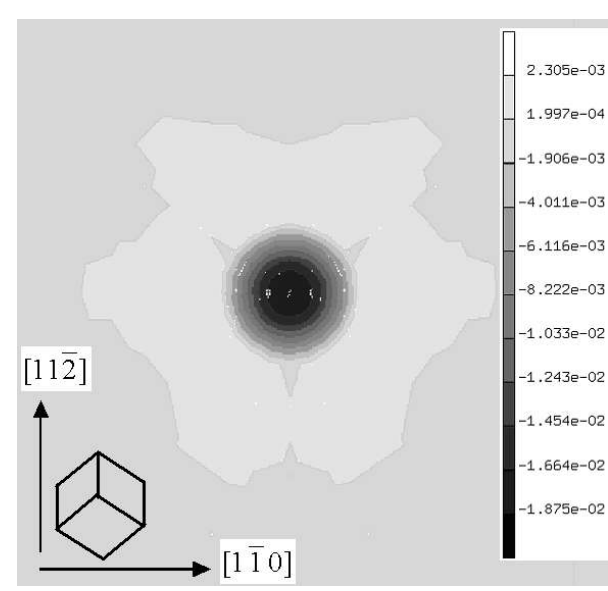
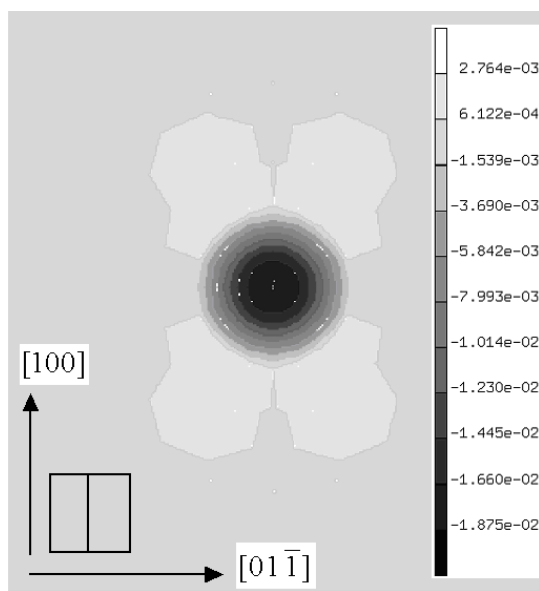
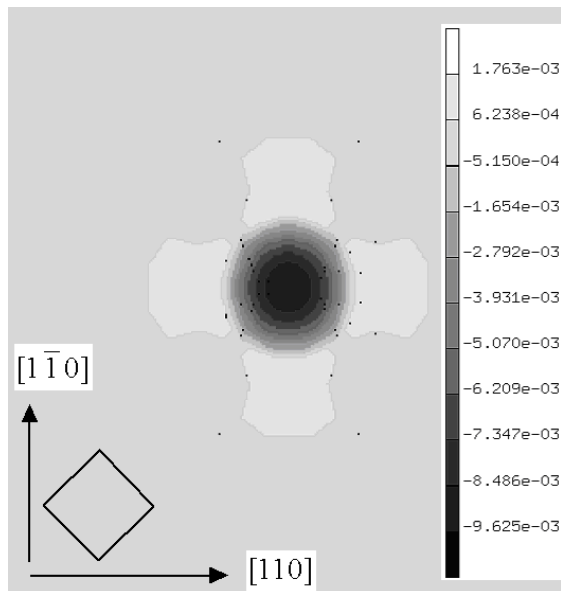
Nanoindentation – orientation dependence, Cu single crystals



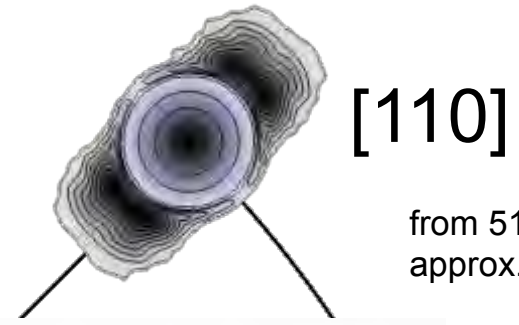
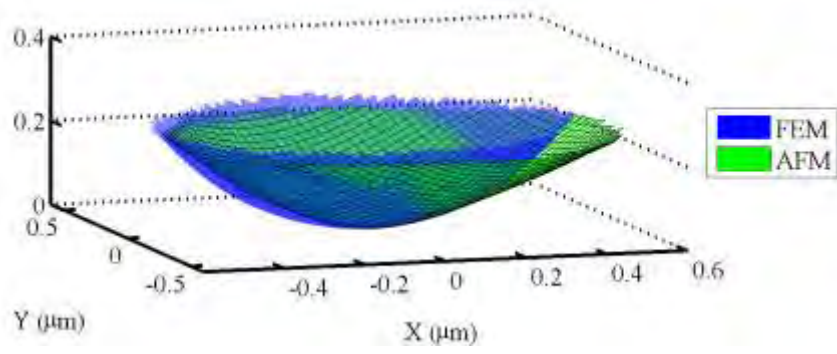
experiment



simulation



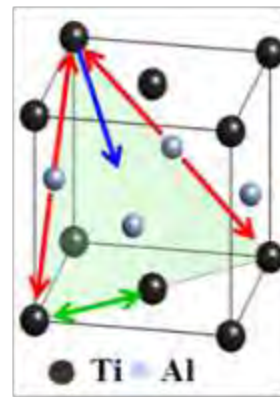
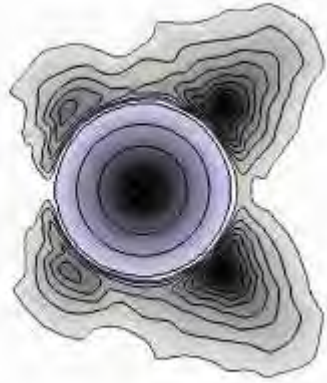
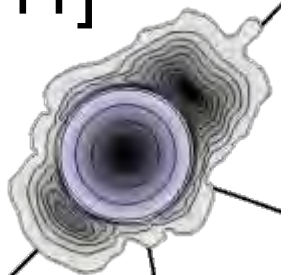
Plastic anisotropy of γ -TiAl: Simulated pile-up profiles



[110]

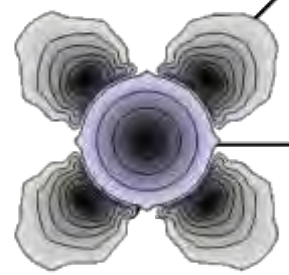
from 51 orientations
approx. resol. 9°

[111]

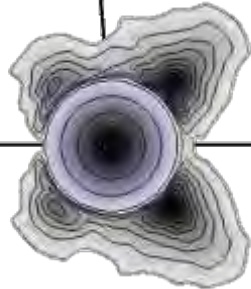


Pile-up IPF
High symmetry
orientations

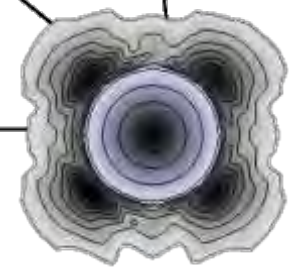
[001]



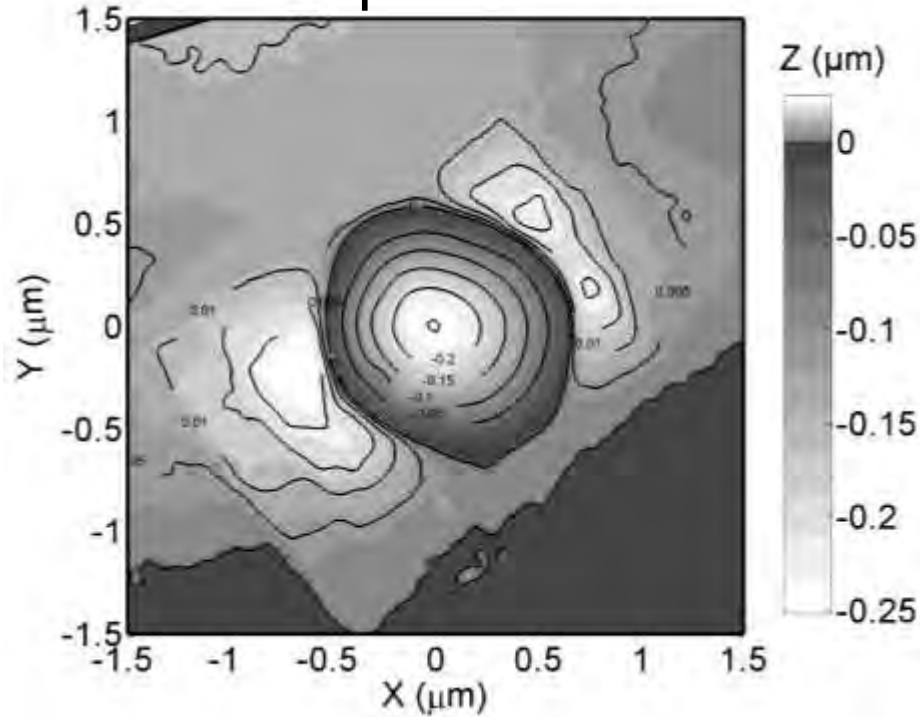
[101]



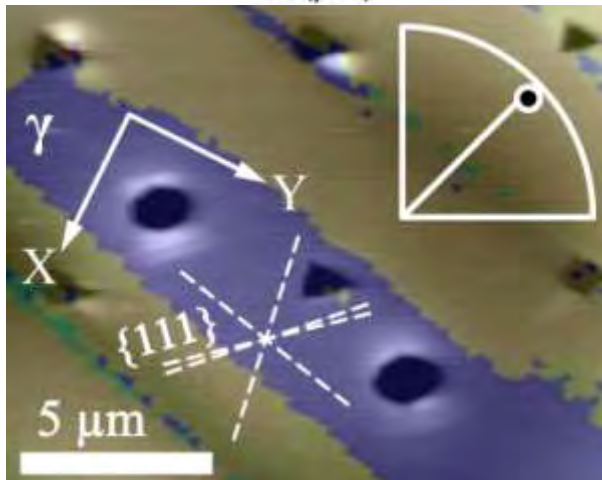
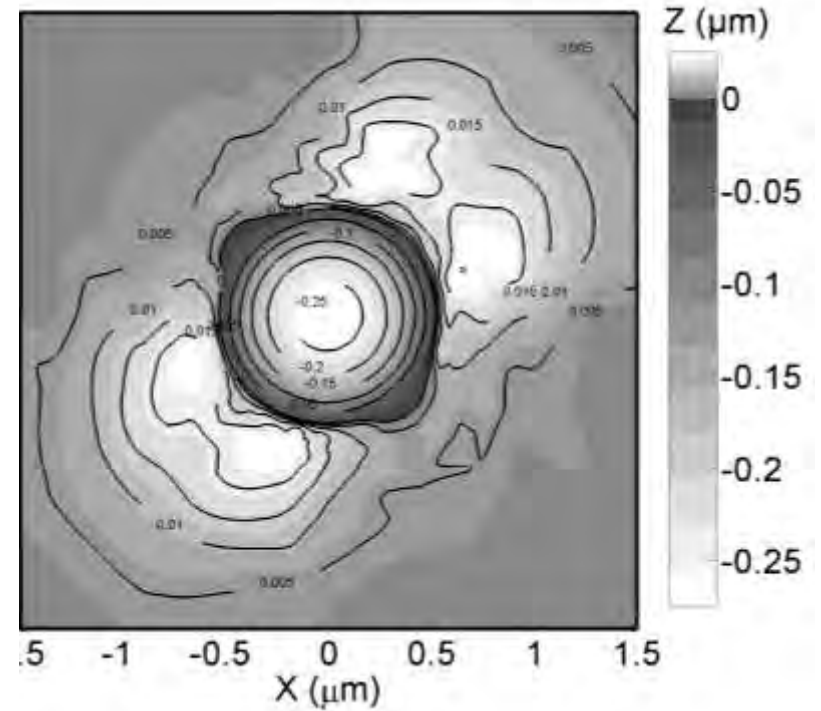
[100]

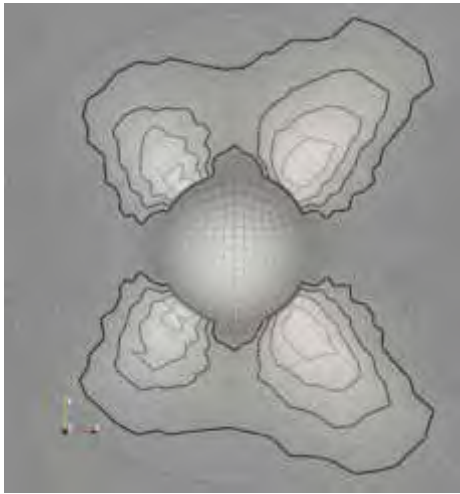


Experiment

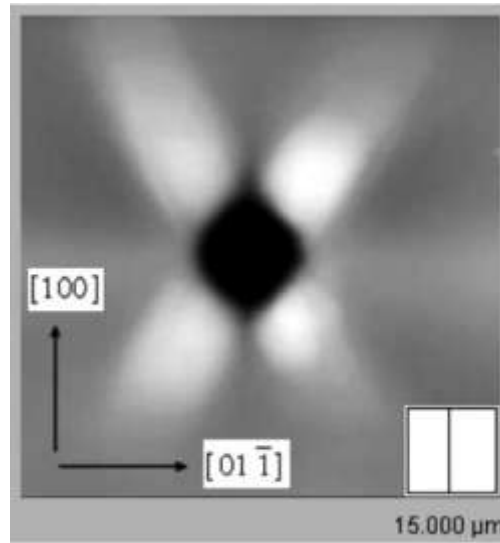


Simulation



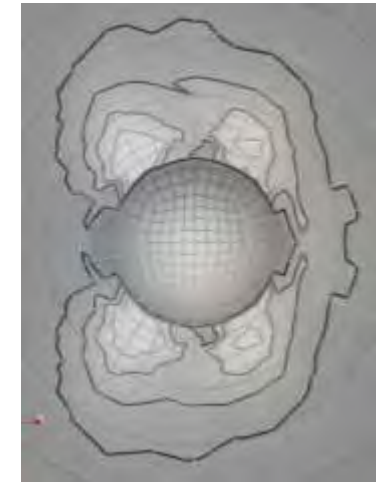


$$\tau_c^O / \tau_c^S < 1 \quad (\text{Ti-50Al})$$



$$\tau_c^O / \tau_c^S \approx 1$$

Cu, Al, Au, Ag, ...

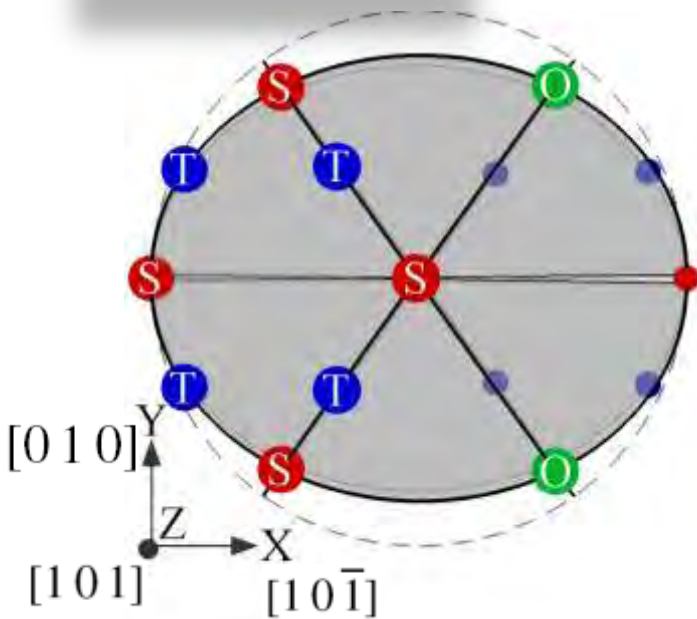
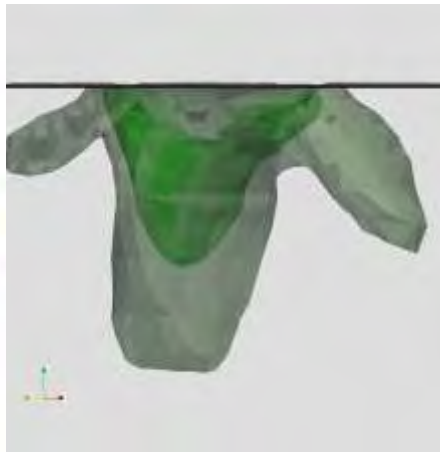
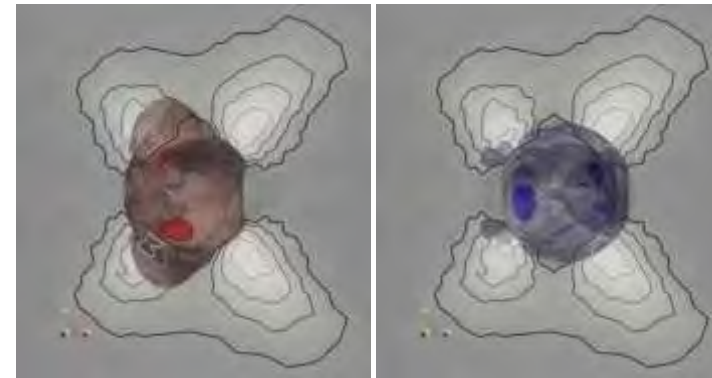
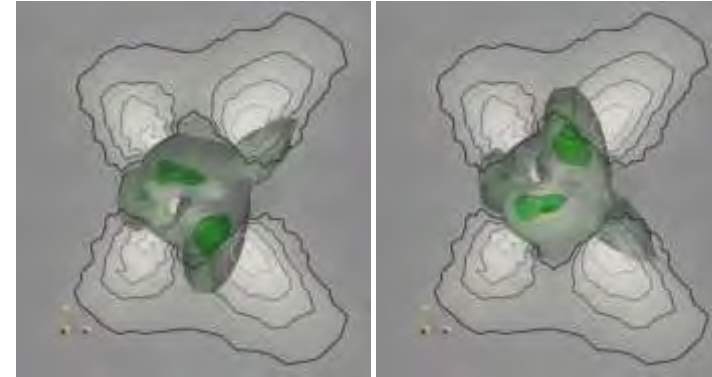
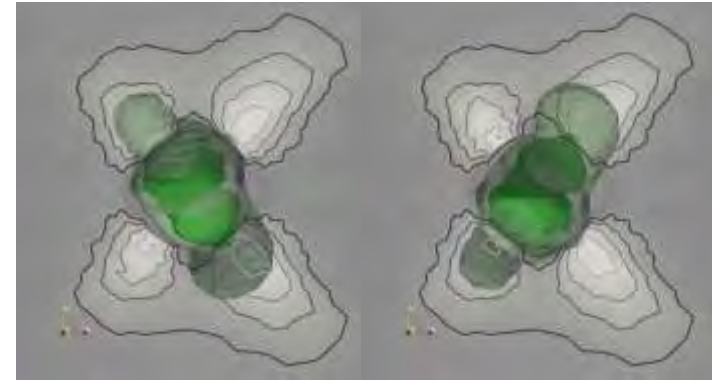
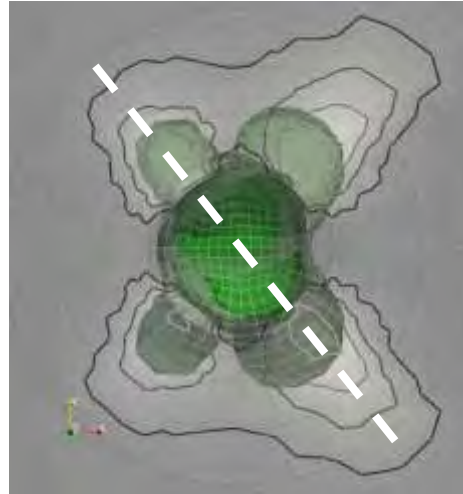
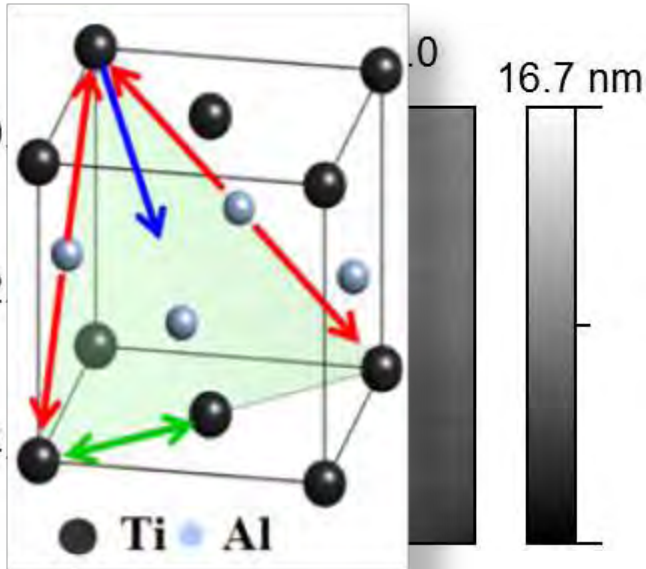


$$\tau_c^O / \tau_c^S > 1$$

Predicted
for Ti-55Al

[101] indentation indicates relative strengths of ordinary and super dislocation glide in TiAl

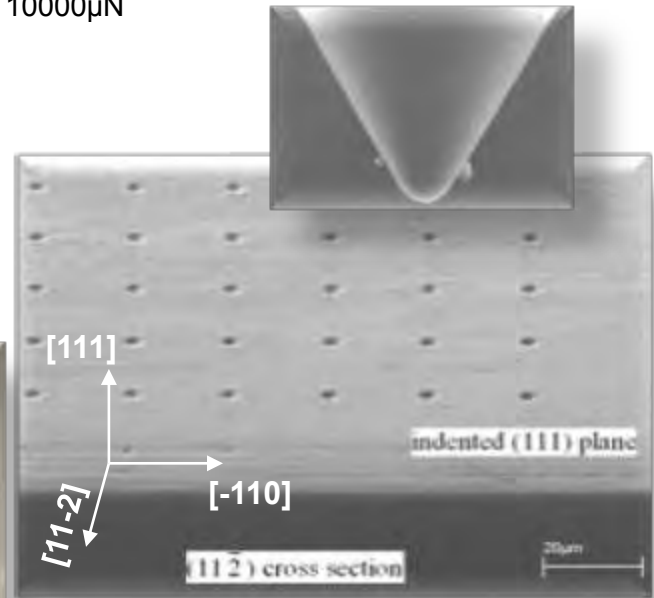
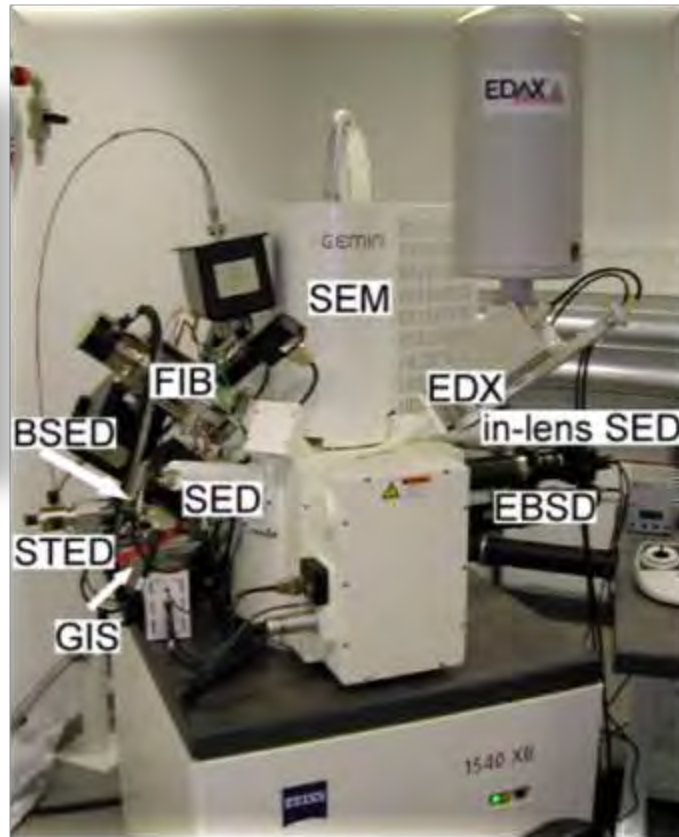
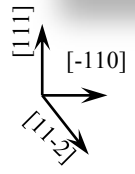
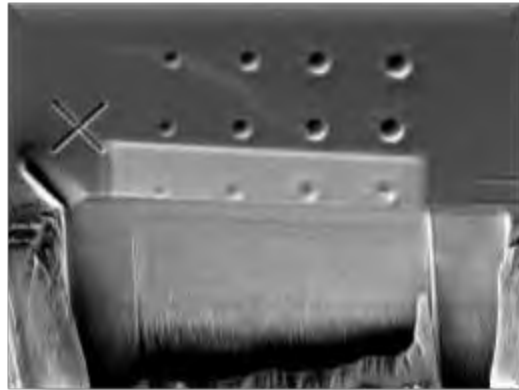
[101] indentation in γ -TiAl



3D microstructure analysis



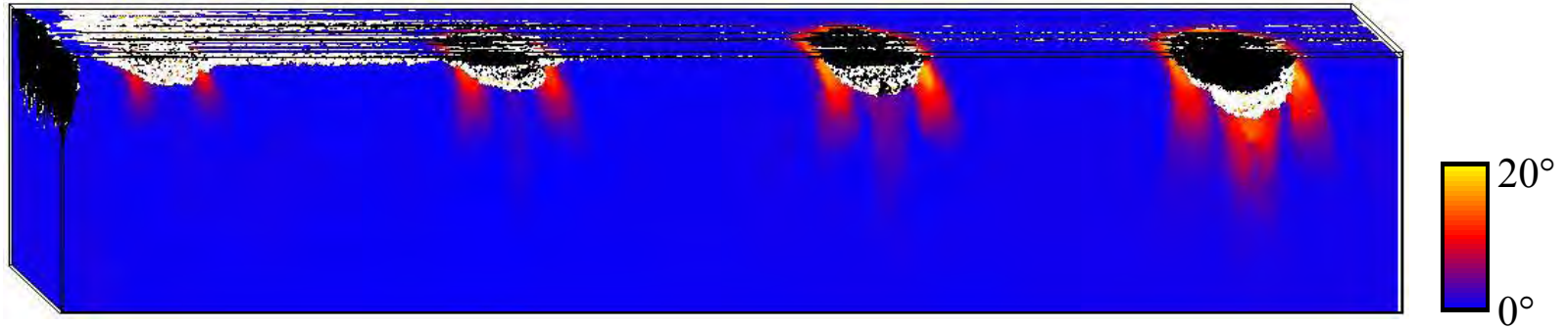
Cu, 60° conical, tip radius 1μm, loading rate 1.82mN/s, loads: 4000μN, 6000μN, 8000μN, 10000μN



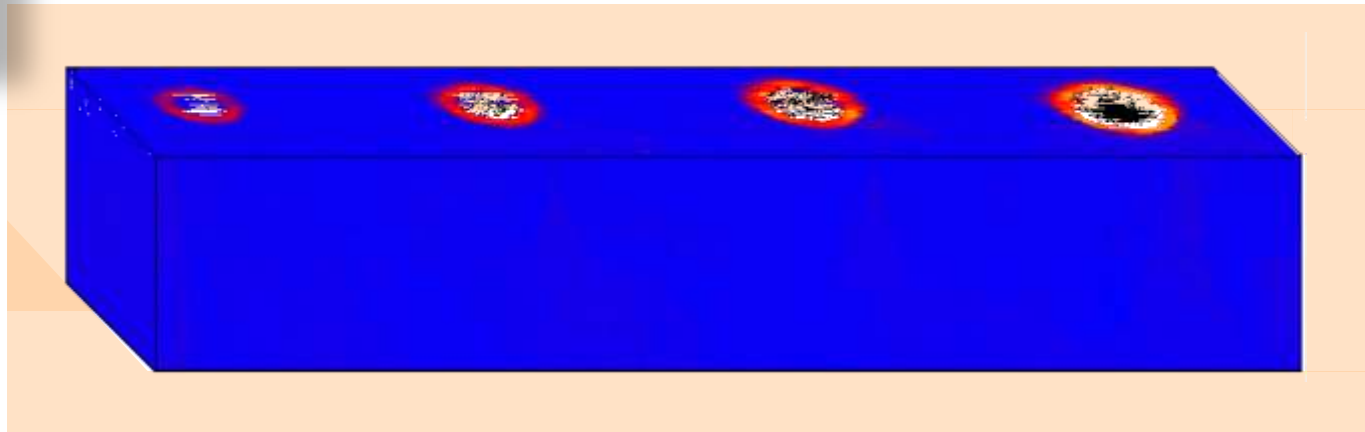
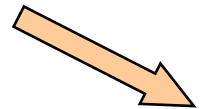
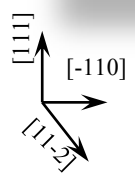
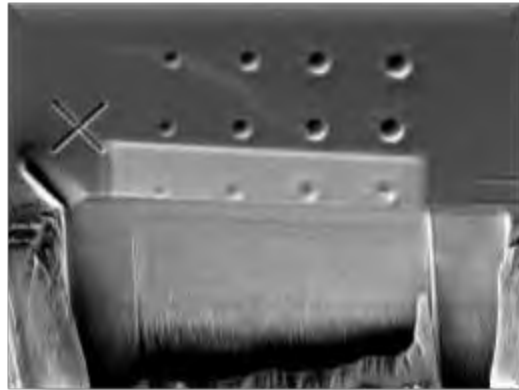
Indentation (smaller is stronger): 3D EBSD and CPFEM



Cu, 60° conical, tip radius 1μm, loading rate 1.82mN/s, loads: 4000μN, 6000μN, 8000μN, 10000μN



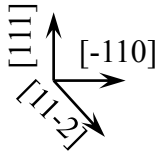
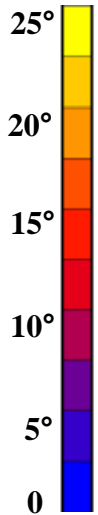
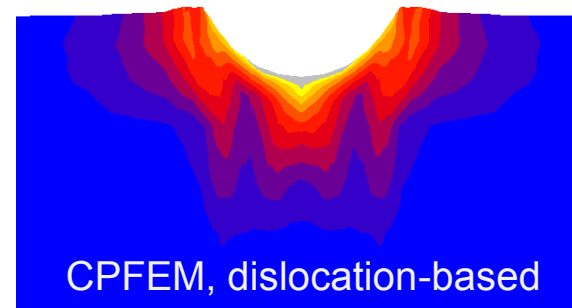
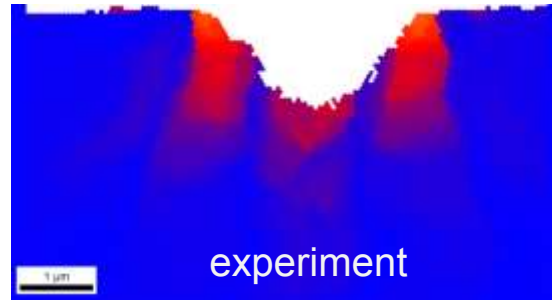
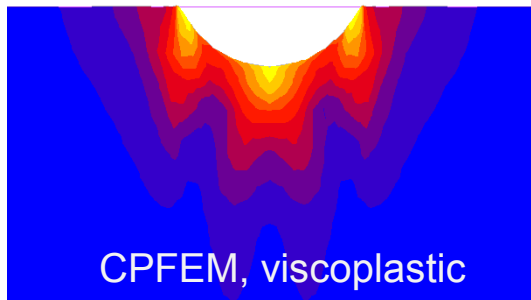
Misorientation angle



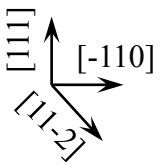
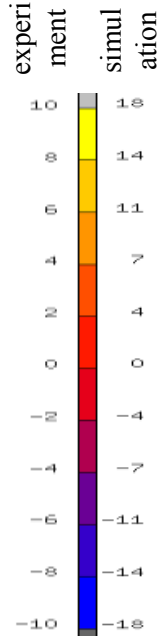
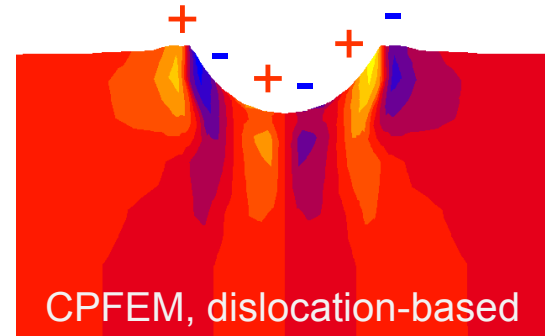
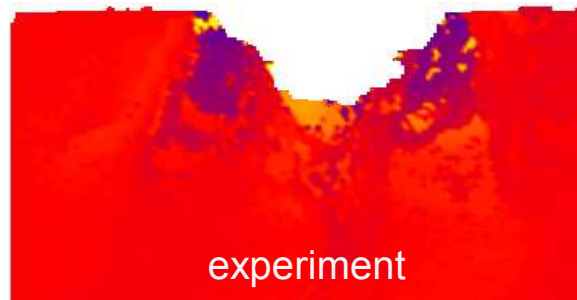
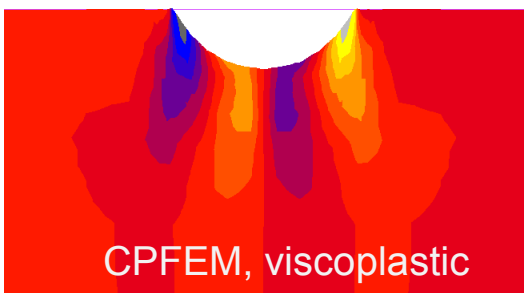
Comparison, crystal rotations (absolute, about [11-2] axis)



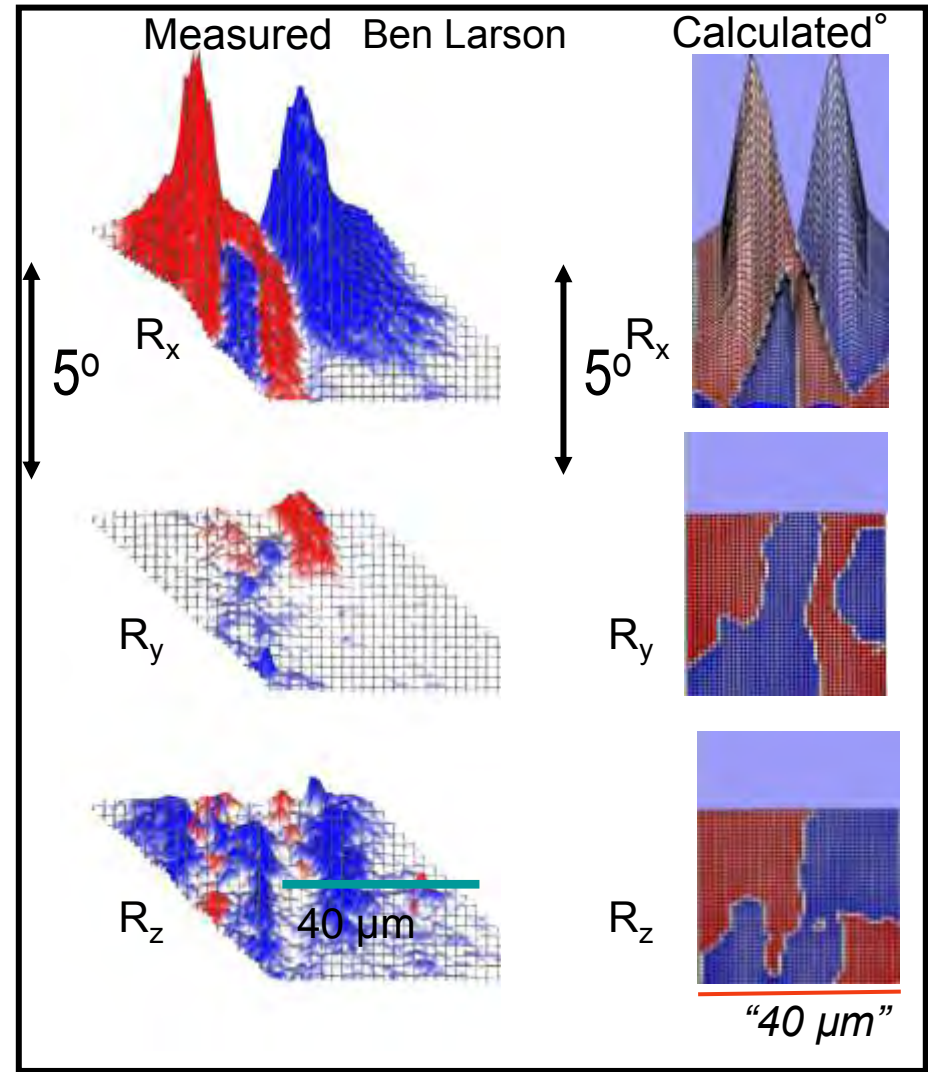
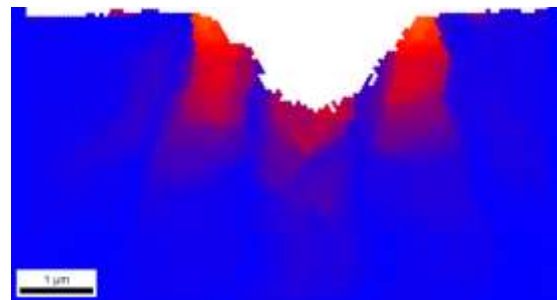
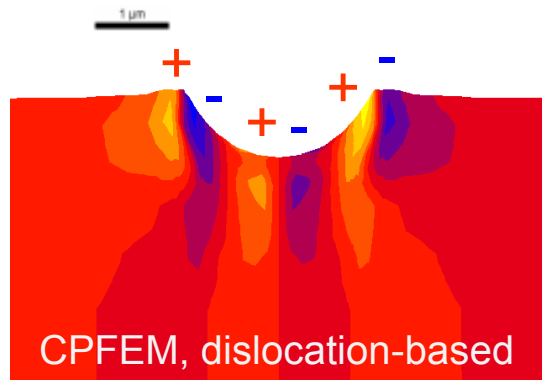
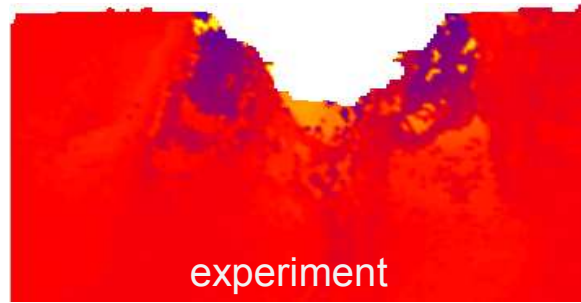
Absolute rotations



<11-2> rotations

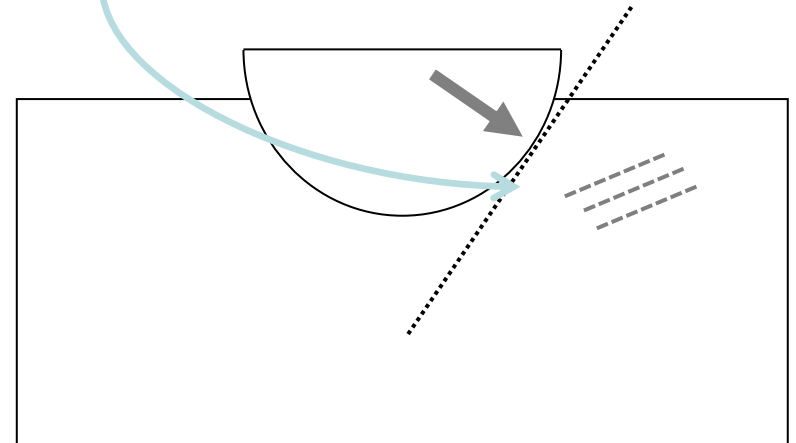
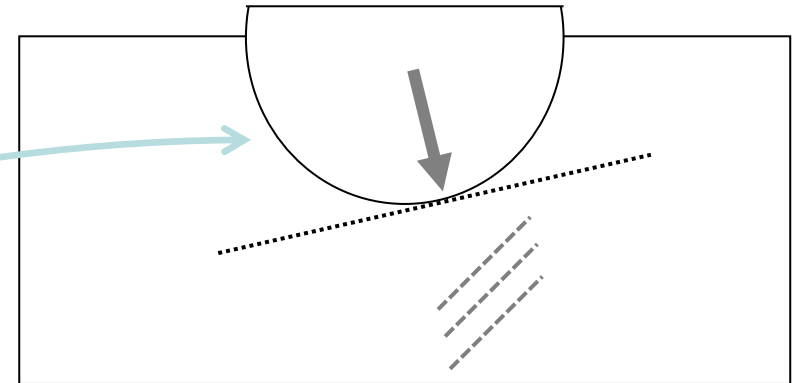
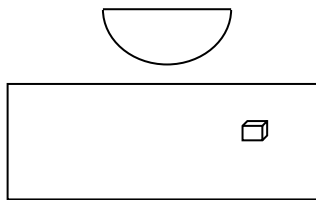
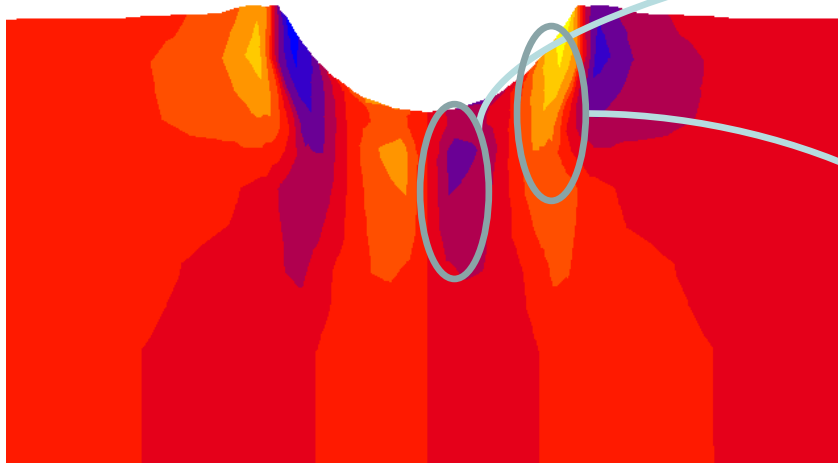
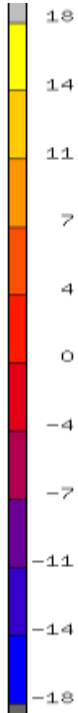
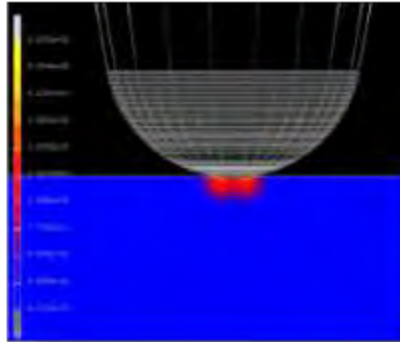


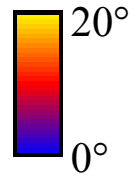
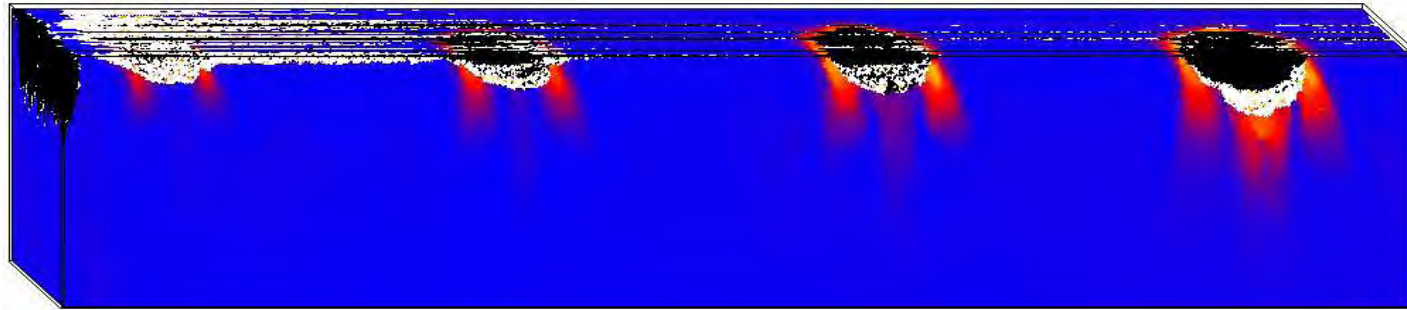
Comparison between crystal rotation about [11-2]



see also: Ben Larson, Bill Clegg, Alan Needleman

Rotations about [11-2] axis, simplify, strain path



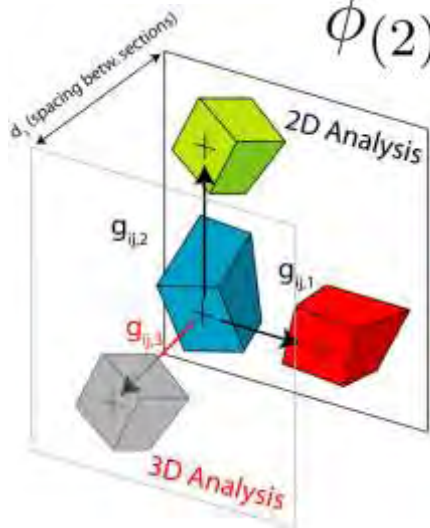


misorientation angle

$$\Delta\phi = \phi_{(2)} \phi_{(1)}^{-1} \quad \text{misorientation}$$

$$|\Delta\phi| = \min\{\cos^{-1}\{tr[(O_i^{cry} \phi_{(1)}) \phi_{(2)}^T O_j^{cry}]\}\} \quad i = 1 \dots 24, j = 1 \dots 24$$

$$\phi_{(2)} - \phi_{(1)} = (\Delta\phi - I)\phi_{(1)} \quad \text{orientation difference}$$



$$g_{ij,k} = \frac{\phi_{(2)ij} - \phi_{(1)ij}}{d_k} \quad \begin{array}{l} \text{orientation gradient} \\ \text{(spacing } d \text{ from EBSD scan)} \end{array}$$



$$\alpha = \nabla \times \beta^{el}$$

$$\alpha_{pi} = e_{pkj} (\epsilon_{ij,k}^{el} + g_{ij,k})$$

$$\alpha_{pi} = e_{pkj} g_{ij,k}$$

dislocation tensor (GND)

J. F. Nye. Some geometrical relations in dislocated crystals. Acta Metall. 1:153, 1953.

E. Kröner. Kontinuumstheorie der Versetzungen und Eigenspannungen (in German). Springer, Berlin, 1958.

E. Kröner. Physics of defects, chapter Continuum theory of defects, p.217. North-Holland Publishing, Amsterdam, Netherlands, 1981.

Slip and line directions of dislocations for GNDs in a FCC crystal

$$\sqrt{2} \hat{\mathbf{b}}: \bar{1}10 \ 10\bar{1} \ 0\bar{1}1 \ \bar{1}\bar{1}0 \ 101 \ 01\bar{1} \ 110 \ \bar{1}01 \ 0\bar{1}\bar{1} \ 1\bar{1}0 \ \bar{1}0\bar{1} \ 011 \ 110 \ 101 \ 011 \ \bar{1}10 \ 10\bar{1} \ 0\bar{1}1$$

$$\sqrt{6} \hat{\mathbf{t}}: \bar{1}\bar{1}2 \ \bar{1}2\bar{1} \ 2\bar{1}\bar{1} \ \bar{1}\bar{1}\bar{2} \ \bar{1}\bar{2}1 \ 211 \ 1\bar{1}\bar{2} \ 121 \ 2\bar{1}\bar{1} \ 112 \ 1\bar{2}\bar{1} \ 2\bar{1}\bar{1} \ 110 \ 101 \ 011 \ \bar{1}10 \ 10\bar{1} \ 0\bar{1}1$$

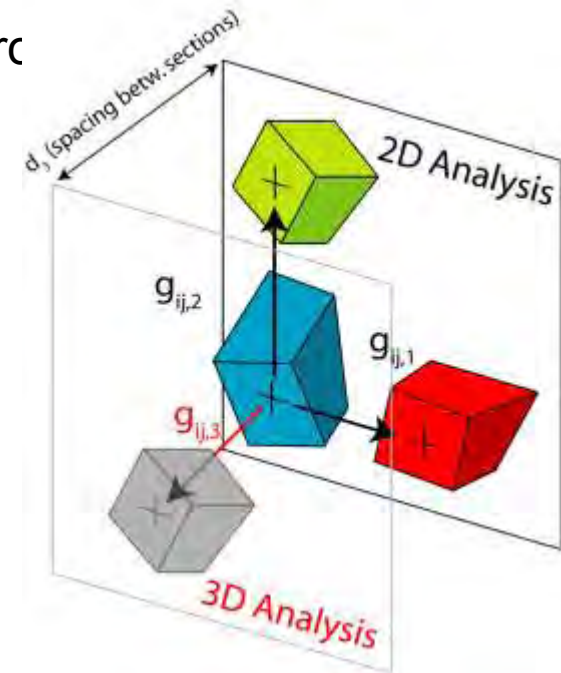
$$\mathbf{B} = \mathbf{b}(\hat{\mathbf{t}} \cdot \mathbf{r}) = (\mathbf{b} \otimes \hat{\mathbf{t}})\mathbf{r} \quad \text{Frank loop thrc}$$

$$\alpha_{ij} = \sum_{a=1}^{18} \rho_{gnd}^a b_i^a t_j^a$$

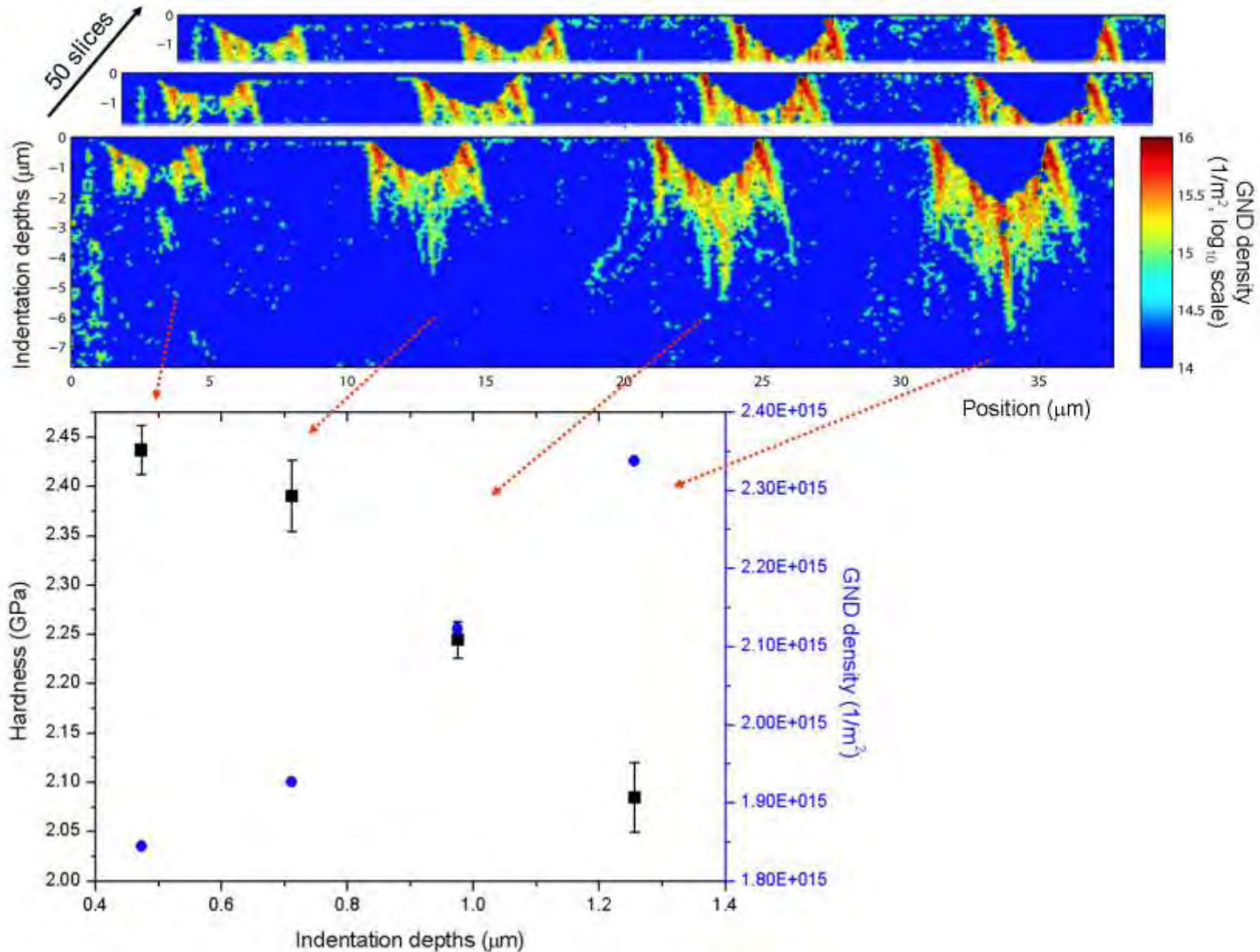
18 b,t combinations

$$\alpha_{ij} = \sum_{a=1}^9 \rho_{gnd}^a b_i^a t_j^a$$

9 b,t combinations



Extract geometrically necessary dislocations

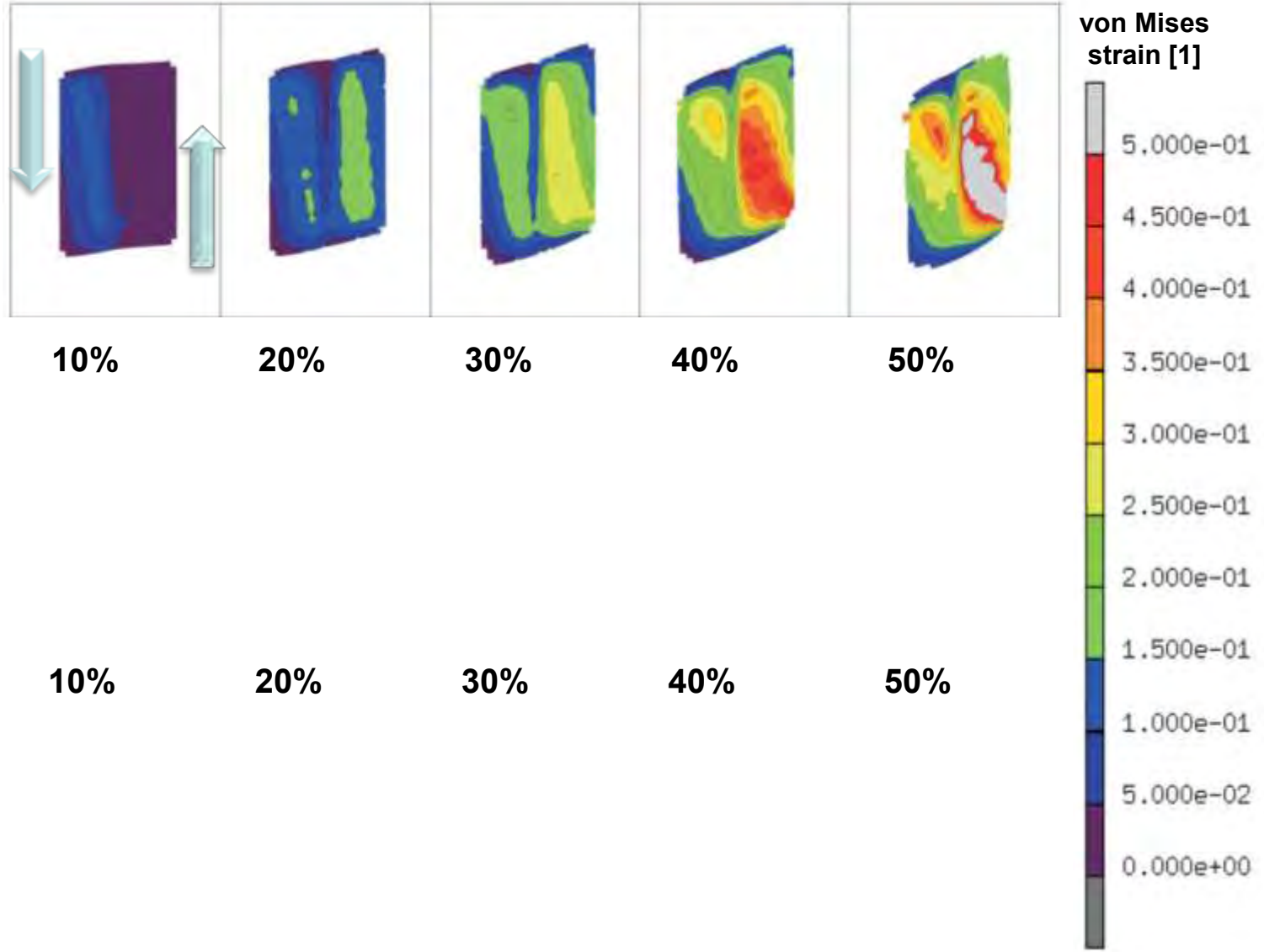




- **Multiscale Crystal Plasticity FEM**
- **Micrometer scale**
 - Indentation
- **Millimeter scale**
 - Grain boundaries
- **Macroscale**
 - Engineering forming simulations
- **Challenges**
 - Bauschinger effects
 - Damage initiation
 - Hybrid simulations
 - FFT solvers
 - Thermomechanical processing
- **Conclusions**



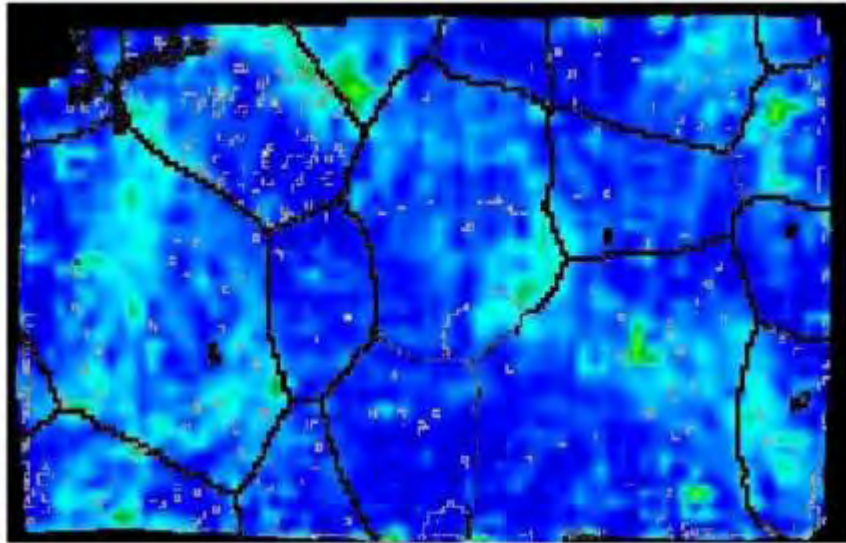
experiment



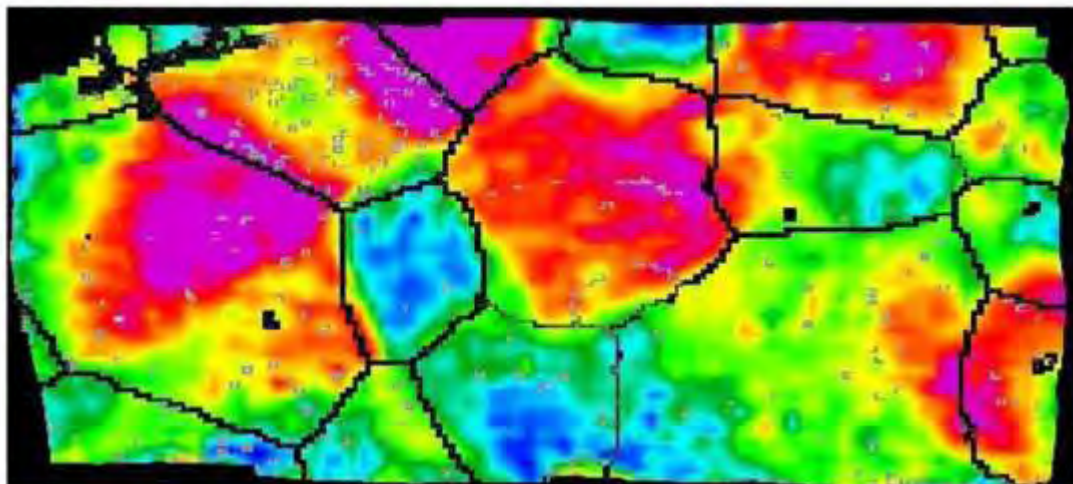
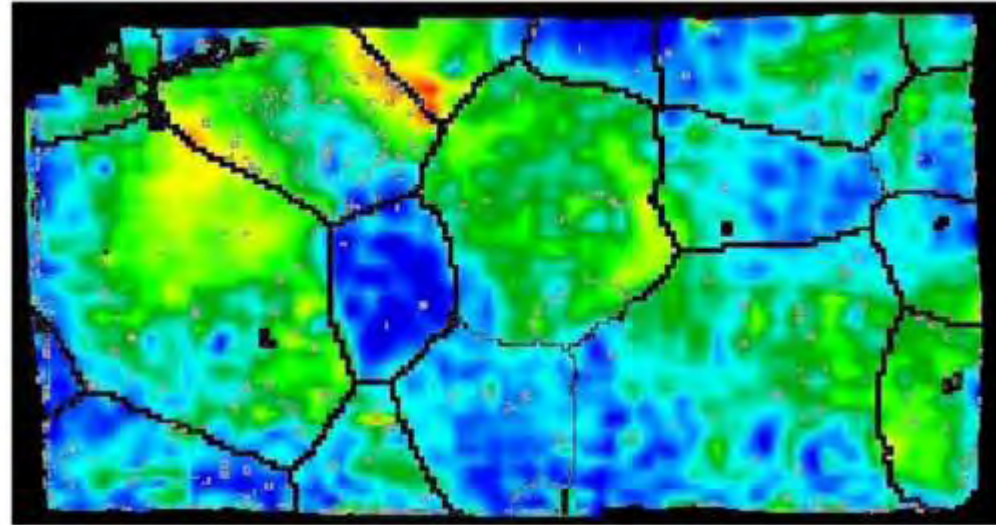
3.1 mm long, 2.0 mm thick and 2.2 mm high, low angle grain boundary (7.4°)



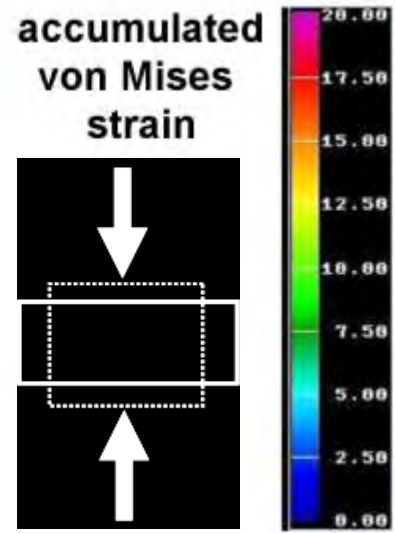
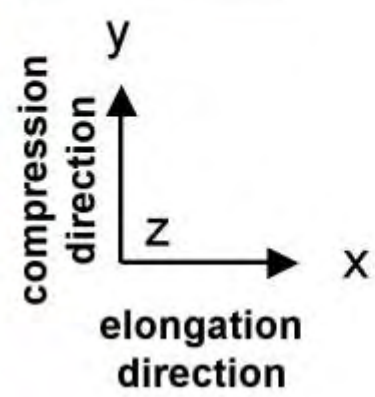
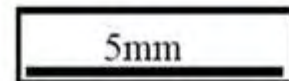
3%



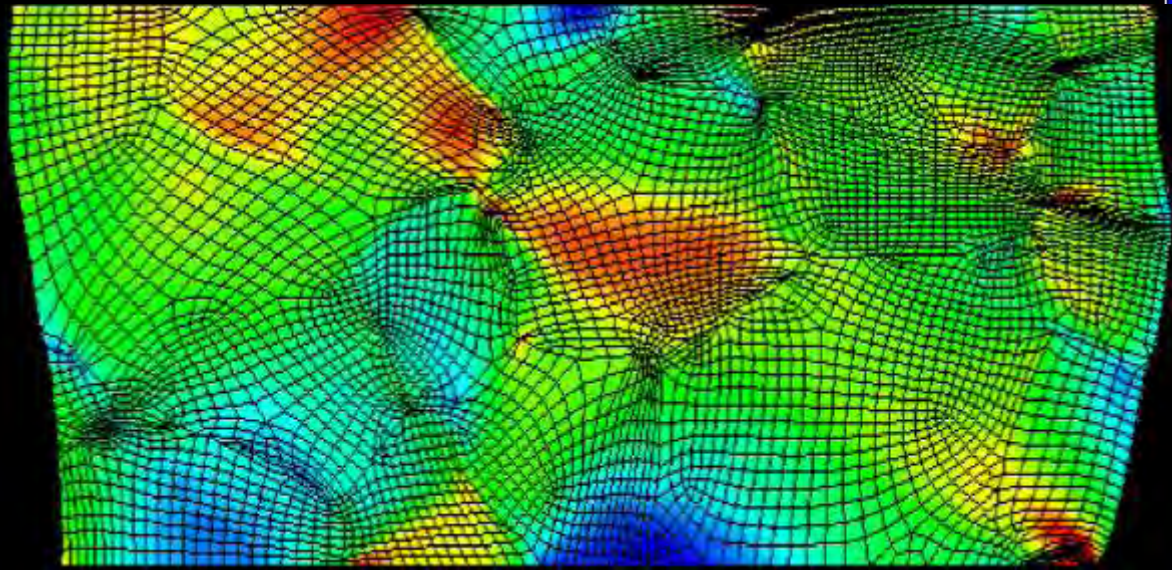
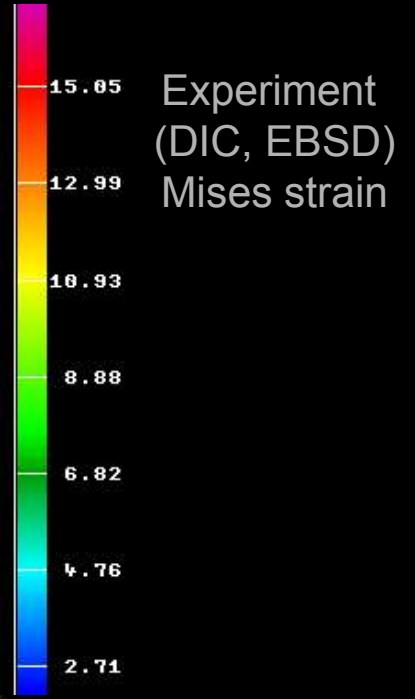
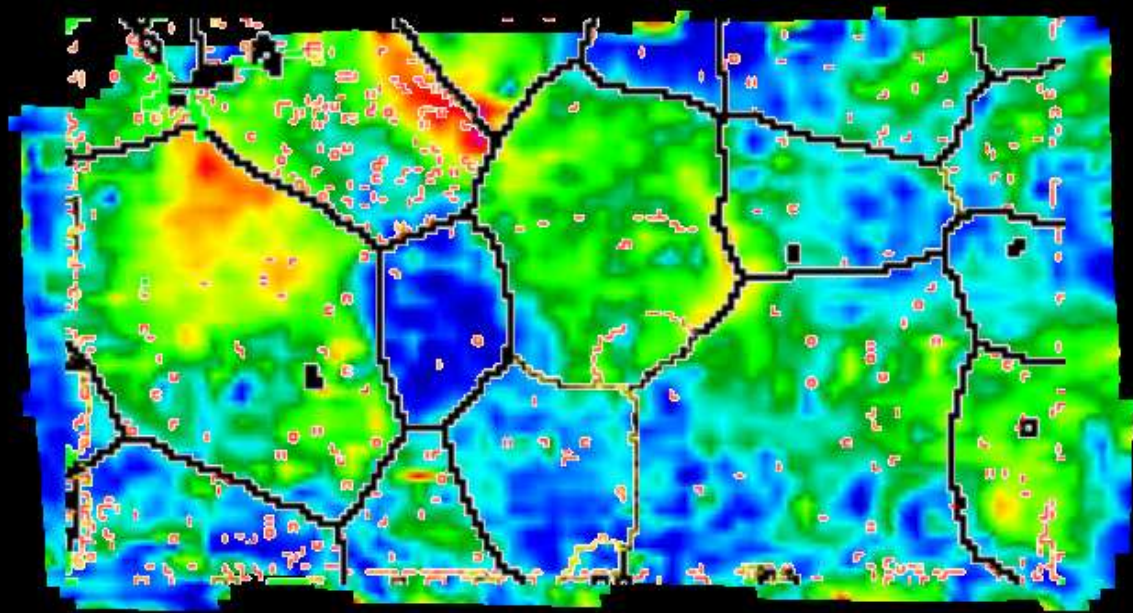
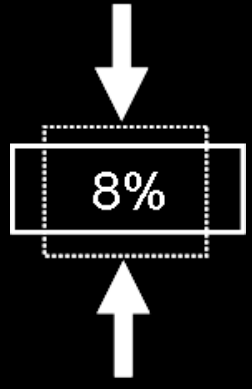
8%



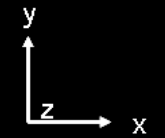
15%



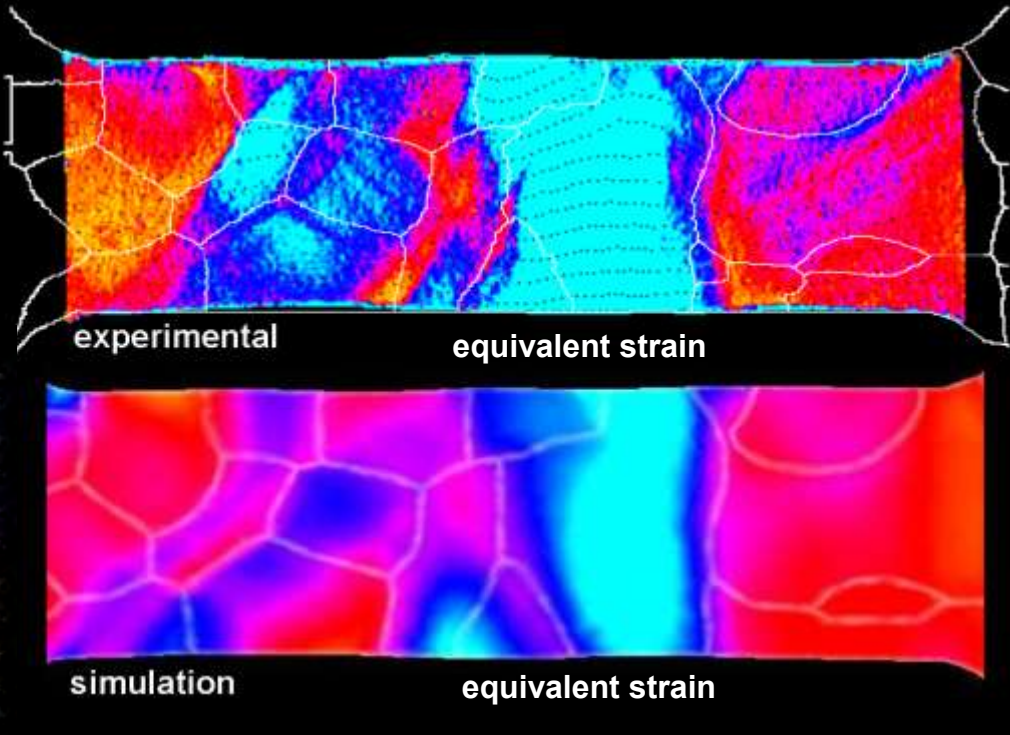
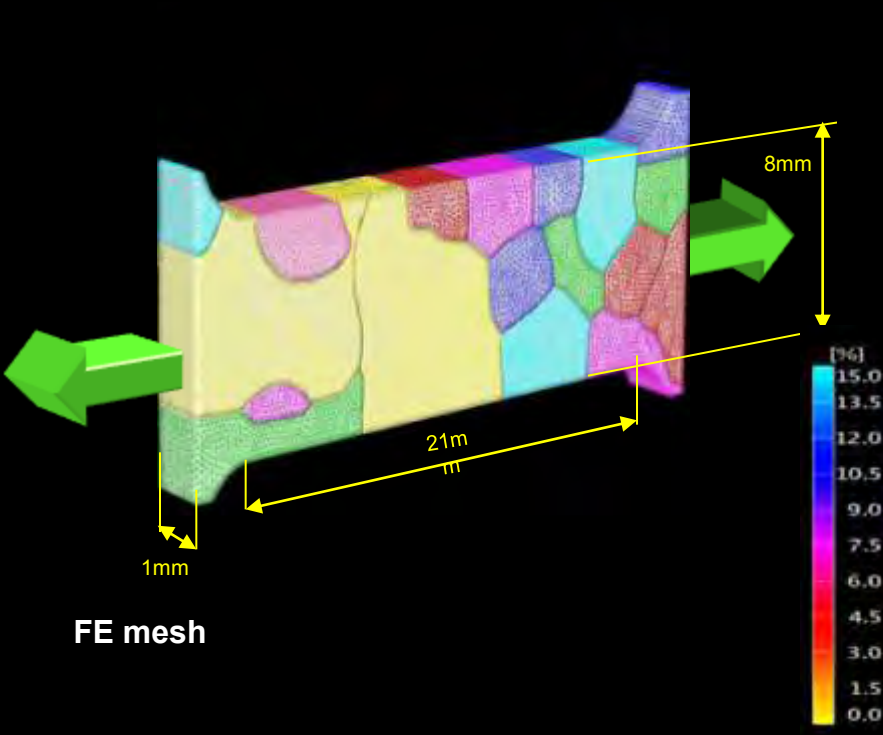
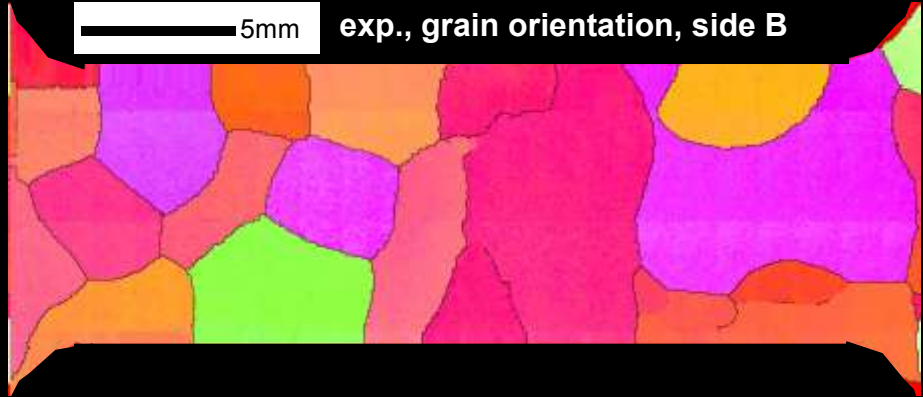
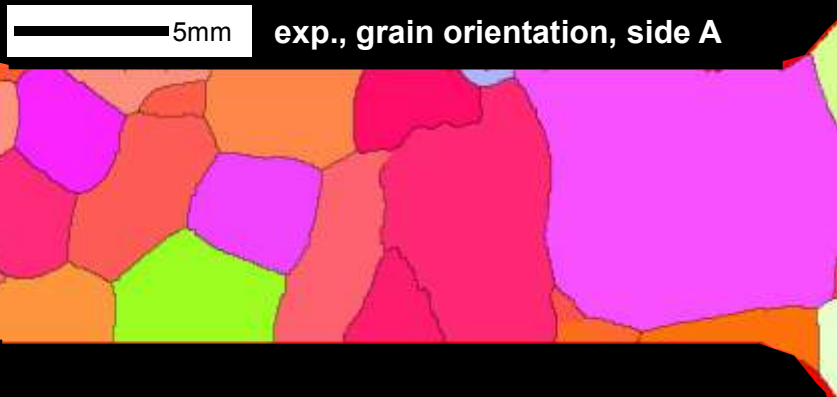
Crystal plasticity FEM, grain scale mechanics (columnar Al, 2D)



Simulation (viscoplastic CP-FEM) Mises strain

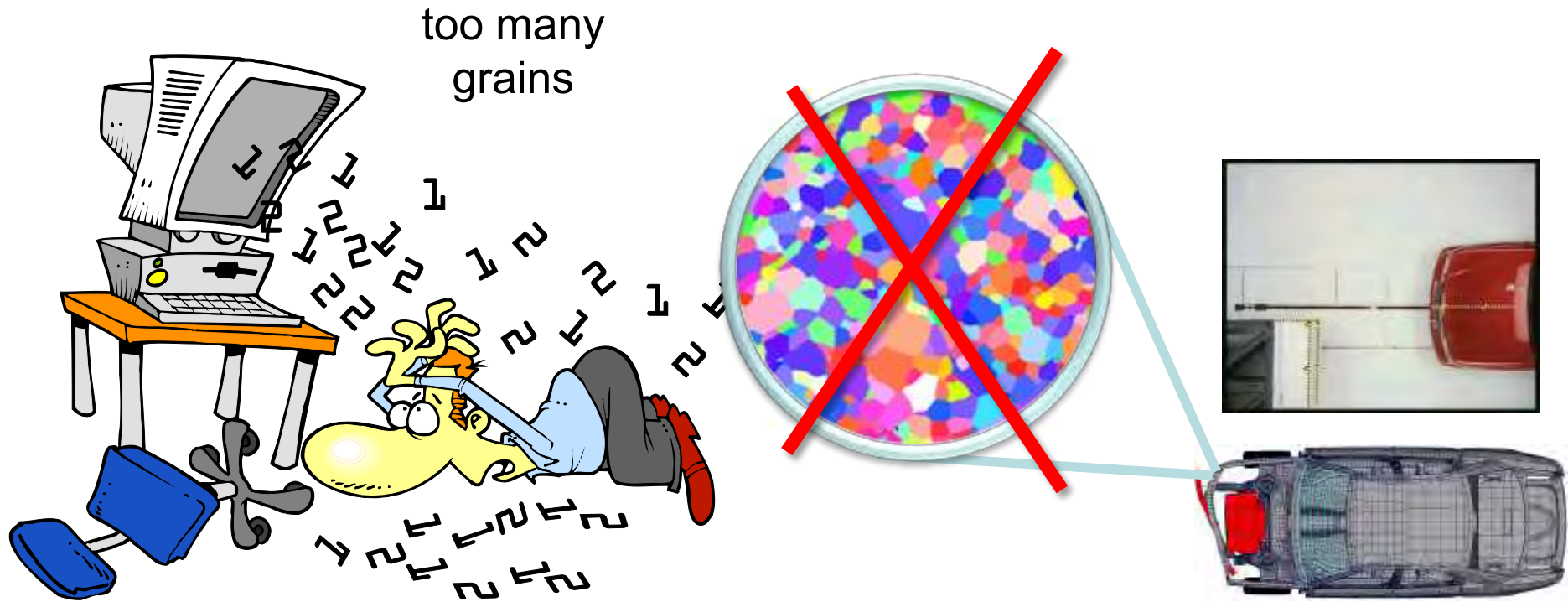


Crystal plasticity FEM, grain scale mechanics (3D grains, Al)

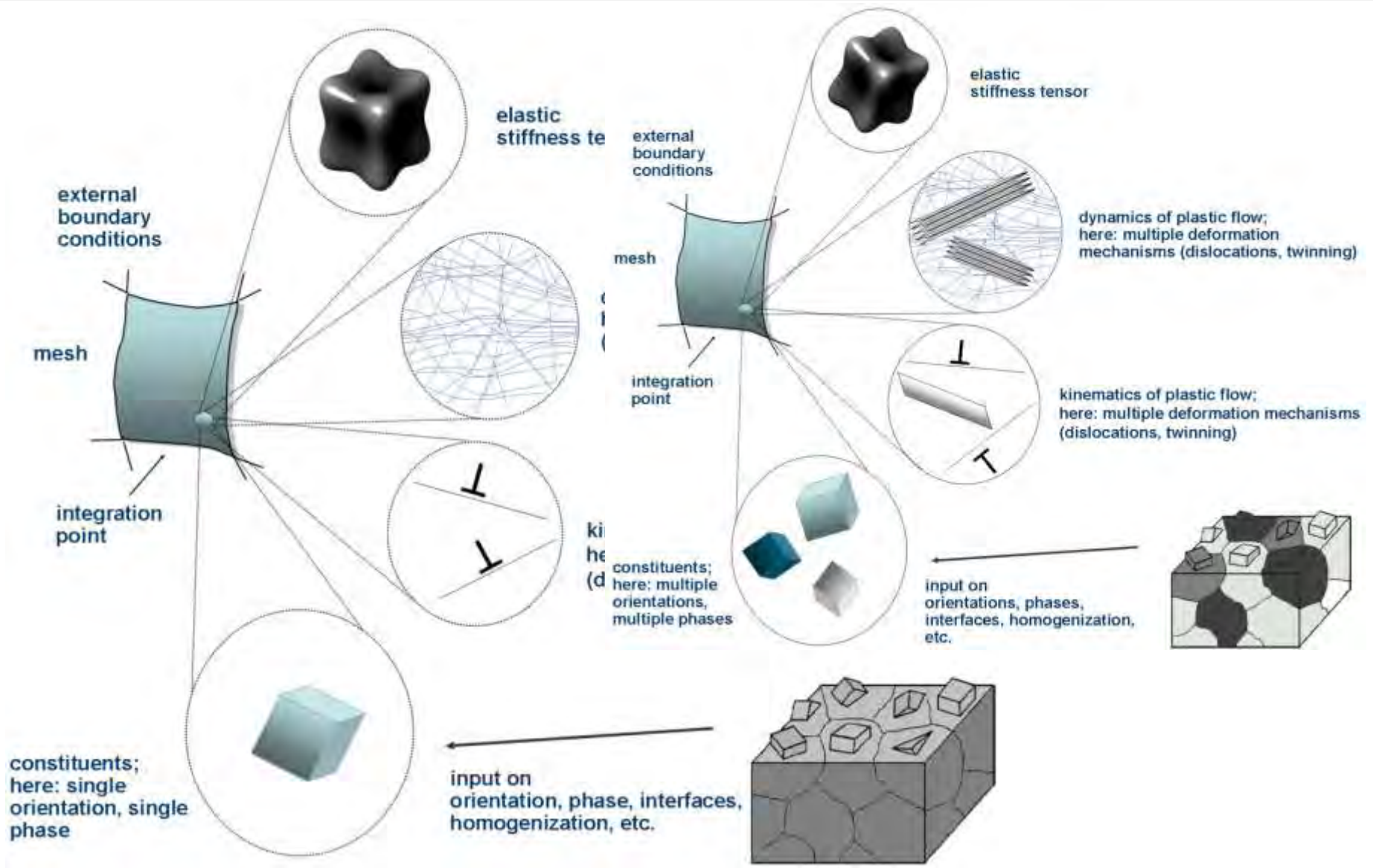


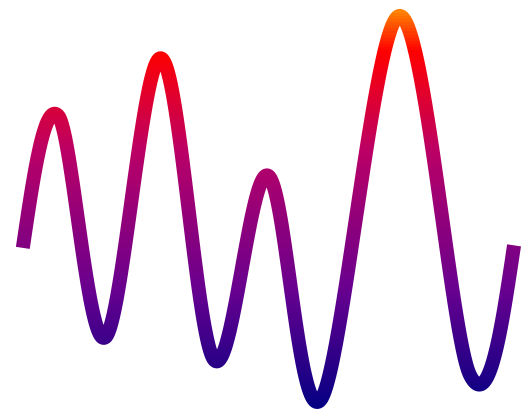


- **Multiscale Crystal Plasticity FEM**
- **Micrometer scale**
 - Indentation
- **Millimeter scale**
 - Grain boundaries
- **Macroscale**
 - Engineering forming simulations
- **Challenges**
 - Bauschinger effects
 - Damage initiation
 - Hybrid simulations
 - FFT solvers
 - Thermomechanical processing
- **Conclusions**



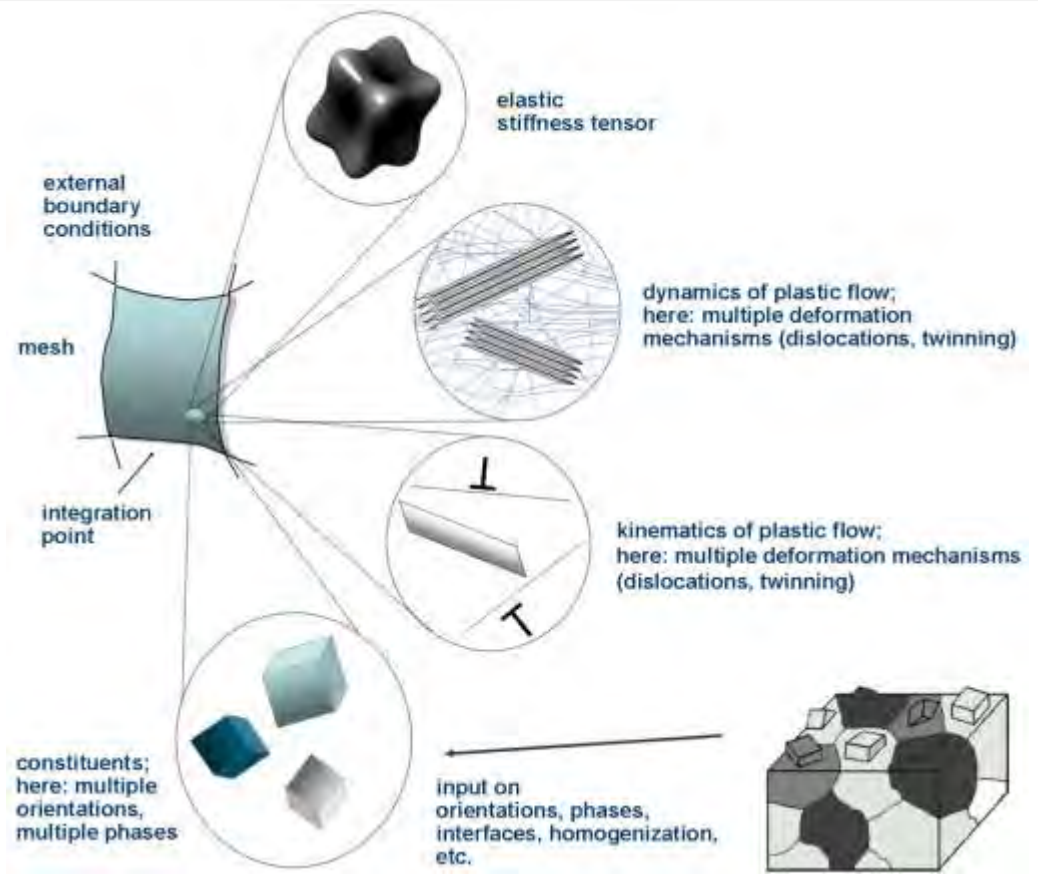
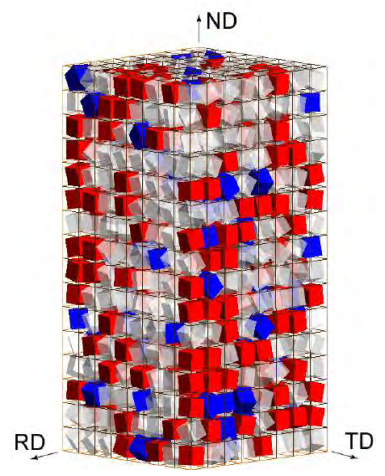
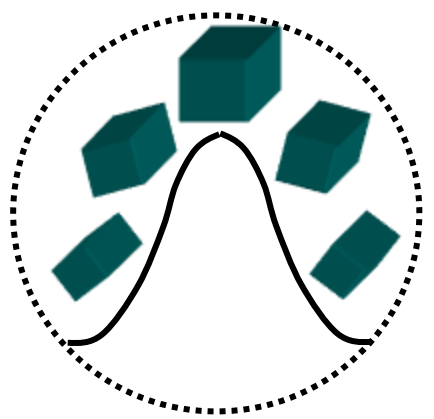
Multiscale crystal plasticity FEM for large scale forming



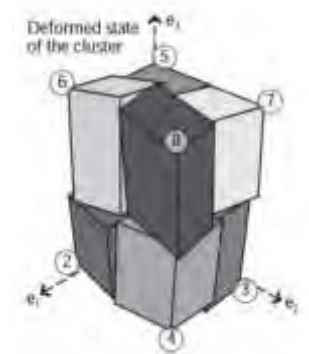
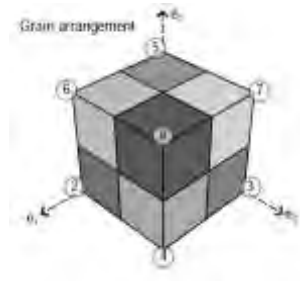


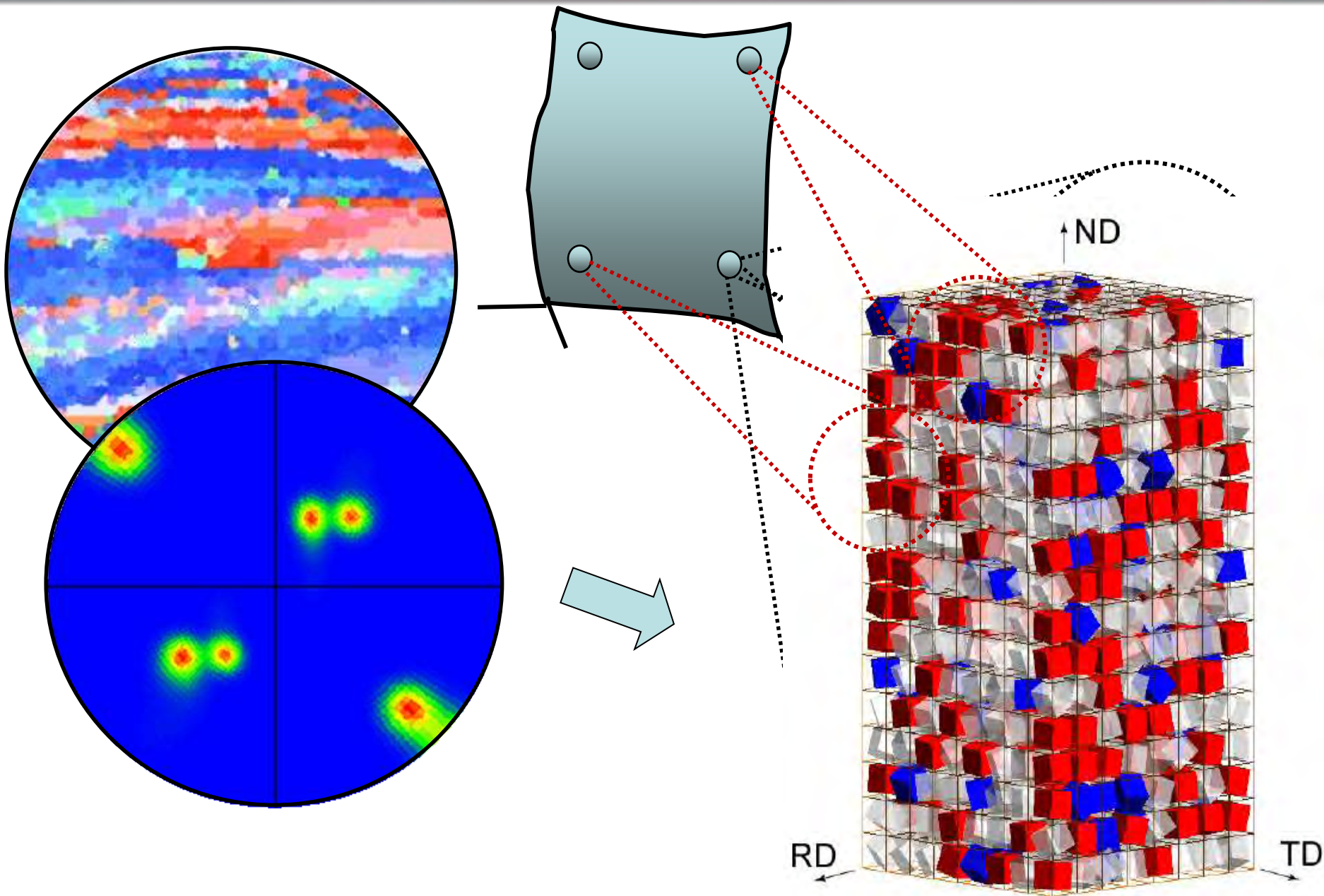
FFT

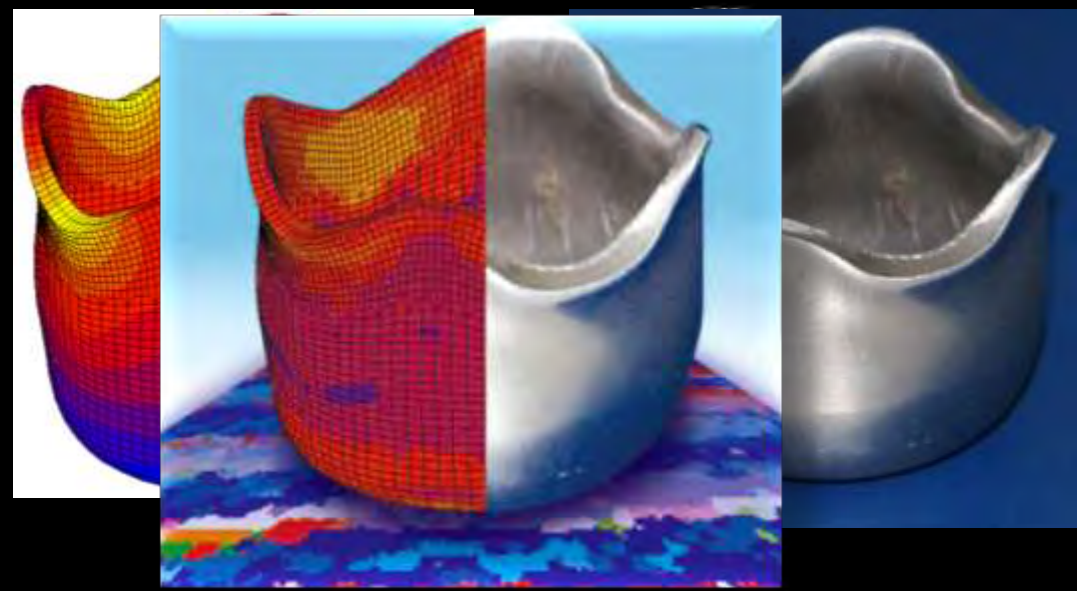
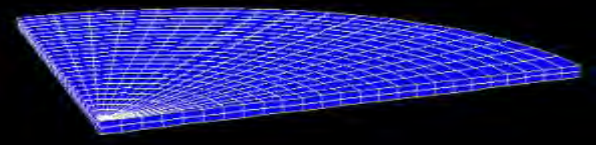
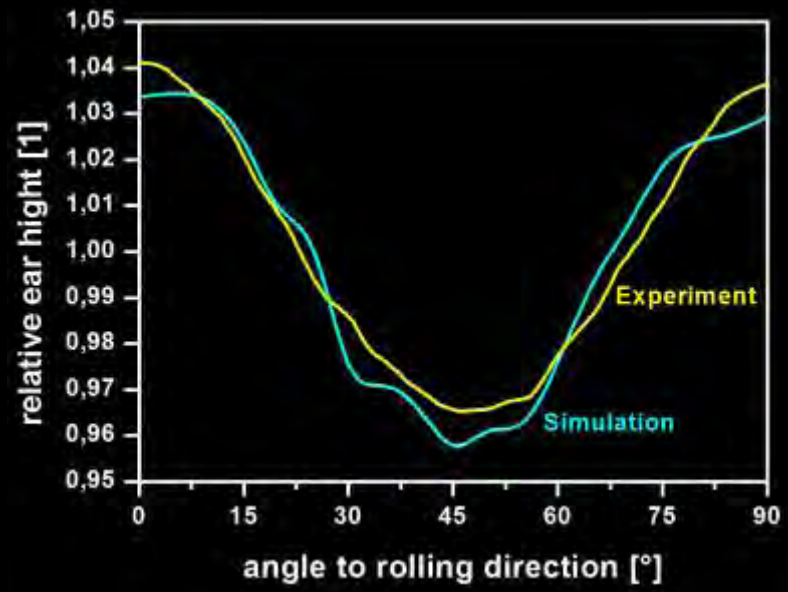
TC-CPFEM



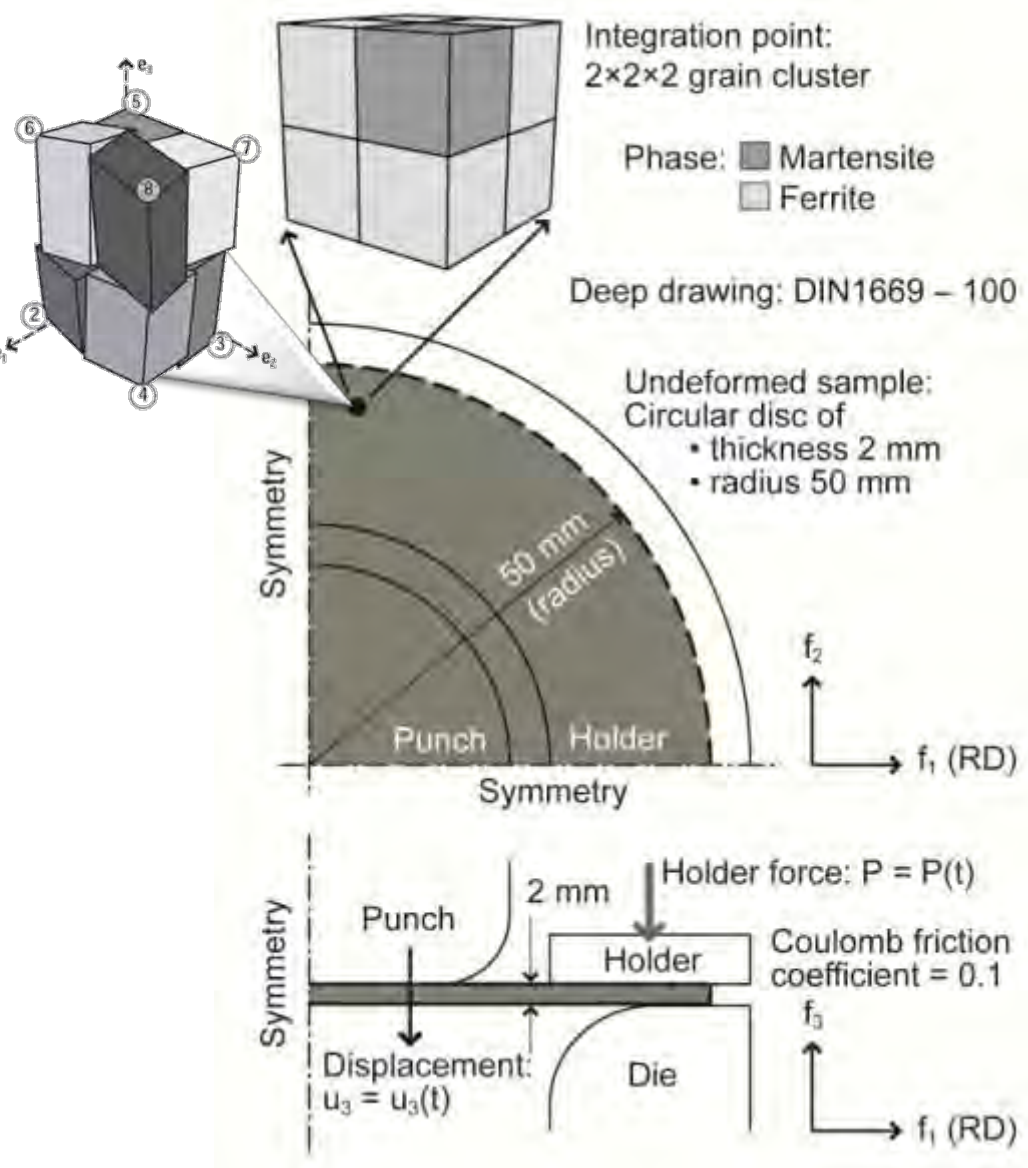
Clustermodels



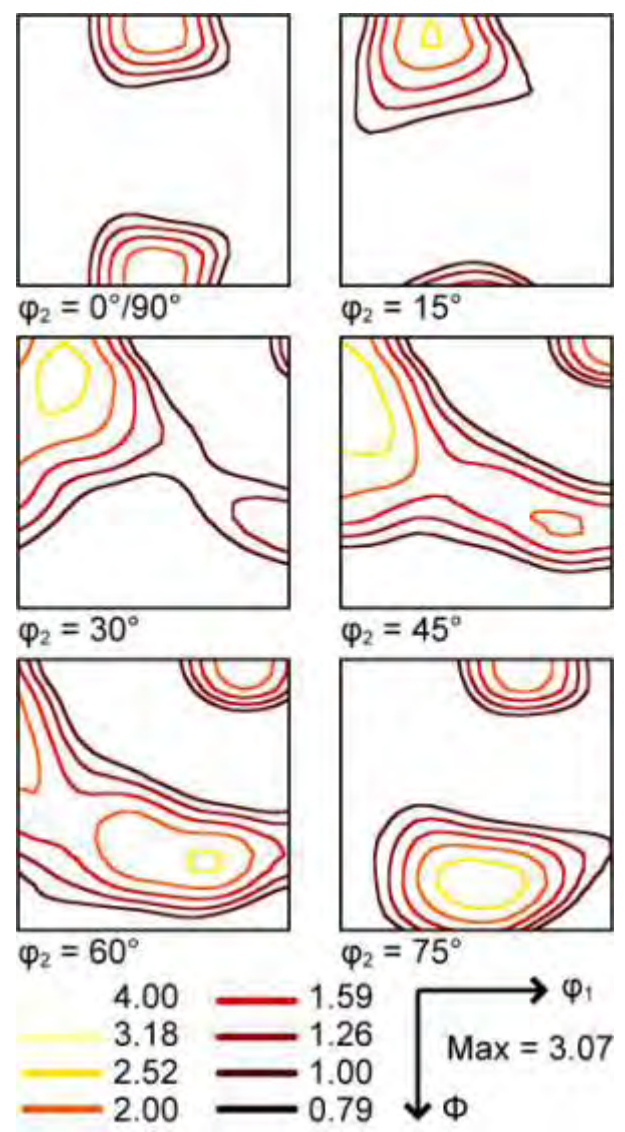


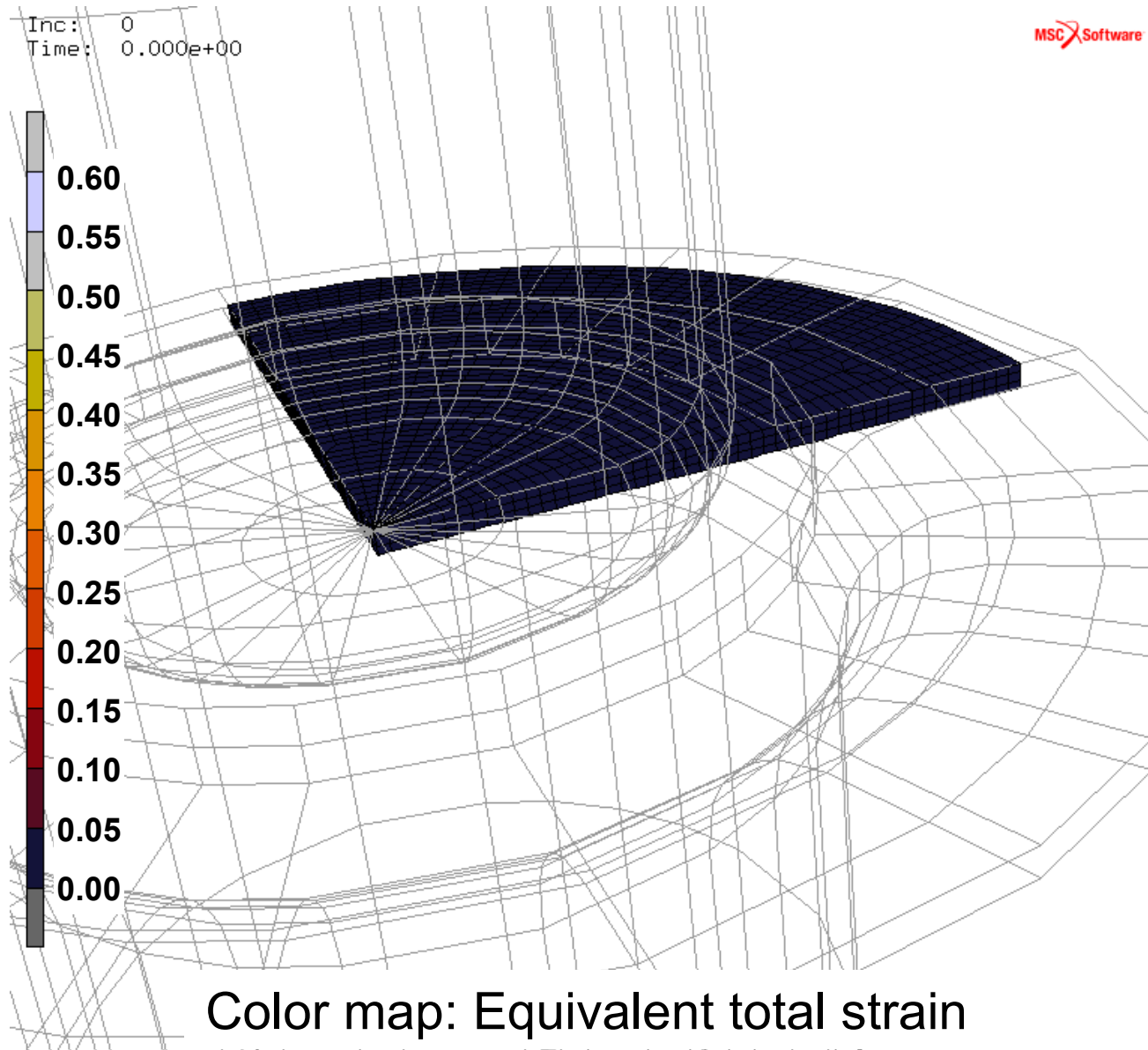


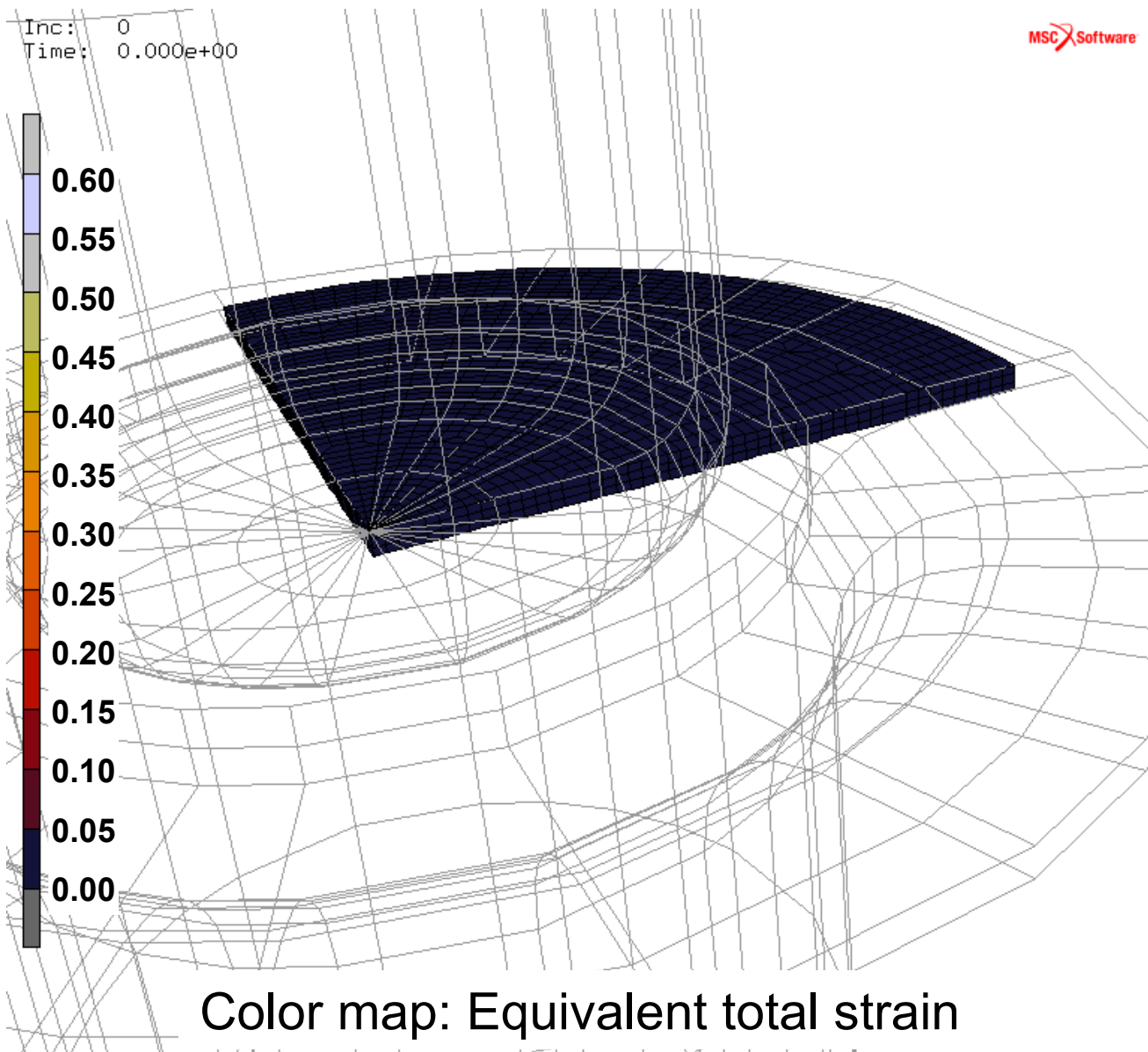
Simulation setup: grain cluster homogenization



Initial texture of bcc ferrite:

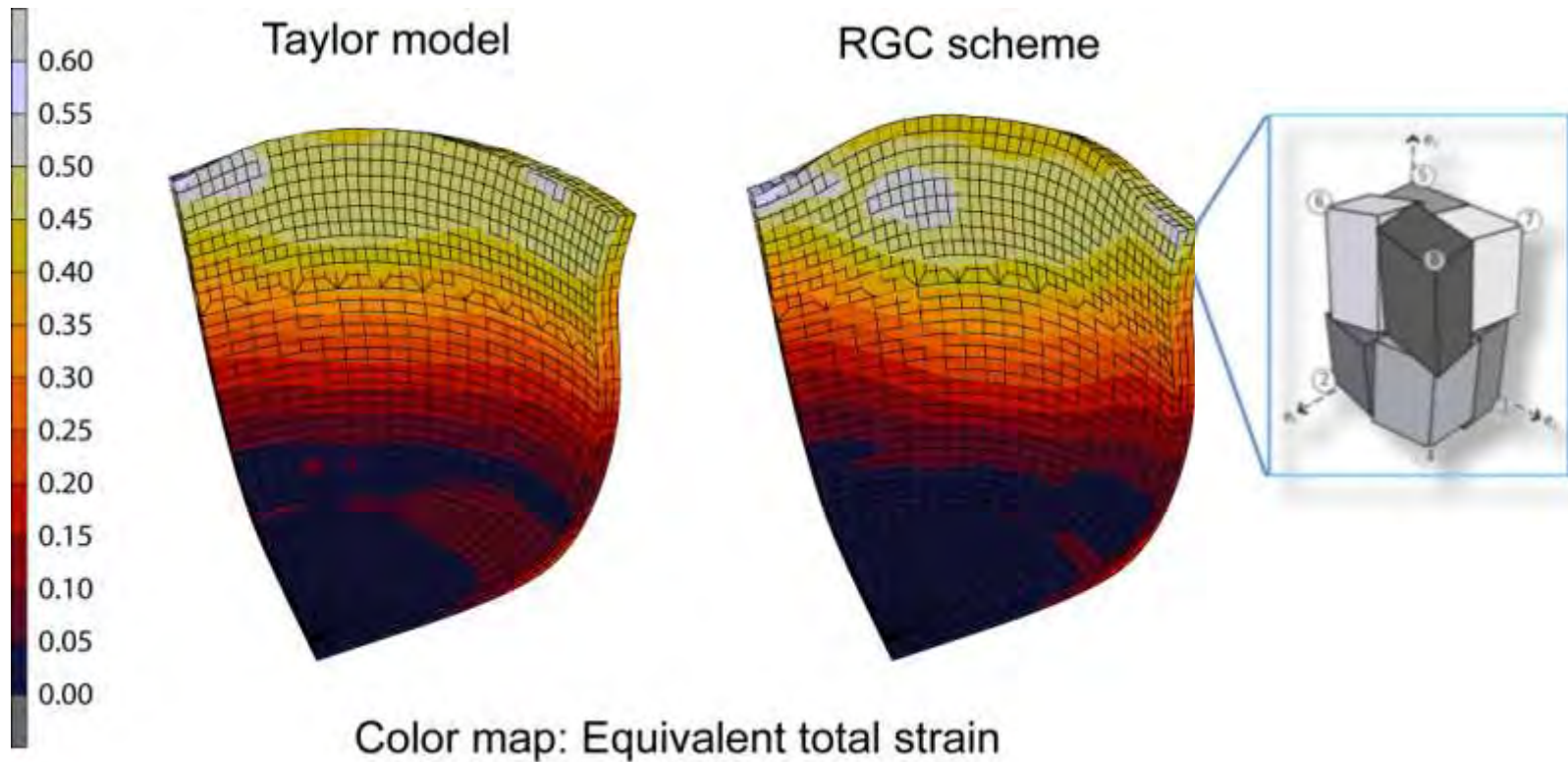






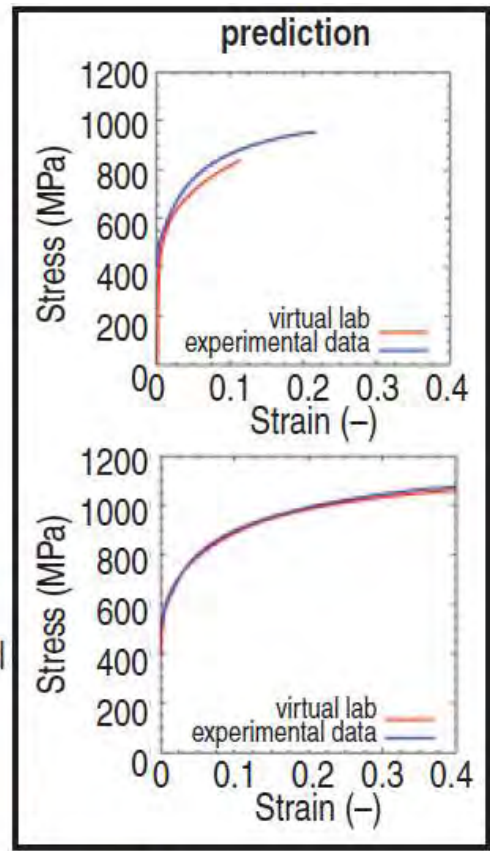
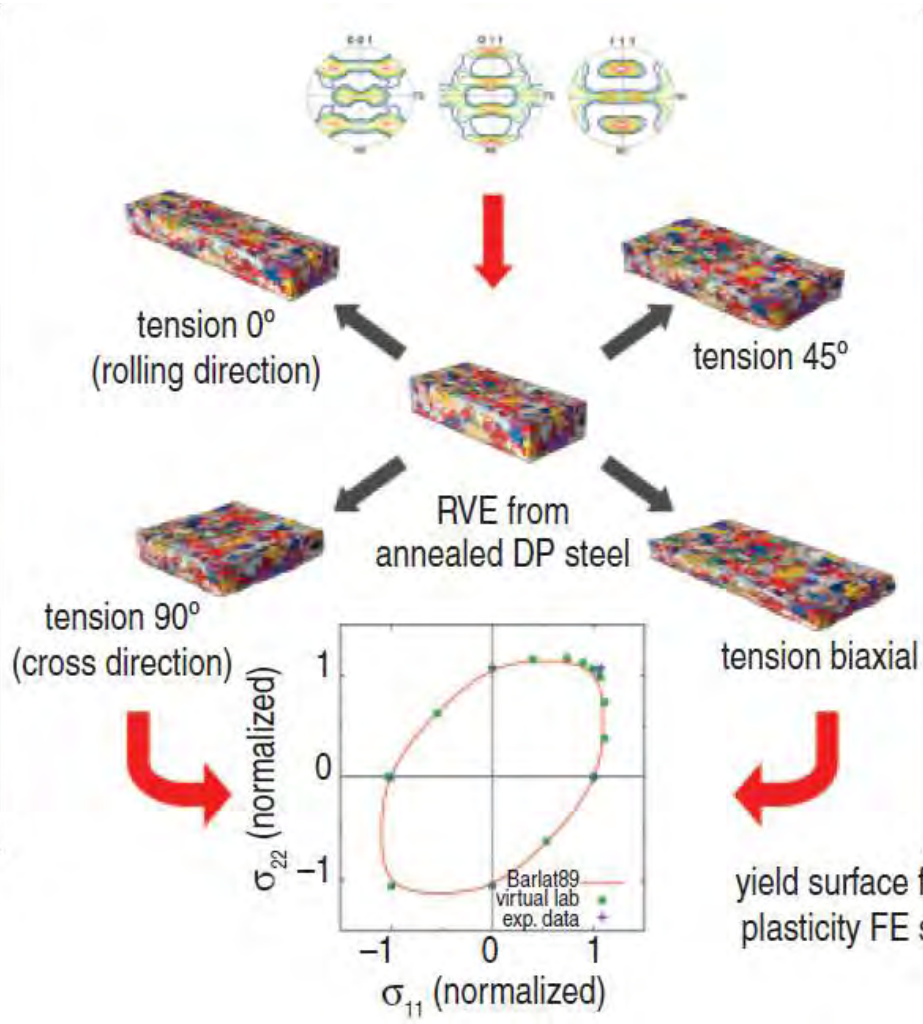
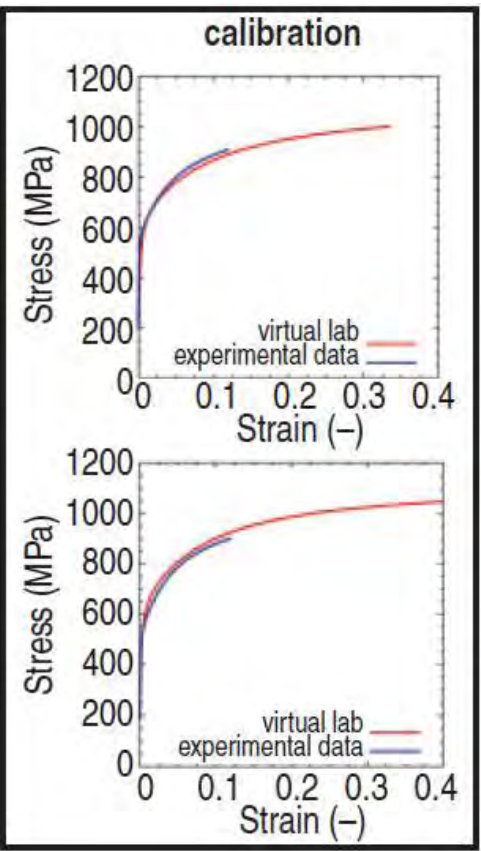


- RGC scheme predicts different ear-profile than Taylor
- RGC computation time ~ 5 times Taylor model



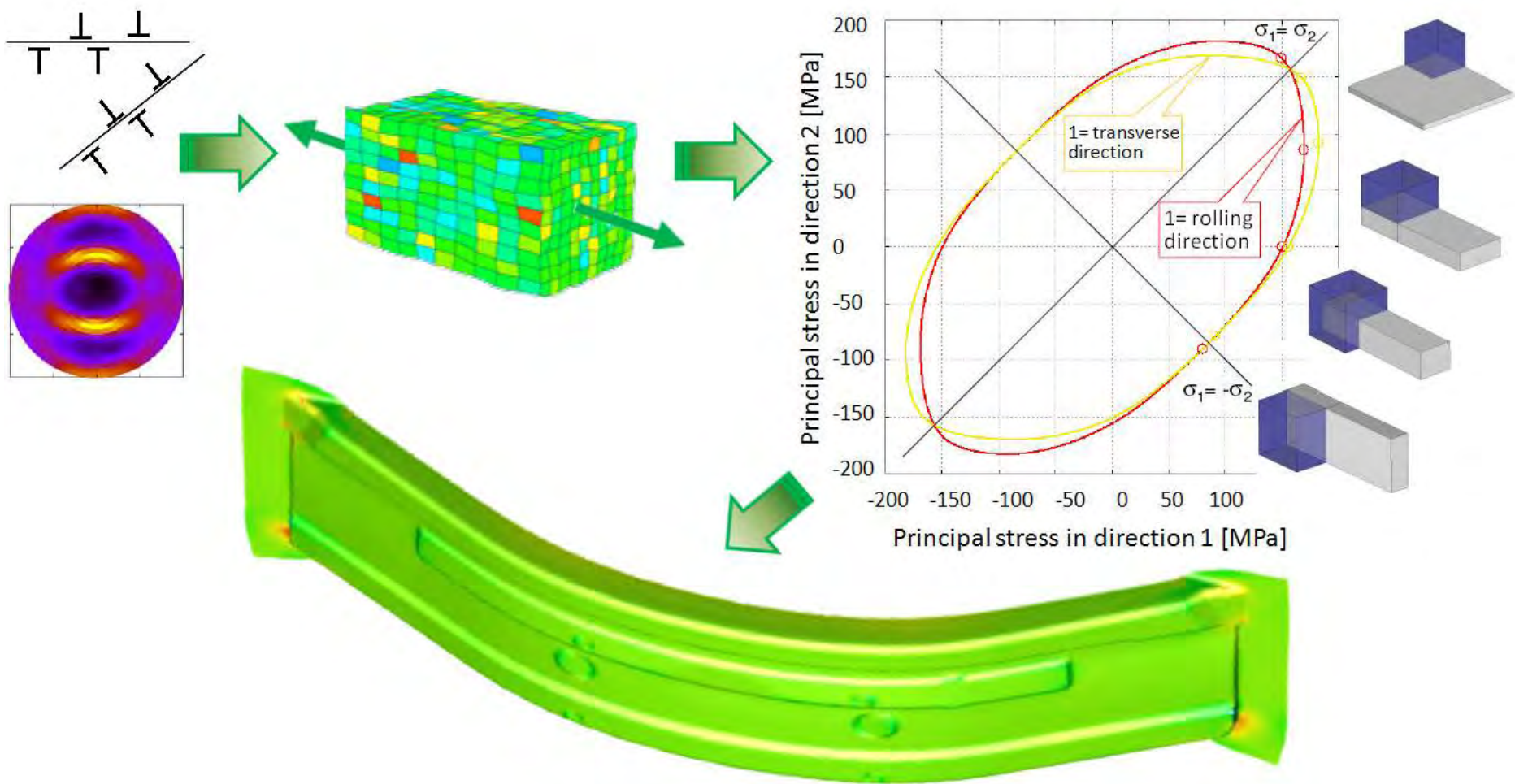


Numerical Laboratory: From CPFEM to yield surface (engineering)





Numerical Laboratory: From CPFEM to yield surface (engineering)



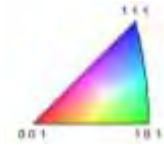
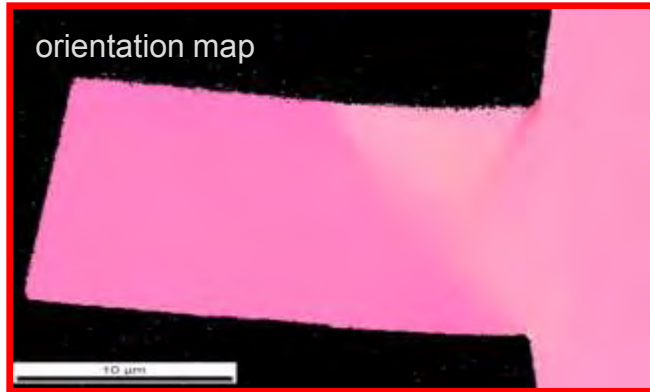
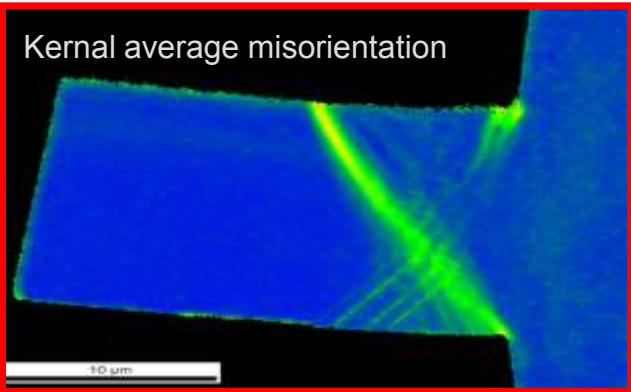
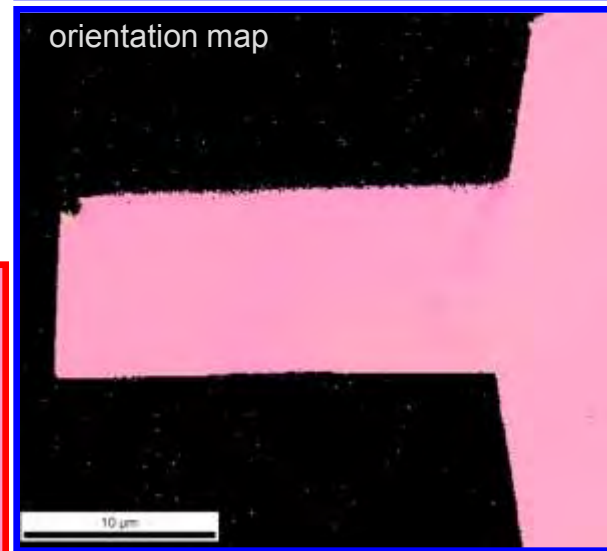
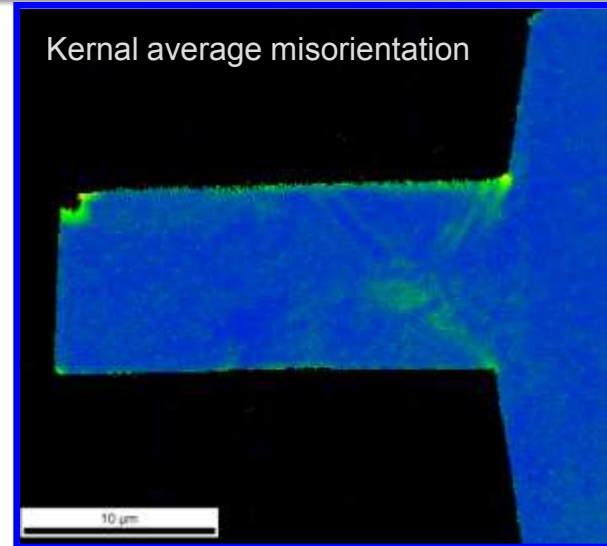
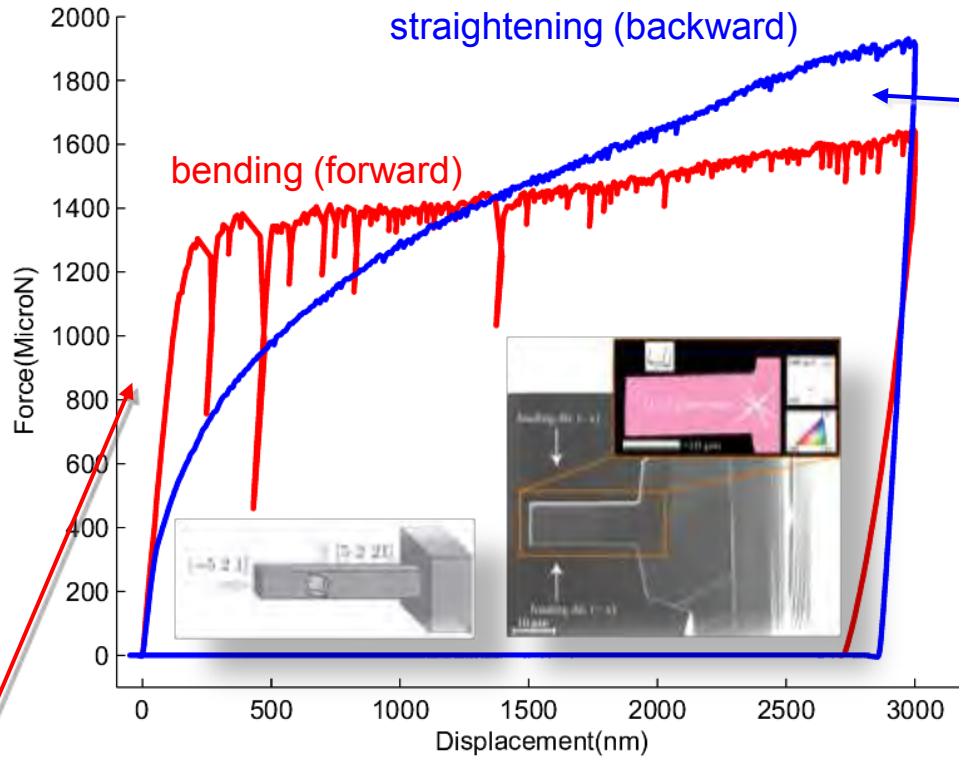
DC04 study with Mercedes, Volkswagen, Audi, Inpro



- **Multiscale Crystal Plasticity FEM**
- **Micrometer scale**
 - Indentation
- **Millimeter scale**
 - Grain boundaries
- **Macroscale**
 - Engineering forming simulations
- **Challenges**
 - Bauschinger effects
 - Damage initiation
 - Hybrid simulations
 - FFT solvers
 - Thermomechanical processing
- **Conclusions**

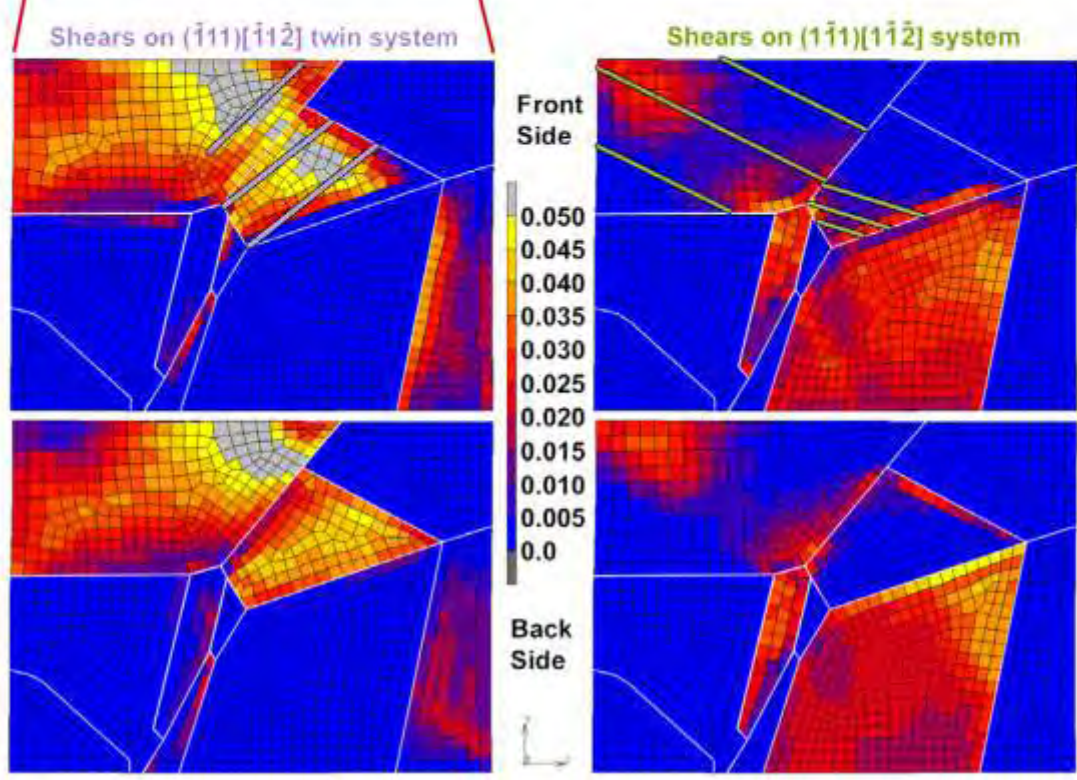
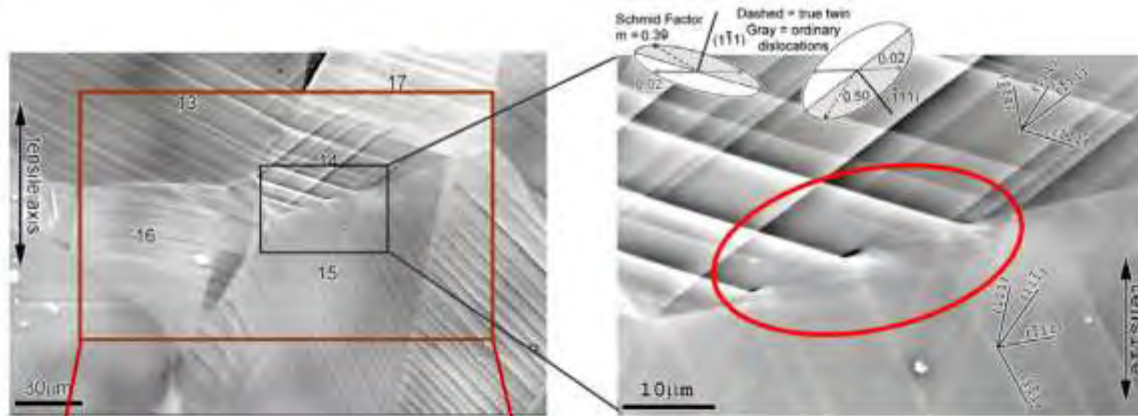


Microscale Bauschinger* effect in beam bending



* Bauschinger effect: flow stress asymmetry upon load path change

Crystal plasticity FEM and damage initiation

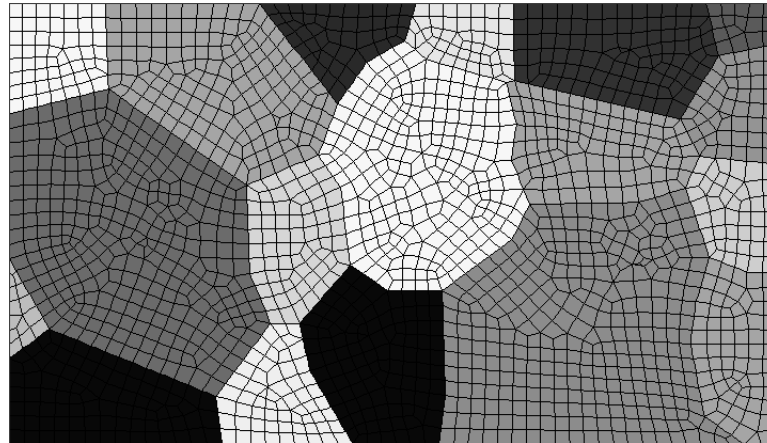


T.R. Bieler, P. Eisenlohr, F. Roters, D. Kumar, D.E. Mason, M.A. Crimp, D. Raabe: Intern. J. Plast. 25 (2009) 1655



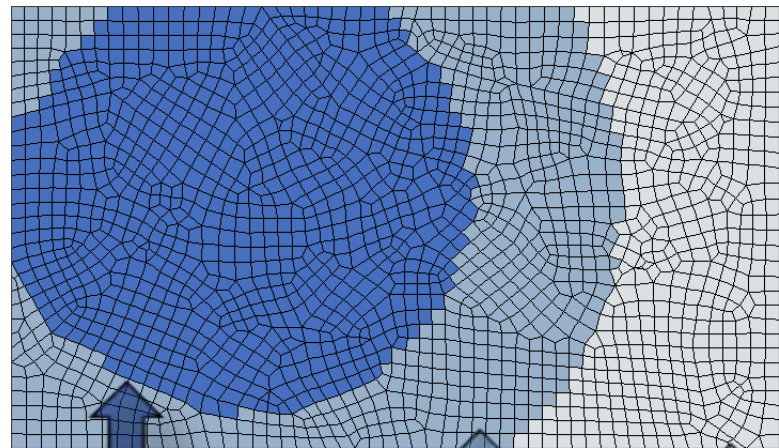
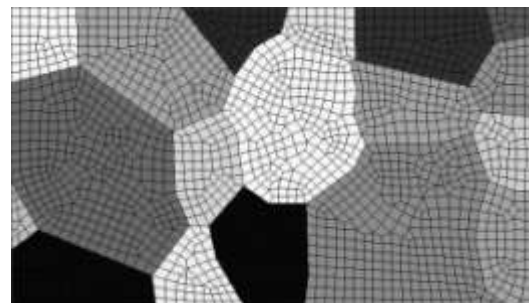
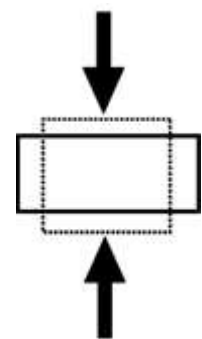
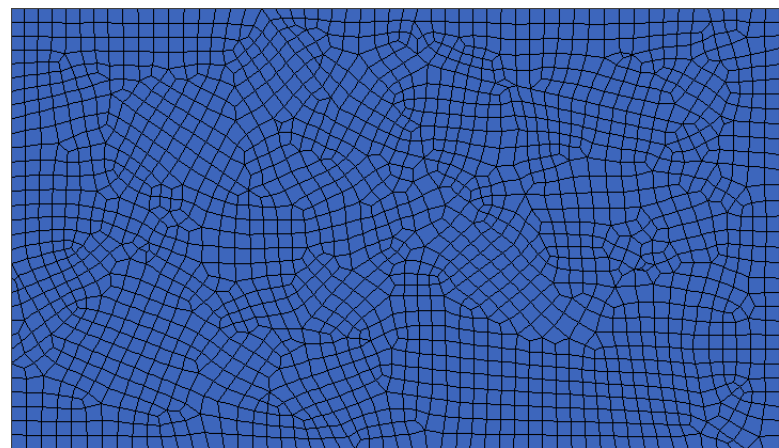
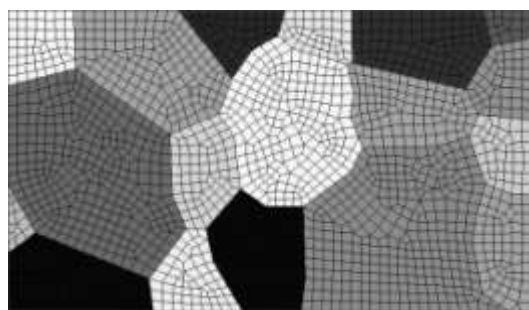
- plane strain compression of oligo-crystal (18 grains)
- 1876 quadratic hexahedral elements (1 layer)
- 13530 nodes

- Reference to DIC experiment
- Interest focused on corner of hard central grain





full-field dislocation density-based CPFEM



modular

dislocation density-based

phenomenological CP

J2 isotropic

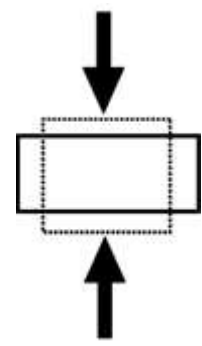
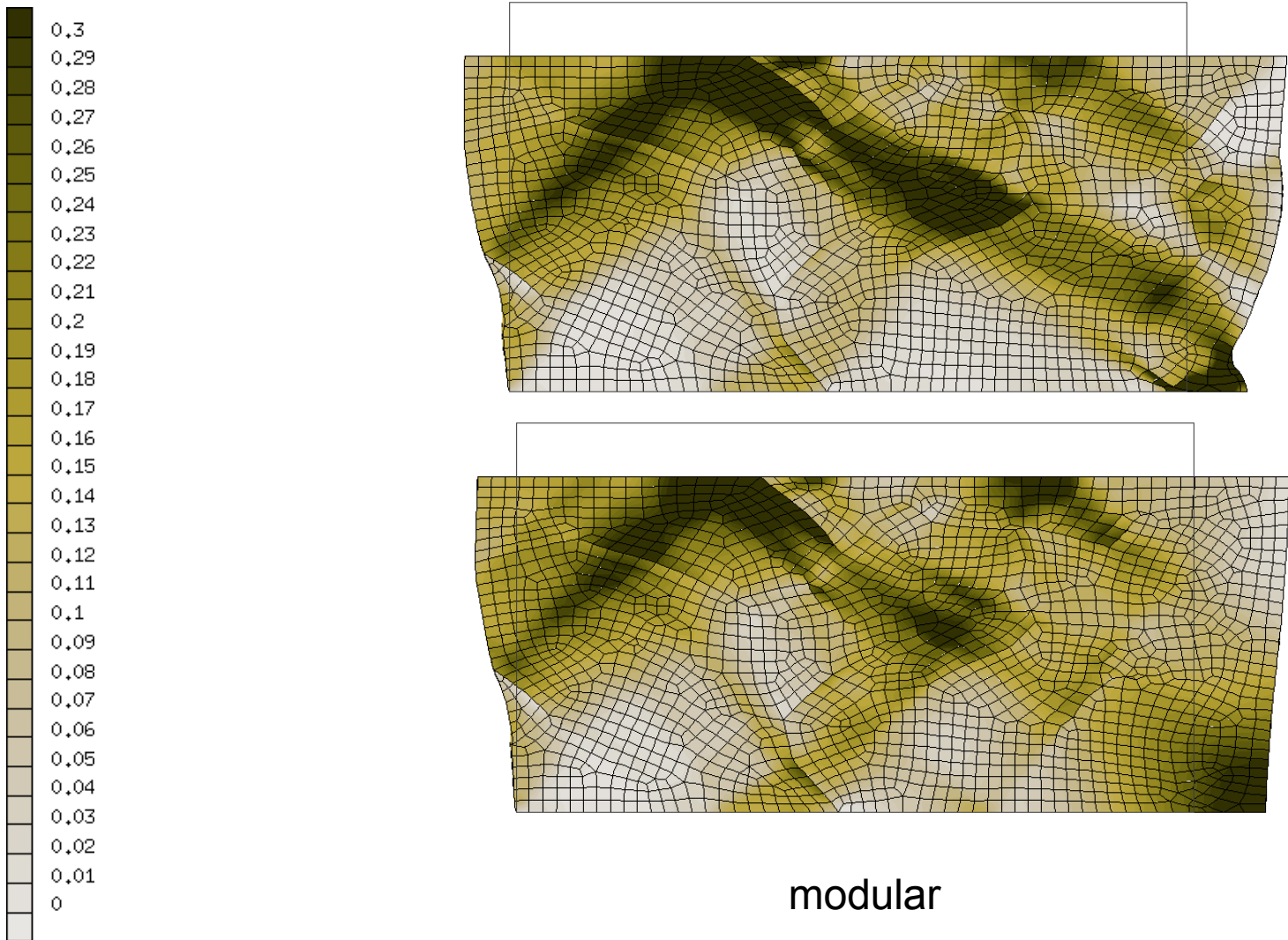
- Modular material point model can incorporate arbitrary constitutive laws within same mesh

J2: 2nd tensor invariant (here: stress tensor)



logarithmic strain
(normal)

full-field dislocation density-based CPFEM

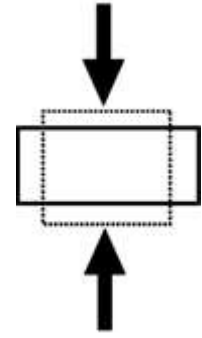
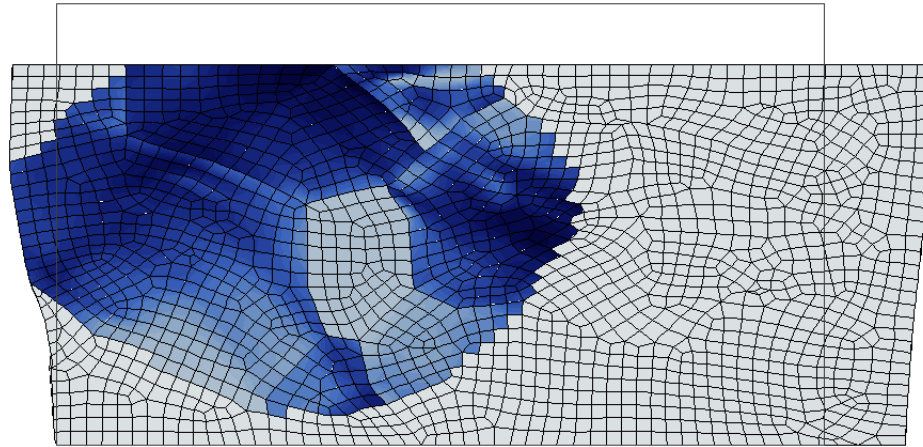
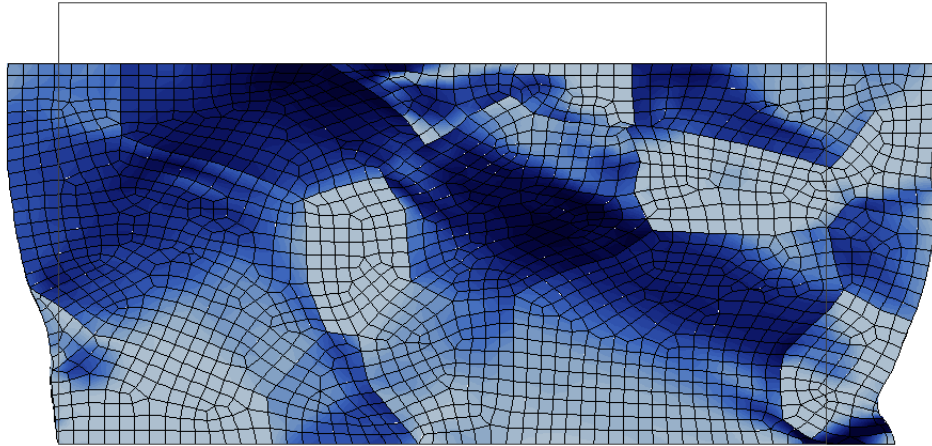
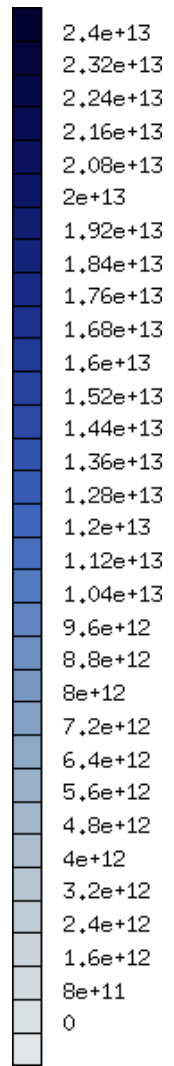


modular



dislocation density

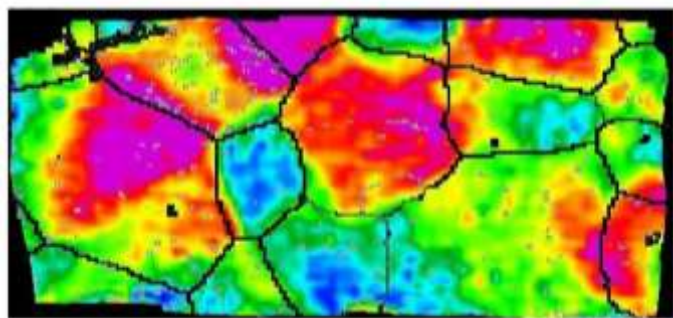
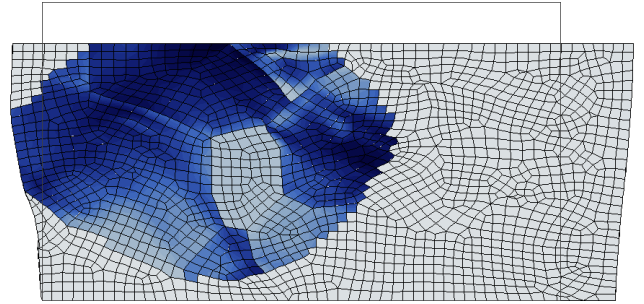
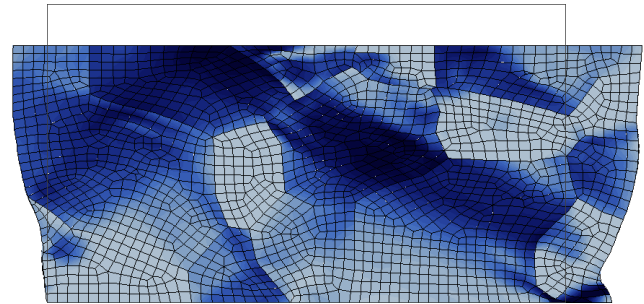
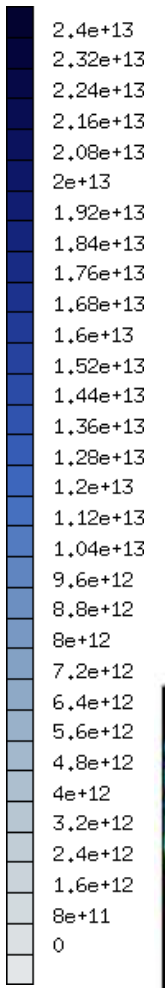
full-field dislocation density-based CPFEM



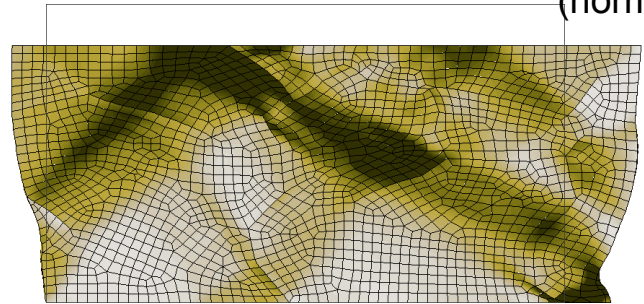
modular



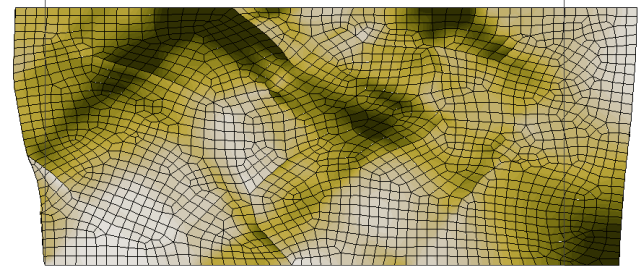
dislocation density



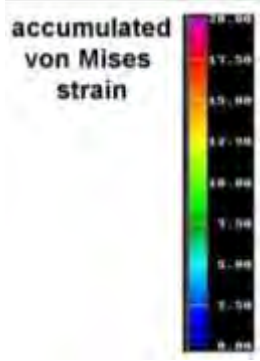
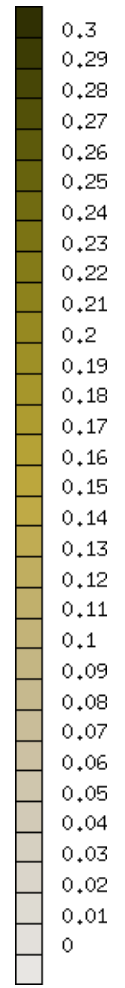
full-field



modular

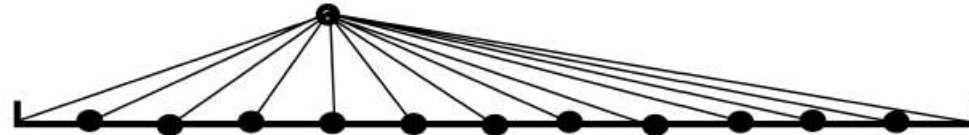


logarithmic strain (normal)



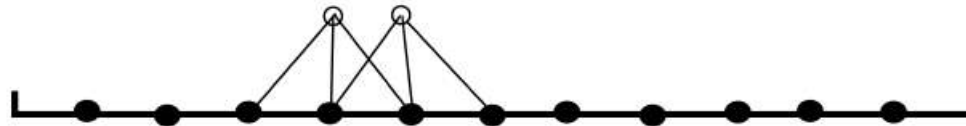
Spectral

One high-order polynomial for WHOLE domain



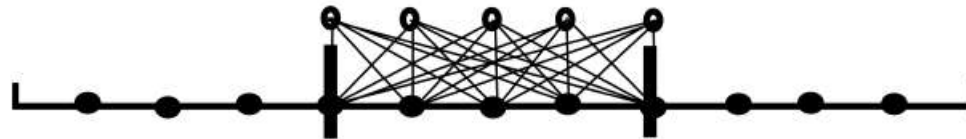
Finite Difference

Multiple Overlapping Low-Order Polynomials



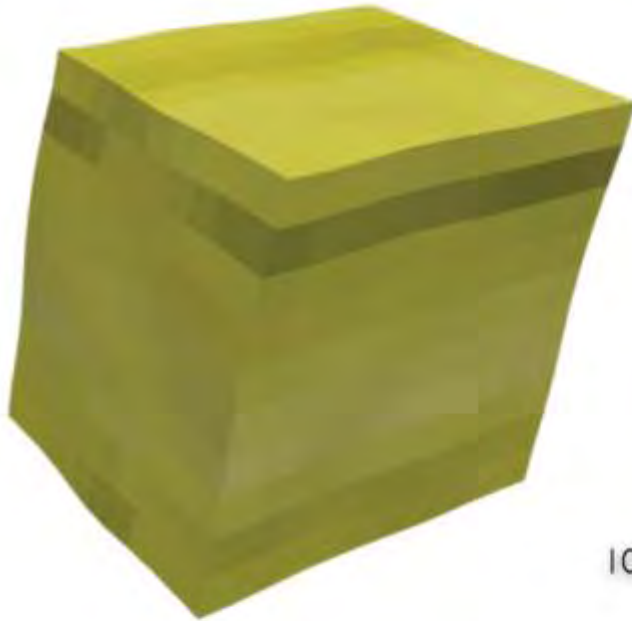
Finite Element

*Non-Overlapping Polynomials,
One per Subdomain*



Picture from: J. P. Boyd. Chebyshev and Fourier spectral methods. Dover, New York, 2001

shear deformation



FEM

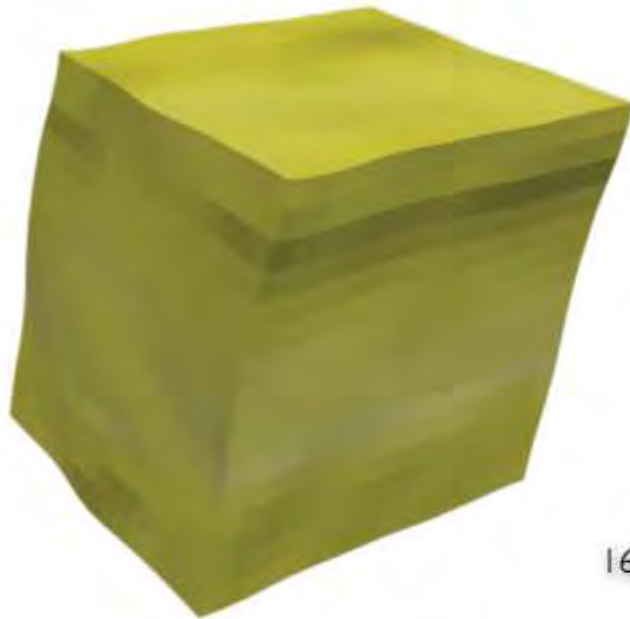
10



FFT



shear deformation



FEM

16



FFT

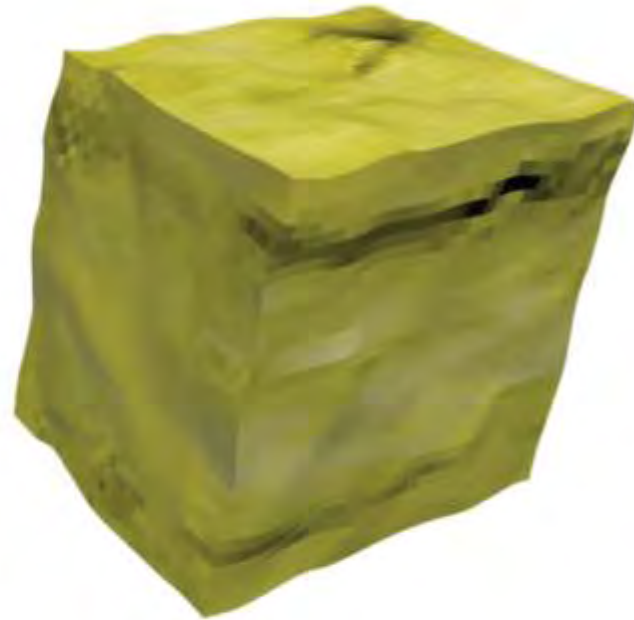


shear deformation



FEM

32



FFT



shear deformation



FEM

64



FFT



shear deformation



FEM

128



FFT



Polycrystal with 100 grains (aluminum alloy) @ $\bar{F}_{23} = 0.25$



F_{23} : FEM solution for 32^3 elements



F_{23} : FFT solution for 32^3 FP



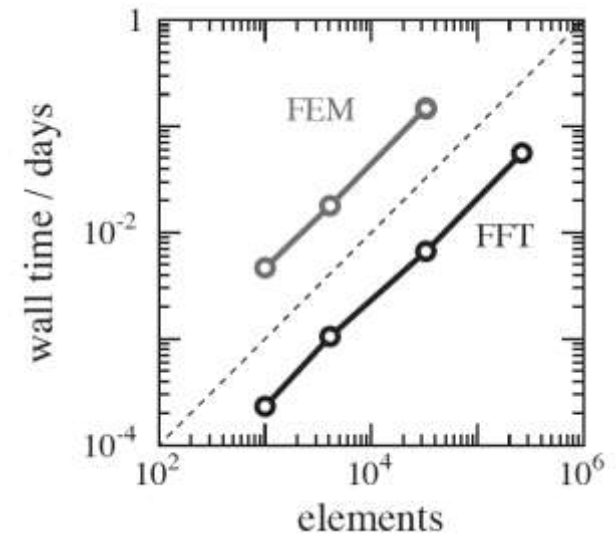
Polycrystal with 100 grains discretized by 64^3 FP @ $\bar{F}_{23} = 0.25$



Deformation gradient (F_{23})



1st Piola-Kirchhoff stress (P_{23})





10^3

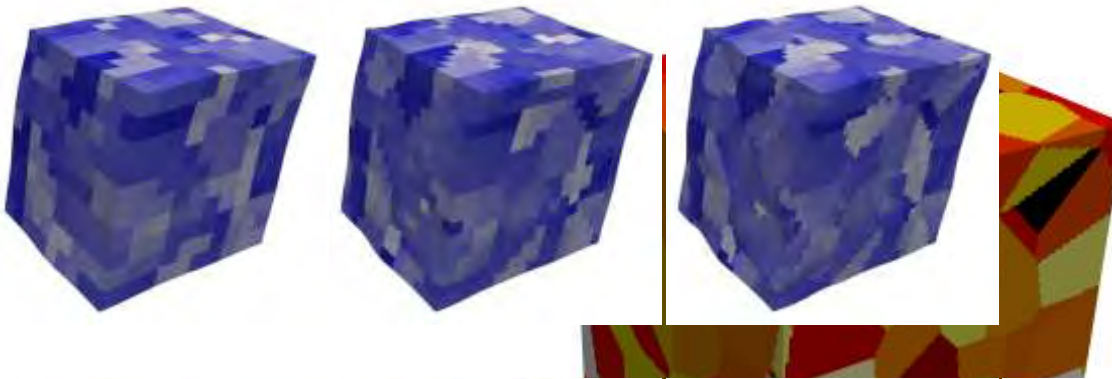
16^3

32^3

64^3

128^3

FEM

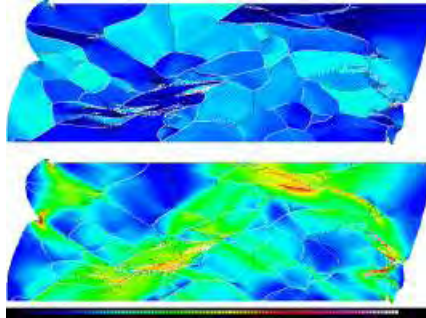


FFT





Nucleation at 50% max. disloc. density

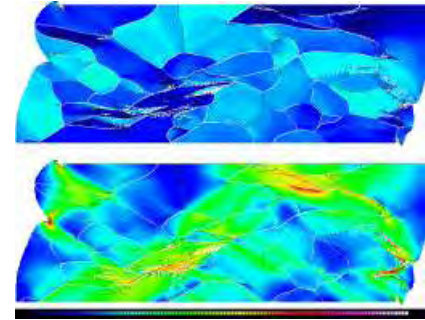


orientation

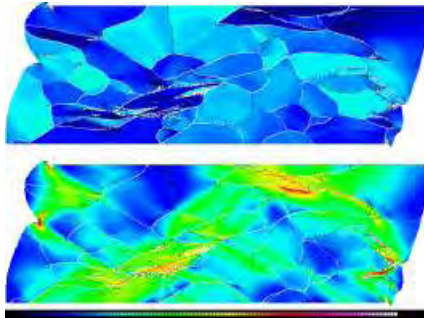
dislocation density

$$\dot{\nu} = m\dot{\rho} = m_0 \exp\left(-\frac{Q}{kT}\right)P$$

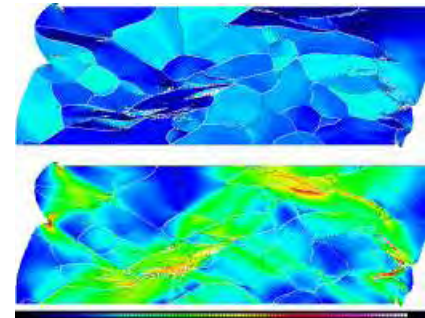
Nucleation at 60% max. disloc. density



Nucleation at 70% max. disloc. density



Nucleation at 80% max. disloc. density



Al, CPFEM and CA starting data, 800 K; site-saturated nucleation in cells with at least 50%, 60%, 70% and 80% of the maximum occurring dislocation density; growth misorientations above 15° : activation energy of grain boundary mobility: 1.46 eV and pre-exponential factor $m_0 = 8.3 \times 10^{-3} \text{ m}^3/(\text{N s})$.



- **Multiscale Crystal Plasticity FEM is a versatile method for boundary condition treatment in crystal mechanics**
- **Include phenomenological or dislocation-based hardening laws**
- **Good at predicting stresses, strains, shapes, contact, texture**
- **One-to-one comparison to experiments**
- **Limits: constitutive aspects where DDD is better suited (limits of statistical and mean field models): size effects, source limitations, bursts, localization, Bauschinger effect, patterning and laminates**
- **Structural size effects**
- **FFT solver**

References on simulation of rolling textures



- D. Raabe, M. Sachtleber, Z. Zhao, F. Roters, S. Zaefferer: *Acta Mater.* 49 (2001) 3433–3441, Micromechanical and macromechanical effects in grain scale polycrystal plasticity experimentation and simulation
- D. Raabe, R. Becker: *Model. Sim. Mater. Sc. Engin.* 8 (2000) 445-462, Coupling of a crystal plasticity finite element model with a probabilistic cellular automaton for simulating primary static recrystallization in aluminum
- D. Raabe, Z. Zhao, S.-J. Park, F. Roters: *Acta Mater.* 50 (2002) 421–440, Theory of orientation gradients in plastically strained crystals
- Z. Zhao, F. Roters, W. Mao, D. Raabe: *Adv. Eng. Mater.* 3 (2001) 984-990, Introduction of A Texture Component Crystal Plasticity Finite Element Method for Industry-Scale Anisotropy Simulations
- D. Raabe, P. Klose, B. Engl, K.-P. Imlau, F. Friedel, F. Roters: *Adv. Eng. Mater.* 4 (2002) 169-180, Concepts for integrating plastic anisotropy into metal forming simulations
- D. Raabe, Z. Zhao, W. Mao: *Acta Mater.* 50 (2002) 4379–4394, On the dependence of in-grain subdivision and deformation texture of aluminium on grain interaction
- D. Raabe and F. Roters: *Intern. J. Plast.* 20 (2004) 339-361, Using texture components in crystal plasticity finite element simulations
- D. Raabe, M. Sachtleber, H. Weiland, G. Scheele, and Z. Zhao: *Acta Mater.* 51 (2003) 1539-1560, Grain-scale micromechanics of polycrystal surfaces during plastic straining
- Z. Zhao, W. Mao, F. Roters, D. Raabe: *Acta Mater.* 52 (2004) 1003–1012, A texture optimization study for minimum earing in aluminium by use of a texture component crystal plasticity finite element method
- D. Raabe, Z. Zhao, F. Roters: *Scripta Materialia* 50 (2004) 1085-1090, Study on the orientational stability of cube-oriented FCC crystals under plane strain by use of a texture component crystal plasticity finite element method
- D. Raabe, Y. Wang, F. Roters: *Comput. Mater. Sc.* 34 (2005) 221-234, Crystal plasticity simulation study on the influence of texture on earing in steel
- Tikhovskiy, D. Raabe, F. Roters: *Scripta Materialia* 54 (2006) 1537-1542, Simulation of the deformation texture of a 17%Cr ferritic stainless steel using the texture component crystal plasticity FE method considering texture gradients
- C.-S. Han, A. Ma, F. Roters, D. Raabe: *Intern. J. Plast.* 23 (2007) 690–710, A Finite Element approach with patch projection for strain gradient plasticity formulations
- B. Liu, D. Raabe, F. Roters, P. Eisenlohr, R. A. Lebensohn: *Model. Sim. Mater Sc. Engin.* 18 (2010) 085005, Comparison of finite element and fast Fourier transform crystal plasticity solvers for texture prediction
- F. Roters, P. Eisenlohr, L. Hantcherli, D.D. Tjahjanto, T.R. Bieler, D. Raabe: *Acta Materialia* 58 (2010) 1152–1211, Overview of constitutive laws, kinematics, homogenization and multiscale methods in crystal plasticity finite-element modeling: Theory, experiments, applications

Concepts for Integrating Plastic Anisotropy into Metal Forming Simulations

By Dierk Raabe,* Peter Klose, Bernhard Engl, Klaus-Peter Imlau, Frank Friedel, and Franz Roters

Modern metal forming and crash simulations are usually based on the finite element method. Aims of such simulations are typically the prediction of the material shape, failure, and mechanical properties during deformation. Further goals lie in the computer assisted lay-out of manufacturing tools used for intricate processing steps. Any such simulation requires that the material under investigation is specified in terms of its respective constitutive behavior. Modern finite element simulations typically use three sets of material input data, covering hardening, forming limits, and anisotropy. The current article is about the latter aspect. It reviews different empirical and physically based concepts for the integration of the elastic-plastic anisotropy into metal forming finite element simulations. Particular pronunciation is placed on the discussion of the crystallographic anisotropy of polycrystalline material rather than on aspects associated with topological or morphological microstructure anisotropy. The reviewed anisotropy concepts are empirical yield surface approximations, yield surface formulations based on crystallographic homogenization theory, combinations of finite element and homogenization approaches, the crystal plasticity finite element method, and the recently introduced texture component crystal plasticity finite element method. The paper presents the basic physical approaches behind the different methods and discusses engineering aspects such as scalability, flexibility, and texture update in the course of a forming simulation.

1. Introduction

The advance of modern well-tailored and optimized materials nowadays provides a huge and steadily-growing application spectrum to customers of formed products. Well established examples are the introduction of high-strength multi-phase steels or 6xxx series aluminum alloys for the automotive industry. The high demands with respect to mechanical properties and surface appearance faced by these materials in the course of metal forming increasingly requires adequate quantitative characterization measures to build a bridge between producers and product designers.

Modern approaches for conducting simulations of plastic deformation are usually based on solving large sets of differential equations associated with a well posed forming problem by use of non-linear finite element methods. Primary

objectives of such simulations are the prediction of the material shape after forming, in particular the thickness distribution; the minimization of material failure in conjunction with the optimization of material flow during forming; and the cal-

[*] Prof. D. Raabe, Dr. F. Roters
Max-Planck-Institut für Eisenforschung GmbH
Abteilung für Mikrostrukturphysik und Umformtechnik
Max-Planck-Str. 1, 40237 Düsseldorf (Germany)
E-mail: raabe@mpie.de

Dr. P. Klose, Dr. B. Engl, Dr. K.-P. Imlau, Dr. F. Friedel
Research & Development, Quality Engineering, and Materials
Testing
Thyssen Krupp Stahl AG, Kaiser-Wilhelm-Strasse 100,
D-47166 Duisburg (Germany)

culuation of the final mechanical properties of the formed sample. Further related essential applications are in the fields of optimizing tool designs, predicting pressing forces, and simulating the final surface appearance of the part. The latter aspect involves both, macroscopic (e.g., wrinkling) as well as microstructural (e.g., ridging, orange peel) mechanisms for changes in surface quality during forming.

Rendering continuum-type metal forming simulations scientifically sound, predictive at the microstructure scale, in good accord with experiment, and at the same time economically rewarding requires that the involved materials are properly specified in terms of their respective constitutive behavior. For this purpose modern finite element simulations typically employ three sets of material input data, covering hardening, forming limits, and anisotropy (Fig. 1). The current article deals with the latter aspect. It reviews both, empirical and physically based concepts for the integration of the elastic-plastic anisotropy into metal forming finite element simulations. Particular pronunciation is placed on the discussion of the crystallographic anisotropy of polycrystalline material rather than on aspects associated with topological or morphological microstructure anisotropy. The various anisotropy concepts which will be reviewed in the following are empirical yield surface approximations, yield surface formulations based on crystallographic homogenization theory, combinations of finite element and homogenization approaches, the crystal plasticity finite element method, and the recently introduced texture component crystal plasticity finite element method.

By providing a survey on the advantages and disadvantages of the various anisotropy concepts the article takes an effort to present both, the present state of the art in the industrial practice as well as advanced approaches which allow the user to include more of the physics associated with crystalline anisotropy. The present state in anisotropy engineering is naturally different between industrial applications and basic science. The use of empirical or semi-empirical polynomials for yield surface approximations is the standard procedure in the industrial practice whereas the various crystal plasticity finite element methods gradually become a standard in the basic materials sciences. The importance of empirical approaches in the industrial practice is due to the fact that they provide short computation times, allow for simple mechanical input data, and are flexible with respect to additional fit points obtained by texture information. An important weakness of empirical approaches lies in the absence of texture update. The prevalence of the crystal plasticity finite element method in basic research is due to its physical basis and the incorporation of texture changes. The major drawback of the

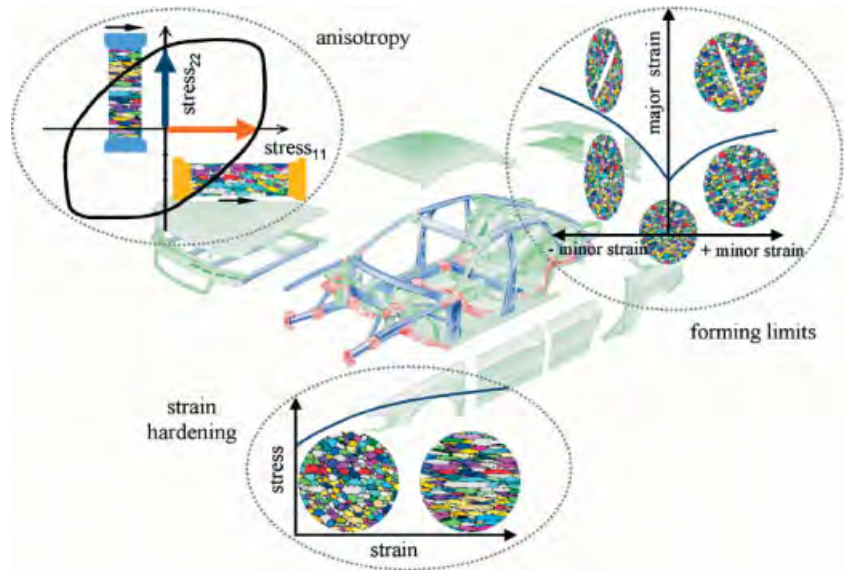


Fig. 1. Modern finite element approaches which aim at simulating realistic metal forming operations typically require three sets of material input data, namely, the strain hardening curve, a forming limit diagram, and information about the crystallographic (and morphological) anisotropy. The article focuses on concepts for integrating elastic-plastic anisotropy.

crystal plasticity approaches are the long calculation times which presently exceed those obtained by use of the yield surface by a factor of 50–100. An improvement in speed of the crystal plasticity methods is attained by the recent introduction of the texture component crystal plasticity finite element method which exceeds the computation times of yield surface calculations only by a factor of 15–25.

The paper has the following plan: First, we give a brief introduction to the physical origin of elastic-plastic crystallographic anisotropy. Second, we present the basic approaches behind the different anisotropy concepts and discuss aspects such as scalability, flexibility, and texture update in the course of forming simulation.

2. From Scalar to Tensorial Materials Engineering

The yield surface represents the generalization of the yield point from uniaxial tensile testing to general stress states. Expanding the yield point into a closed yield surface is only required if the material under inspection shows elastic-plastic anisotropy, i.e., if it deforms differently in different directions. However, such behavior is the rule and not the exception in real materials. Polycrystals with random and thus quasi-isotropic behavior do practically not occur in sheet metal forming operations. Strong crystalline anisotropy is typically encountered in many engineering materials such as alloys based on iron, aluminum, copper, magnesium and titanium.

The physical nature of elastic-plastic anisotropy in metals is the crystalline arrangement of the atoms. Metallic matter usually occurs in polycrystalline form where each grain has a different crystallographic orientation, shape and volume frac-

tion. The distribution of the orientations in a polycrystalline aggregate is referred to as crystallographic texture. The anisotropy of the elastic tensor and the discrete nature of crystallographic slip along densely packed lattice directions on preferred crystal planes also entails a highly anisotropic integral response of such polycrystalline specimens during mechanical loading. While the elastic-plastic deformation of a single crystal and bicrystals as a function of their orientation can nowadays be well predicted, plasticity of polycrystalline matter is less well understood. This is essentially due to the intricate elastic-plastic interactions occurring during co-deformation among the highly anisotropic individual crystals. This interaction leads to strong heterogeneity in terms of strain, stress, and crystal orientation. Another difficulty in tackling the anisotropy of polycrystalline matter lies in the fact that the crystals rotate during forming, owing to the skew symmetric portion of the displacement gradients created by crystal slip. This means that texture and anisotropy gradually change during forming, even under constant strain path conditions. In this context it must be underlined that crystallographic orientation changes are principally non-reversible owing to the orientation sensitivity of strain path changes and the orientation dependence of strain hardening (Not only the beginning of plastic yield but also further strain hardening is a tensorial, i.e., highly anisotropic orientation dependent problem.) This means that - even in the case of very simple strain paths - mechanics and texture should wherever possible be integrated into the simulation concept due to the strong non-linearity of the problem. Artificial separation of the two aspects (continuum mechanics, crystal plasticity mechanics) may entail severe misinterpretations, particularly in the case of strain path changes.

These various aspects which show the complexity of texture and anisotropy and their evolution during forming underline that for an engineering purpose one major aim of polycrystal research must lie in identifying adequate measures for mapping crystallographic anisotropy into classical mathematical methods for predicting large strain plastic deformation. The second even more challenging aim lies in developing methods for predicting also the change of crystal anisotropy during forming on a sound physical basis.

3. The Physical Origin of Crystalline Elastic-Plastic Anisotropy

3.1. Elastic Anisotropy

The elastic anisotropy of crystalline matter departs from the directionality of the electronic bond and the resulting crystal lattice structure. For small deviations of the atoms from their equilibrium positions the reversible elastic response to loads can be approximated by a linear relationship which is referred to as Hooke's law. In this framework the linear elastic constants can be derived as the components of the

second derivative of the electronic potential. The elastic constants can be written in the form of a fourth-rank elastic stiffness tensor C_{ijkl} or in the form of a fourth-rank elastic compliance tensor S_{ijkl} According to

$$\sigma_{ij} = C_{ijkl} \epsilon_{kl} \quad \epsilon_{ij} = S_{ijkl} \sigma_{kl} \quad (1)$$

Symmetry relations and thermodynamic considerations reduce the 81 elastic constants to a set of 3 independent numbers (C_{1111} , C_{1122} , C_{2323}) (Corresponding to (C_{11} , C_{12} , C_{44}) in reduced matrix notation) in the case of cubic crystal symmetry (e.g., Al, Fe, Cu) and to a set of five independent numbers (C_{1111} , C_{1122} , C_{1133} , C_{3333} , C_{2323}) (Corresponding to (C_{11} , C_{12} , C_{13} , C_{33} , C_{44}) in reduced matrix notation) in the case of hexagonal crystal symmetry (e.g., Ti, Mg, Zn). The deviation from elastic isotropy can for cubic crystals be quantified by the so called Zener anisotropy ratio

$$A = \frac{2 C_{2323}}{C_{1111} - C_{1122}} \quad (2)$$

While aluminum has a relatively low elastic anisotropy with $A = 1.215$, iron has a larger Zener ratio of $A = 2.346$. Of all cubic metals tungsten has the lowest deviation from isotropy with a Zener ratio of $A \approx 1$ and lithium the largest with $A = 9.34$.

3.2. Plastic Anisotropy

The plastic anisotropy of crystalline matter also departs from the directionality of the electronic bond and the resulting crystal lattice structure. Both aspects determine which slip planes and which translation vectors (Burgers vectors) serve for the motion of lattice dislocations or the activation of plastically relevant athermal transformations. The main consequence of this anisotropy in the present context is that metals are deformed in a discrete rather than in a continuum fashion rendering plasticity an intrinsically anisotropic property of metals. Assuming that the normalized Burgers vectors b_j and the normalized slip plane normals n_i of the s different slip systems available in a particular crystal lattice are known, their orientation factors m_{ij} can be readily formulated as dyadic products according to

$$m_{ij}^s = n_i^s b_j^s \quad (3)$$

with its symmetric portion being

$$m_{ij}^{\text{sym},s} = \frac{1}{2} (n_i^s b_j^s + n_j^s b_i^s) \quad (\text{crystal coordinates}) \quad (4)$$

when given in crystal coordinates. One must note that all slip vectors used in the equations are normalized. Transforming the latter equation into the sample coordinate system (Fig. 2) leads to

$$m_{kl}^{\text{sym},s} = \frac{1}{2} (a_{ki} n_i^s a_{lj} b_j^s + a_{lj} n_j^s a_{ki} b_i^s) \quad (\text{sample coordinates}) \quad (5)$$

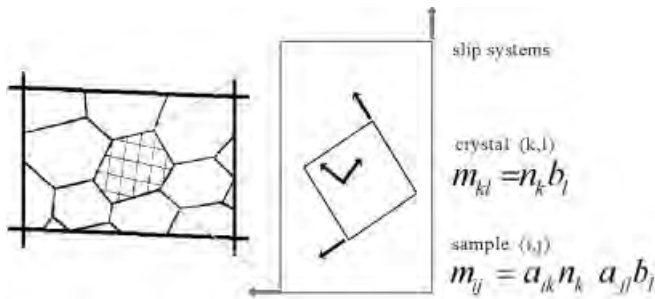


Fig. 2. The plastic anisotropy of crystalline matter departs from the directionality of the electronic bond and the resulting crystal lattice structure. Both aspects determine the slip planes and translation vectors (Burgers vectors) on which lattice dislocations move during plastic deformation. The diagram shows the different coordinate system and the resulting geometrical transformation operations one has to consider in this context.

where a_{ki} and a_{ij} are the transformation matrices between the crystal coordinate system and the sample coordinate system. Using these s different orientation factors $m_{kl}^{sym,s}$ of the s different available slip systems for the transformation of an external load into the slip geometry provides a simple kinematic formulation for the yield surface of a single crystal.

$$m_{kl}^{sym,s} \sigma_{kl} = \tau_{crit,+}^{s, active} \tag{6}$$

$$m_{kl}^{sym,s} \sigma_{kl} = \tau_{crit,-}^{s, active}$$

for the active slip systems, and

$$m_{kl}^{sym,s} \sigma_{kl} < \tau_{crit,+}^{s, nonactive} \tag{7}$$

$$m_{kl}^{sym,s} \sigma_{kl} < \tau_{crit,-}^{s, nonactive}$$

for the non-active slip systems (Fig. 3). One must note that the Einstein summation rule applies in all equations in case not stated otherwise. While the slip dyads of cubic systems typically contain $\langle 111 \rangle$ and $\langle 110 \rangle$ vectors (fcc, bcc) as well as $\langle 111 \rangle$ and $\langle 112 \rangle$ vectors (bcc), hexagonal materials deform by slip on basal, prismatic, and pyramidal systems depending on their cell aspect ratio.

Most points on the single crystal yield surface describe single-slip conditions. In the graphical representation of the yield surface single-slip generally takes place when the stress tensor (in vector transformation notation, using the tensor-vector transformation rule see Equation 8)

$$\sigma_{\lambda}^T = \left\{ \frac{1}{\sqrt{6}} (2\sigma_{33} - \sigma_{11} - \sigma_{22}), \frac{1}{\sqrt{2}} (\sigma_{22} - \sigma_{11}), \sqrt{2}\sigma_{23}, \sqrt{2}\sigma_{13}, \sqrt{2}\sigma_{12} \right\} \tag{8}$$

points at a hyperplane rather than a hyperconus (Fig. 4). Note that the cubes placed in Figure 4 indicate the changing orientation of the external reference system, i.e., of the stress state. Polyslip conditions, as usually required for polycrystal deformation owing to the satisfaction of strain rate compatibility among the grains, are characterized by hyperconus coordinates of the stress state (Fig. 5). The conus positions for the stress can be calculated using a conventional homogenization approach, for instance Taylor-Bishop-Hill theory (indicated by δ^{TBH} in Figure 5). The corresponding multislip positions of the stress tensor, satisfying an externally imposed strain rate,

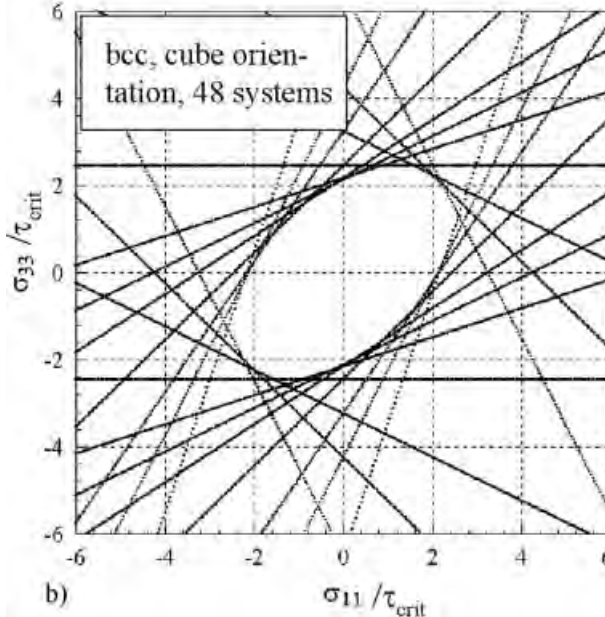
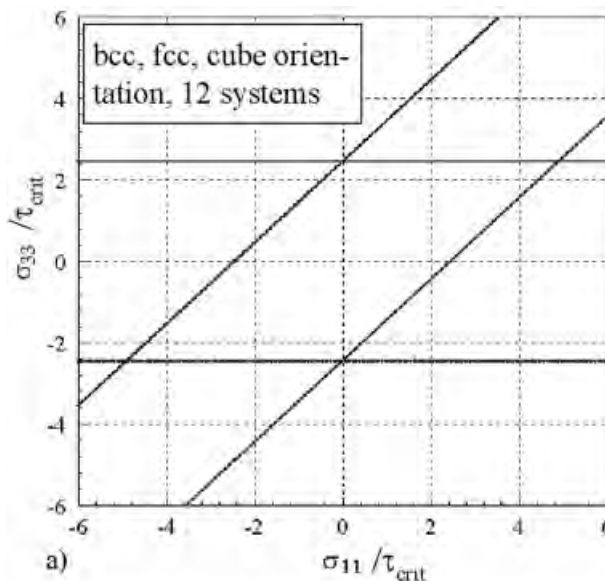


Fig. 3. A simple Schmid-type formulation considering the different orientation factors of all available slip systems which essentially transforms an external load into shear stresses acting on the slip systems provides a kinematic formulation for the yield surface of a single crystal. The yield surface shown in the upper figure (a) was derived using the 12 $\{110\}\langle 111 \rangle$ slip systems. The yield surface shown in the lower figure (b) was derived using the 12 $\{110\}\langle 111 \rangle$, 12 $\{112\}\langle 111 \rangle$, and 24 $\{123\}\langle 111 \rangle$ slip systems (body centered cubic). The figure indicates that body centered cubic alloys therefore behave plastically principally different from face centered cubic alloys.

are then denoted as Taylor positions. It must be noted in this context that the Taylor factor generally takes the form of a stress shape tensor for the crystal yield surface rather than that of a factor owing to its dependence on the strain rate tensor. Its magnitude for a given strain rate determines the kinematic size of the yield surface in the corresponding stress direction characterizing the correct polyslip hyperconus and thus the kinematic portion of the corresponding stress state. The symbols $D^{s=1}$ and $D^{s=2}$ in Figure 5 indicate the single slip strain states from slip systems 1 and 2. Using these two slip

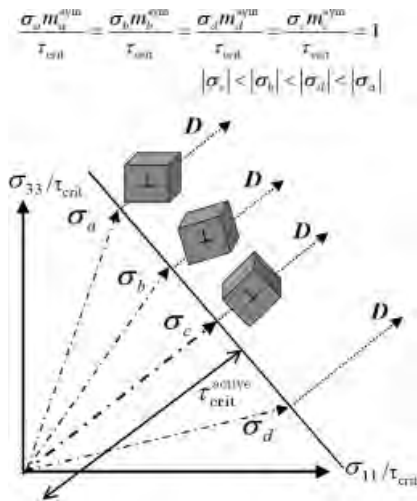


Fig. 4. Most points on the single crystal yield surface describe single-slip conditions. In the graphical representation of the yield surface single-slip generally takes place when the stress state (here given in vector notation) points at a hyperplane rather than a hyperconus. The strain rate tensor is indicated by D and m is the Schmid factor, i.e., the dyadic product of the slip elements. The small cubes placed in the figure indicate the changing relative orientation between the external reference system and the crystal coordinate system.

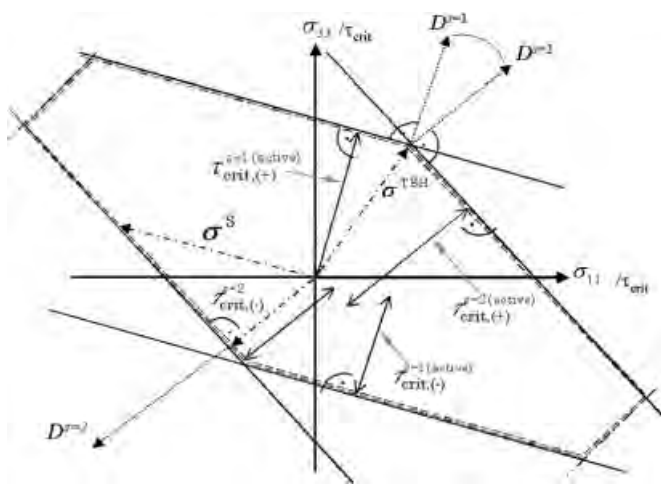


Fig. 5. Polycrystal deformation requires polyslip conditions in order to satisfy strain rate compatibility among the grains. Polyslip states are crystallographically characterized by hyperconus coordinates of the stress state. The conus positions for the stress can be calculated using a conventional homogenization approach, for instance Taylor-Bishop-Hill theory (indicated by δ^{TBH}). The symbols $D^{s=1}$ and $D^{s=2}$ indicate the single slip strain states from slip systems 1 and 2. Using these two slip systems allows one to realize any strain rate state in the respective conus by a linear combination of $D^{s=1}$ and $D^{s=2}$.

systems allows σ to realize any strain rate state in the respective conus by a linear combination of $D^{s=1}$ and $D^{s=2}$. For cubic crystals the yield surface reveals 4 classes of Taylor states for polyslip and one for single slip. These yield states are referred to as

- pentap slip state (5 active slip systems) : ${}^5M_{pq}^i$ (fcc, bcc (reduced): $i = 56$)
- tetra slip (4 active slip systems): ${}^4M_{pq}^j$ (fcc, bcc (reduced): $j = 108$)
- tri slip (3 active slip systems): ${}^3M_{pq}^k$ (fcc, bcc (reduced): $k = 135$)
- bi slip (2 active slip systems): ${}^2M_{pq}^l$ (fcc, bcc (reduced): $l = 66$)
- single slip (1 active slip system): ${}^2M_{pq}^n$ (fcc, bcc (reduced): $n = 24$)

where *fcc* denotes *face centered cubic* and *bcc* denotes *body centered cubic* crystal structure. The term *reduced* indicates that only the first 12 $\{111\}\langle 110 \rangle$ bcc slip systems have been considered here. The number at the end of each row gives the number of different conus cases (and single slip cases) for the respective Taylor state. The total Taylor stress state for a polycrystalline aggregate can for a given external strain rate state then be integrated as a volume weighted sum of all Taylor tensors derived separately for each grain for this boundary condition (Fig. 6).

4. Empirical Approximations of the Yield Surface

The first empirical mathematical description of an anisotropic plastic yield surface was suggested in 1928 by von Mises in the form of a quadratic function.^[1] This approach which was originally designed to empirically approximate the plastic anisotropy of single crystals was in 1948 rendered by Hill^[2] into a generalized form using the Huber-Mises-Hencky approach (Fig. 7a). In Hill's form the yield surface amounts to

$$f(\sigma_{ij}) = (F(\sigma_{22} - \sigma_{33})^2 + G(\sigma_{33} - \sigma_{11})^2 + H(\sigma_{11} - \sigma_{22})^2 + 2L\sigma_{23}^2 + 2M\sigma_{13}^2 + 2N\sigma_{12}^2)^{1/2} \quad (10)$$

where $F, G, H, L, M,$ and N are the anisotropy coefficients. The above equation can be rewritten as

$$f(S_{ij}) = ((G + H)S_{11}^2 + (F + H)S_{22}^2 + (F + G)S_{33}^2 - 2HS_{11}S_{22} - 2GS_{11}S_{33} - 2FS_{22}S_{33} + 2LS_{23}^2 + 2MS_{13}^2 + 2NS_{12}^2)^{1/2} \quad (11)$$

where S_{ij} are the deviatoric stress components. The shape coefficients of Hill's quadratic yield function can be fitted from experimentally obtained mechanical data such as the

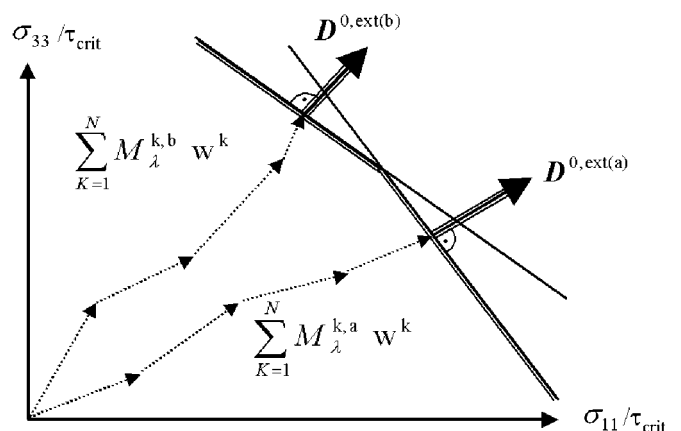


Fig. 6. The Taylor stress state for a polycrystalline aggregate can for a given external strain rate state be integrated as a volume weighted sum of all Taylor factors derived separately for each grain for the respective boundary condition. In this figure M is the Taylor tensor, D the strain rate and w the volume fraction. The counter k sums over all crystals in the aggregate.

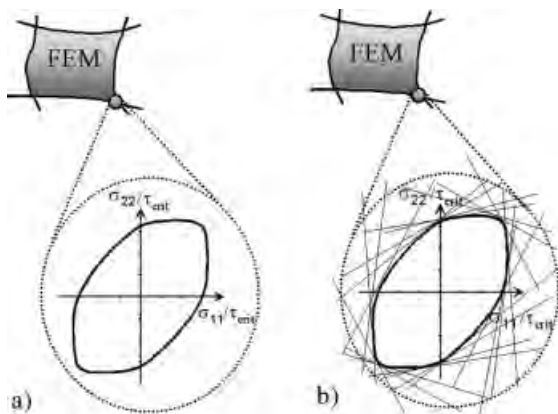


Fig. 7. Schematical presentation of an empirical (a) and of a texture-based (b) yield surface approach. It must be noted though that the actual incorporation of a crystallographic yield surface also requires a functional form.

Lankfort values taken in different directions of a specimen. Scaling can be provided by the yield stress obtained from uniaxial tensile testing. While the Lankfort coefficients and the yield stress can be determined from tensile testing, the direct measurement of mechanical response under complex loads is an intricate task. Although Hill-based anisotropy simulations (referring to the Hill 1948 model) provide decent approximations at least of the initial plastic anisotropy in case of certain iron textures and a number of textures in interstitial free steels, they typically fail to predict the yield shape of high strength steels, austenitic steels, most aluminum alloys, copper, or hexagonal materials. Typical examples where the Hill 1948 yield criterion is not applicable are cup drawing operations of aluminum or copper crystals with six-fold slip symmetry, i.e., with a crystal $\{111\}$ plane parallel to the sheet surface (see paper by Roters and Zhao in this volume). In this case six slip systems have identical Schmid factor relative to the surface which cannot be modeled by the Hill polynomial owing to its quadratic form.

Due to this principle shortcoming a number of optimized empirical anisotropic yield surface concepts with higher order polynomial forms have been proposed in the last decades, such as those introduced later by Hill^[3] and by Barlat^[4] which are better suited for face centered cubic alloys and many body centered cubic steels. In the last years various authors have presented improved empirical yield surface approaches where the yield function can be fitted using both mechanically obtained and even texture-based data.

The chief advantage of using an empirical anisotropic yield surface function as a constitutive law in metal forming finite element simulations is time efficiency and the simple mechanical methods with which it can be derived. The dominant disadvantage of empirical yield surface functions is that the anisotropy of polycrystalline matter generally changes during forming owing to the change of texture. This evolution of anisotropy is not mapped by a corresponding change of the shape of the yield surface. In other words, the same yield surface shape is used throughout one finite element simulation without making a physically meaningful update

of its steadily changing shape. Although empirical constitutive laws can be used to gradually change the yield surface shape during forming, their capability is typically constrained by a lack of physical information about the actual development of the crystallographic texture during forming.

5. Crystallographic Approximations of Elastic-Plastic Anisotropy

5.1. Crystallographic Approximations of Elastic Anisotropy Derived by Homogenization Theory

A typical problem in the field of anisotropy engineering is the approximation of the integral elastic response of a polycrystalline sample under an external load. Although various aspects can principally contribute to the anisotropy of the overall elastic stiffness we concentrate in the following on the influence of the crystallographic texture. The macroscopic elastic properties of a textured polycrystal can be calculated by formulating appropriate volume-weighted means of the individual elastic single crystal tensor, rotated parallel to the respective local coordinate system of each individual crystal. This average value of the integral elastic tensor must therefore take into account all individual orientations of the grains which are described by the orientation distribution function.

An early homogenization approach for the elastic response under an external load was suggested by Voigt, who assumed that in the case of a macroscopically prescribed strain rate state each material portion is in the same strain rate state as the entire sample, irrespective of its spatial position in the specimen. The strain rate would then be homogeneous throughout the sample. However, in a polycrystalline sample, the elastic response typically varies from grain to grain, due to the spatially changing crystal orientation. Since in the Voigt model the prescribed strain rate is the same everywhere in the sample, the stress must vary. The Voigt limit for the elastic response of a polycrystalline sample can thus be calculated by weighting the tensor of the elastic stiffness as a function of orientation with the orientation distribution function. A different approach to treating the homogenization problem in an elastically loaded polycrystalline sample was suggested by Reuss. He suggested that in the case of a macroscopically prescribed stress state each material portion is in the same stress state irrespective of its spatial position in the specimen. The stress would then be homogeneous throughout the specimen. The elastic response may then vary from grain to grain, in accord with the local orientation of the crystal. Since in the Reuss model the prescribed external stress is constant throughout the specimen, the strain must vary according to the local grain orientation. Consequently, the elastic Reuss limit can be calculated for a polycrystal by weighting the tensor of the elastic compliance as a function of orientation

with the orientation distribution function. Since neither the Voigt nor the Reuss method provides reliable approximations to the elastic modulus of a polycrystal, Hill defined an average modulus which consists of the equally weighted results of both above models.

5.2. Crystallographic Approximations of the Yield Surface Derived by Homogenization Theory

Polycrystalline alloys subject to metal forming operations typically develop or inherit morphological textures (e.g., elongated grains, chemical segregation, or second phases with elongated topology entailing directional effects) as well as crystallographic textures (orientation distribution of the crystallites constituting polycrystalline matter). While the former are often less relevant in typical commercial sheet material, the latter strongly determine the overall anisotropy. In the following we will hence concentrate on texture effects on yield anisotropy. Orientation distributions can directly serve as input data for the calculation of the crystallographically determined portion of the yield surface shape using Taylor-Bishop-Hill or self-consistent type approaches (Figs. 3, 7b). This applies for a single crystal yield surface as well as for the homogenization bounds of the polycrystal yield surface (Fig. 8). The major spirit and advantage of the crystallographic yield surface over empirical concepts consists in the fact that it reduces the individual anisotropic behavior of large sets of individual grains comprising a polycrystalline aggregate (10^4 - 10^{10} grains for a typical large scale forming operation) to a simple crystallographic homogenized shape function. It is thus an ideal example of a scale-bridging simulation approach which reduces the tremendous complexity inherent in real microstructures (Fig. 9) to a simple anisotropic function (Fig. 10).

Details about deriving the yield surface from the crystallographic texture of polycrystals are given in [5-11]. The required experimental input textures can be determined using x-ray, neutron, or electron diffraction experiments. Since texture-based yield surface approximations use the complete crystal-

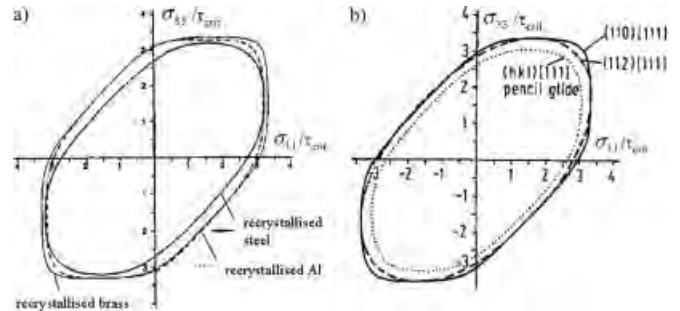


Fig. 8. Some examples of yield functions for different materials calculated by use of the homogenization bounds for their respective polycrystal yield surface. Figure (a) shows yield surface sections for aluminum, steel, and brass. Figure (b) shows yield surface sections for steel using different slip system combinations.

lographic anisotropy information of a specimen they are often superior to empirical approaches which rely on a small set of mechanical parameters. However, modern empirical approaches for the approximation of the yield surface typically use Taylor-Bishop-Hill type crystal simulations on the basis of experimental texture data to provide tangents for a better fit of the yield surface functions. Figure 11 shows the anisotropic effect of some isolated texture components in body centered cubic steels. The $\{111\}\langle 112\rangle$ and the $\{111\}\langle 110\rangle$ texture components each reveal a six-fold symmetry of the shape change with respect to the sheet surface, due to the symmetry of the active Burgers vectors and slip planes. In case that a complete fiber texture exists with a crystal $\langle 111\rangle$ axis parallel to the sheet surface common to all orientations in that sample a very high r-value and a vanishing Δr -value are the consequence. A texture component which is very detrimental to the overall planar anisotropy for instance in ferritic steels is the cube orientation rotated 45° about the normal direction, $\{001\}\langle 110\rangle$. This texture component is often inherited from ferritic hot rolling steps and further sharpened during subsequent cold rolling of many low-carbon steels, most transformer steels, nearly all ferritic stainless steels, and all body centered cubic refractory metals such as molybdenum, tantalum, or niobium. Simulations of this kind would be essential for methods of inverse anisotropy engineering, where one first

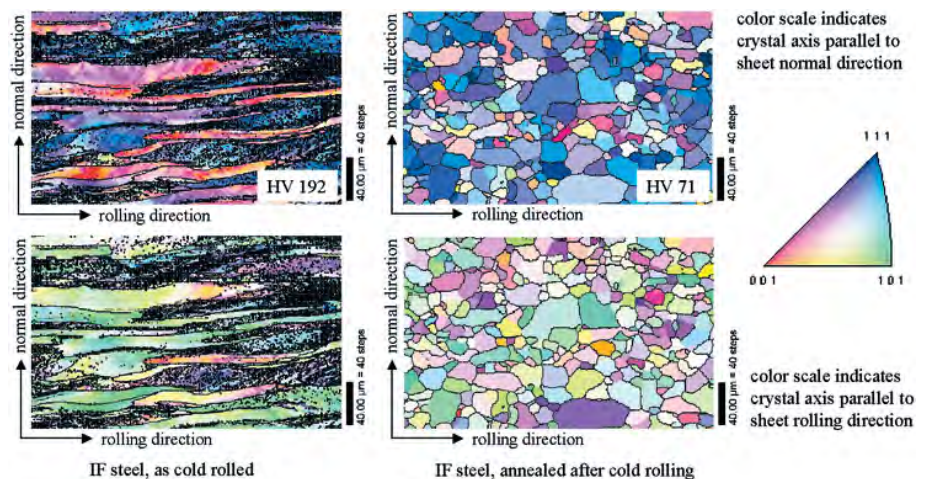


Fig. 9. Real microstructures (here an IF steel) reveal a tremendous complexity not only of the global but also of the local textures. This example shows that the incorporation of textures into finite element formulations requires adequate homogenisation approaches. The upper diagram shows a color scale which indicates the crystal axis parallel to sheet normal direction. The lower graph shows the crystal axis parallel to sheet rolling direction.

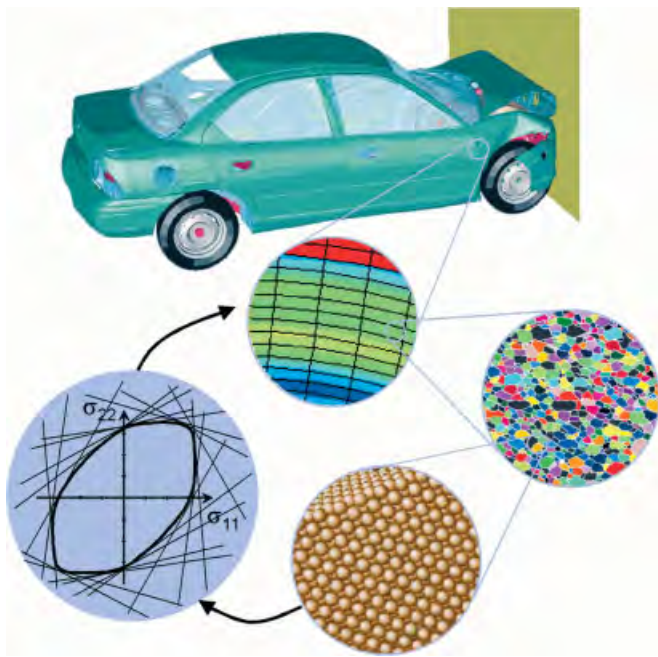


Fig. 10. The overview diagram shows the basic spirit of reducing microstructure complexity into a compact but at the same time physically based crystallographic yield formulation for including anisotropic behavior in metal forming simulations.

identifies those texture components which are most beneficial for a given forming operation (this is not always necessarily a texture which creates a maximum r-value) and subsequently develops processing methods to generate this particular desired texture.

Besides its clear physical basis another advantage of crystallographic yield surface approximations lies in its capability to incorporate both, kinematical and kinetic plasticity effects. In this context it must be considered that the crystallographic texture only gives the respective anisotropic shape function for a particular polycrystalline sample, but the texture dependence of the internal stress and the individual hardness of the different grains are typically ignored by the constitutive laws employed in homogenisation approaches. However, it is principally feasible to generalize the crystallographic yield surface concept by enriching it with the individual strength of each grain. This leads to a formulation of the following kind

$$f(S_{ij}) = \frac{1}{V} \int_V M_{ij}(\mathbf{g}, D_{ij}) \tau_{crit}(D_{ij}, \mathbf{g}) dV \approx \sum_{k=1}^N M_{ij}^k \tau_{crit}^k w^k \quad (12)$$

where $f(S_{ij})$ is the yield surface, V the sample volume, M_{ij} the Taylor shape function obtained by homogenization theory as a function of strain rate D_{ij} and rotation matrix \mathbf{g} , τ_{crit} the flow stress of each individual grain, and w the volume fraction of each grain. An example where kinetic information about the local texture-dependent hardness of the various grains has

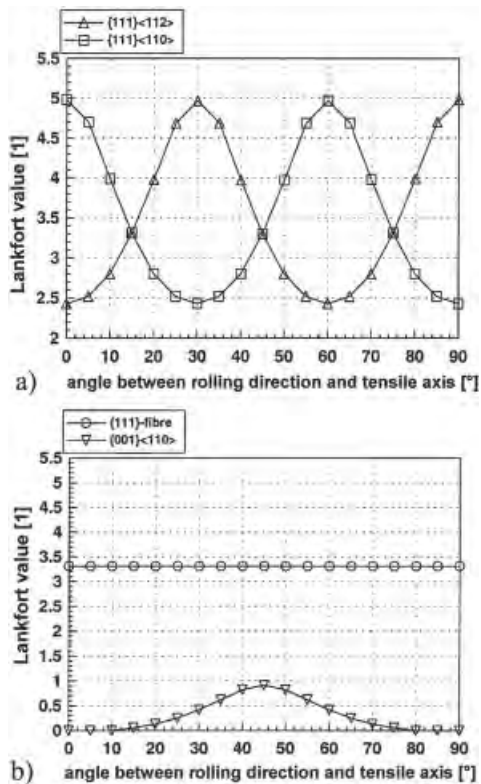


Fig. 11. Anisotropy of some isolated texture components in body centered cubic matter. The $\{111\}\langle 112 \rangle$ and the $\{111\}\langle 110 \rangle$ texture components each reveal a six-fold symmetry of the shape change with respect to the sheet surface, due to the symmetry of the active Burgers vectors and slip planes. In case of a complete $\langle 111 \rangle$ texture fiber with respect to the sheet surface a very high r-value and a vanishing Δr -value is the consequence. A very detrimental texture component is the cube orientation rotated 45° about the normal axis, $\{001\}\langle 110 \rangle$.

been used to approximate a yield surface is given in Figure 12.^[12] The left diagram shows a portion of the planar yield surface as it anisotropically shrinks during partial recrystallization. The right hand side of Figure 12 shows three subsequent time steps of a coupled crystal plasticity FEM - cellular automaton simulation where the upper picture gives the texture in terms of the magnitude of the Rodriguez vector and the lower picture the strength in terms of the dislocation density (black areas are recrystallized). The data from this discrete simulation served as input to the kinematic-kinetic yield surface model.

Although texture-based yield surface approximations have a crisp physical basis in that they incorporate crystal anisotropy in a genuine fashion, they have the shortcoming of ignoring texture changes during forming. This means that – as far as texture update during forming is concerned – there is basically little difference between the predictive capabilities of empirical and texture-based yield surface approximations, particularly if one considers that recent approaches use both, mechanical and texture-related information to fit the yield function. These methods could be referred to as hybrid anisotropic yield criteria or semi-empirical yield criteria.

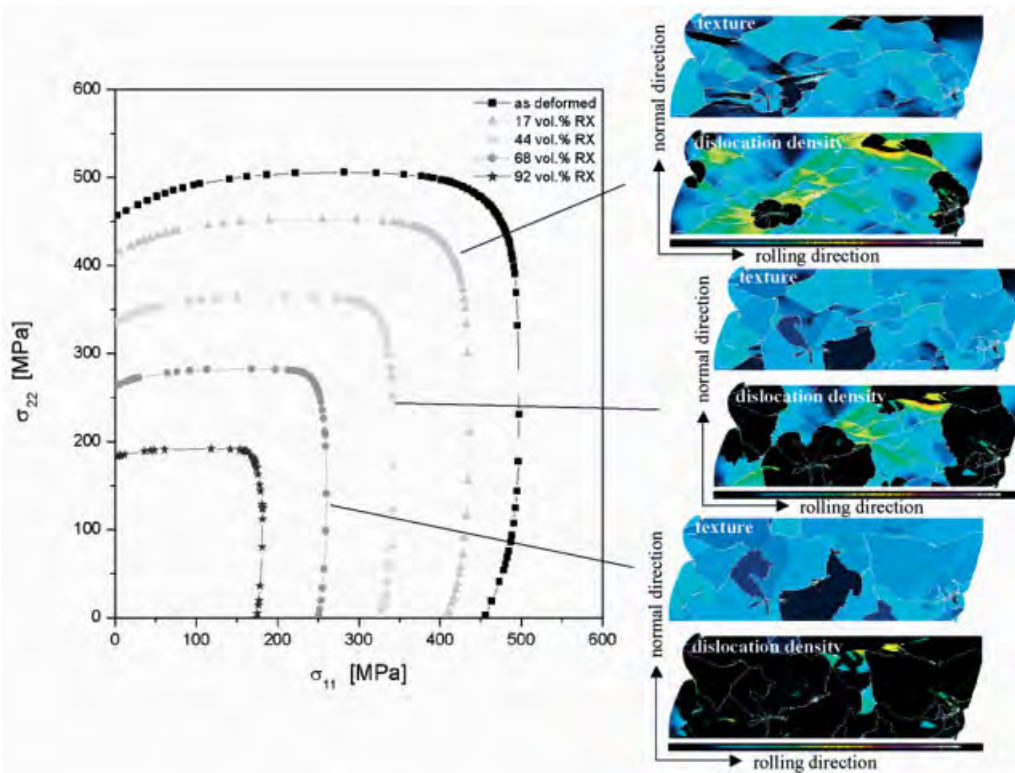


Fig. 12. Coupled crystallographic-kinetic yield functions obtained by including both the texture and the texture dependent flow stress of each individual grain weighted by its respective volume [12]. The left hand side of the diagram shows a portion of the planar yield surface as it anisotropically shrinks during partial recrystallization. The right hand side shows three subsequent time steps of a coupled crystal plasticity FEM - cellular automaton simulation where the upper picture gives the texture in terms of the magnitude of the Rodriguez vector and the lower picture the strength in terms of the dislocation density.

6. Integration of Continuum and Crystal Plasticity Homogenization Models

Recent methods for the approximation of plastic anisotropy aim at combining Taylor-based texture homogenization models with isotropic non-linear finite element simulations.^[13,14] In this approach the deformation tensor after each strain increment is used to prescribe the boundary conditions for a corresponding Taylor simulation using a full constraints or coupled full constraints/grain interaction strain rate homogenization model. Each of the finite elements contains its representative crystallographic texture information in the form of a discrete set of grain orientations. The Taylor factor calculated from homogenization is fed back into the finite element simulation as a correction factor for the flow stress in the ensuing simulation step.

The particular strength of this method lies in the realistic simulation of texture changes under complex boundary conditions. With respect to large scale engineering applications a shortcoming of the approach lies in the fact that a large number of discrete orientations is required for a mathematically correct representation of the texture. This entails long computation times when simulating metal forming operations with complete texture update.

7. Crystal Plasticity Finite Element Simulation

A direct integration of crystal plasticity phenomena into non-linear variational formulations was first suggested by Peirce, Needleman and Asaro.^[15,16] Based on these approaches implicit integration schemes which were for instance developed by Becker^[17] and Kalidindi^[18] are designed in a way which allows one to directly implement them in the form of user-defined subroutines into commercial finite element software packages. The current approaches in this domain provide a direct means for updating the local crystallographic and hardening state of the material via integration of the evolution equations for the crystal lattice orientation and the critical resolved shear stress. The deformation behavior of the crystal volume elements are at each integration point governed by a crystal plasticity model which accounts for discrete plastic deformation by crystallographic slip and for the rotation of the crystal lattice during deformation (Fig. 13). The crystal plasticity finite element models typically use space and time as independent variables and the crystal orientation and the accumulated slip as dependent variable.

In the large-strain constitutive crystal model modified for the present work one assumes the stress response at each macroscopic continuum material point to be poten-

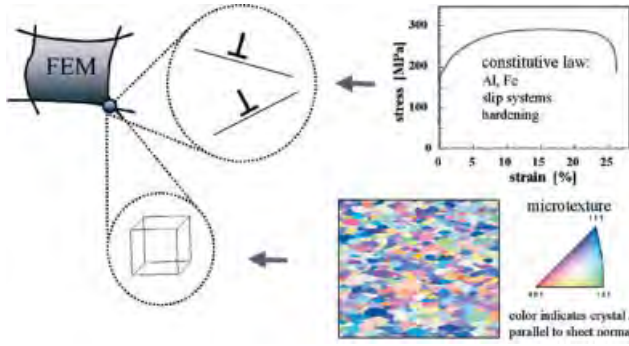


Fig. 13. Schematical presentation of a crystal plasticity finite element formulation for considering and predicting texture-based plastic anisotropy on a grain-for-grain scale.

tially given by one crystal or by a volume-averaged response of a set of grains comprising the respective material point. In case of a multi-grain description the volume averaged stress amounts to

$$\langle \mathbf{T} \rangle = \sum_{k=1}^N (w_k \mathbf{T}_k) \quad (13)$$

where N is the number of grains at each integration point, w_k the volume fraction of each crystal, and T_k the Cauchy stress in the k th crystal. The constitutive equation for the stress in each grain is then expressed in terms of

$$\mathbf{T}^* = \mathbf{C} \mathbf{E}^* \quad (14)$$

where \mathbf{C} is the fourth order elastic tensor and \mathbf{E}^* an elastic strain measure obtained by polar decomposition,

$$\mathbf{E}^* = \frac{1}{2} (\mathbf{F}^{*T} \mathbf{F}^* - \mathbf{1}) \quad (15)$$

which leads to a stress measure which is the elastic work conjugate to the strain measure \mathbf{E}^* ,

$$\mathbf{T}^* = \mathbf{F}^{*-1} (\det(\mathbf{F}^*) \mathbf{T}) \mathbf{F}^{*T} \quad (16)$$

where \mathbf{T} is the symmetric Cauchy stress tensor in the grain, and \mathbf{F}^* is a local elastic deformation gradient defined in terms of the local *total* deformation gradient \mathbf{F} and the local *plastic* deformation gradient \mathbf{F}^P . The relation between the elastic and the plastic portion of \mathbf{F} amounts to

$$\mathbf{F}^* = \mathbf{F} \mathbf{F}^{P-1}, \quad \det(\mathbf{F}^*) > 0, \quad \det(\mathbf{F}^P) = 1 \quad (17)$$

The plastic deformation gradient is given by the flow rule

$$\dot{\mathbf{F}}^P = \mathbf{L}^P \mathbf{F}^P \quad (18)$$

with its crystalline portion

$$\mathbf{L}^P = \sum_{k=1}^N \dot{\gamma}_k \mathbf{m}_k, \quad \dot{\gamma}_k = f(\tau_k - \tau_{k, \text{crit}}), \quad \tau_k \approx \mathbf{L}^* \cdot \mathbf{m}_{k,0} \quad (19)$$

where \mathbf{m}_k are the k dyadic slip products introduced above, $\dot{\gamma}_k$ the shear rates on these systems, and $\tau_{k, \text{crit}}$ the actual critical shear stress on the k th system. For room temperature simulations of aluminum plastic deformation is commonly assumed to occur on the 12 slip systems with $\langle 110 \rangle$ slip directions and $\{111\}$ slip planes, i.e., the slip vectors $b_i = 1/\sqrt{2} (110)$ and $n_i = 1/\sqrt{3} (111)$ are orthonormal. For room temperature simulations of iron plastic deformation can be assumed to occur on 12 $b_i = 1/\sqrt{3} (111)$, $n_i = 1/\sqrt{2} (110)$ systems, 12 $b_i = 1/\sqrt{3} (111)$, $n_i = 1/\sqrt{6} (112)$; systems, and 24 $b_i = 1/\sqrt{3} (111)$, $n_i = 1/\sqrt{14} (123)$ systems.

For many simulations in this field, the strengths of all slip systems at a material point are taken to be equal, i.e., one adopts the Taylor hardening assumption. The hardening as a function of total slip can be assumed to follow experimentally observed or theoretically achieved macroscopic strain hardening behavior obtained from a uniaxial or biaxial test by fitting the experimental data to a standard scalar constitutive equation. The fit can be adjusted by the average Taylor factor of the sample and its change during deformation to give the slip system threshold stress as a function of the accumulated shear. Most of the results presented in this work have been achieved by accounting for latent hardening through the use of an appropriate hardening matrix.

Crystal plasticity finite element models represent elegant tools for detailed joint simulation studies of texture evolution and strain distribution under realistic boundary conditions (Fig. 14). Each integration point can represent one single orientation or map even a larger set of crystals. Although the latter case is principally feasible, it entails long calculation times, rendering the method less practicable for industry-scale applications.

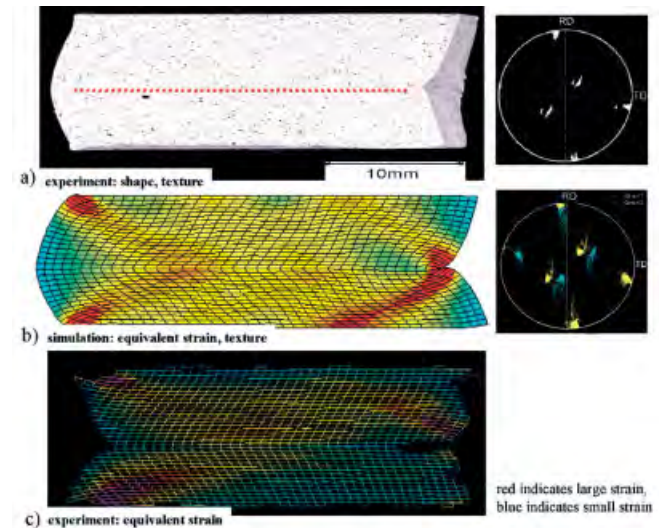


Fig. 14. Example where a grain-for-grain crystal plasticity finite element model was applied for a joint simulation study of texture and strain under realistic boundary conditions. The example shows the deformation of an aluminum bicrystal. The upper diagram shows the shape change of the two grains and the experimentally determined microtexture. The mid section shows the von Mises strain distribution and the microtexture predicted by a corresponding crystal plasticity finite element simulation. The lower graph gives the experimentally determined strain distribution.

8. Integrating Texture Components into the Crystal Plasticity Finite Element Method

A novel physically based and highly time efficient approach for including and updating texture-based elastic-plastic anisotropy during large-strain metal forming operations lies in the integration of crystallographic texture components into the crystal plasticity finite element method.^[19,20] The approach is particularly designed for industrial use since it can be assembled by integrating existing software solutions from crystallography and variational mathematics. The approach is based on directly feeding spherical crystallographic texture components into a non-linear finite element model (Fig 15). The method is used for performing fast simulations of industry-scale metal forming operations of textured polycrystalline materials including texture update. Instead of yield surface concepts or large sets of discrete grain orientations it uses a small set of discrete and mathematically compact Gaussian texture components to map the orientation distribution discretely onto the integration points of a viscoplastic crystal plasticity finite element model. This method drastically enhances the computing speed and precision compared to previous large scale - large strain crystal plasticity finite element approaches.

The texture component method used for this approach is based on the introduction of symmetrical spherical Gauss or Bessel-Gauss functions for the approximation of the orientation distribution.^[21,22] This method provides a small set of compact texture components which are characterized by simple parameters of physical significance (three Euler angles, full width at half maximum, volume fraction). Using this method, only a few texture components are required for map-

ping the complete texture in a mathematical precise form. As starting data one can use both, statistical textures taken from neutron and x-ray measurements or microtextures determined via electron diffraction in the SEM or TEM (Fig. 15). The advantages of this novel approach are at hand. First, one can simulate metal forming operations with complete consideration of elastic-plastic anisotropy and gradual local texture update at the same time (Fig. 16). Second, one can within reasonable computation times quantitatively investigate the texture changes that take place during metal forming (Fig. 17). This information can help to better select which anisotropy concept is appropriate for the different kinds of metal forming boundary conditions and materials. For instance, in cases where only small texture changes take place it can be useful - due to simulation speed - to use one of the conventional yield surface concepts which neglect texture update.

9. Quintessence

The article presented different empirical and physically based concepts for the integration of the elastic-plastic anisotropy of polycrystalline matter into both, small scale and large scale metal forming finite element simulations. The reviewed anisotropy concepts were empirical yield surface approximations, texture-based yield surface formulations based on crystallographic homogenization theory, combinations of finite element and texture-based polycrystal homogenization approaches, the crystal plasticity finite element method, and the recently introduced texture component crystal plasticity finite element method. The article presented the basic physical approaches behind the different methods and reviewed

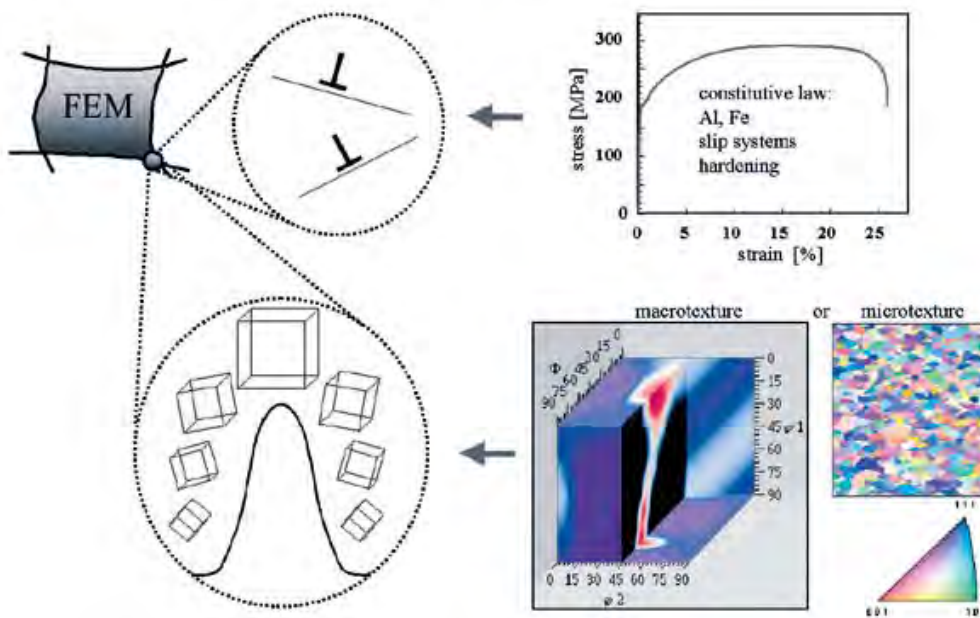


Fig. 15. Schematic presentation of a new physically based and time efficient approach for including and updating texture-based elastic-plastic anisotropy during large-strain metal forming operations [19,20]. The method integrates crystallographic texture components into the crystal plasticity finite element method and is hence referred to as texture component crystal plasticity finite element method (TCCP-FEM). It can make use of both, microtextures or statistical texture information.

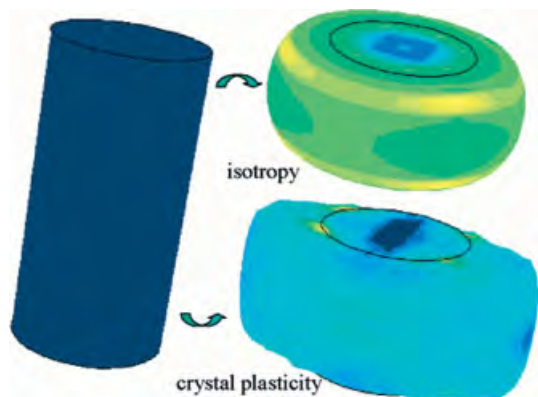


Fig. 16. Example of an isotropic and an anisotropic compression test simulation.

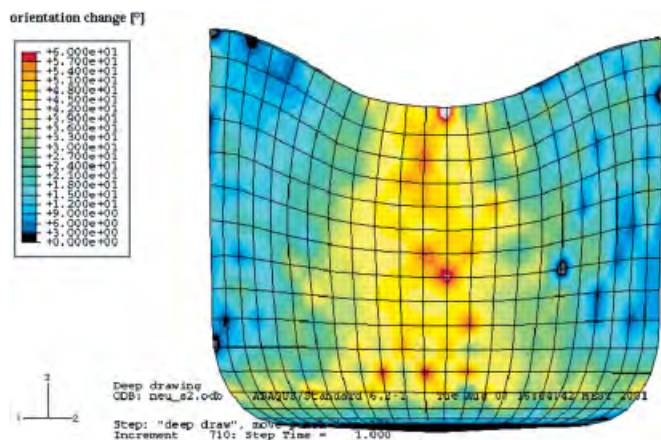


Fig. 17. The texture component crystal plasticity finite element method allows one to quantitatively investigate within reasonable calculation times the texture changes that take place during metal forming. This information is important to select which anisotropy concept is appropriate for the different kinds of metal forming boundary conditions and materials. For instance, in cases where only small texture changes take place it can be useful - due to simulation speed - to use one of the conventional yield surface concepts which neglect texture update.

various engineering aspects such as scalability, flexibility, and texture update in the course of a forming or crash simulation. The present state of the art in anisotropy engineering is naturally different between the day-to-day industry practice and basic science. The use of empirical or semi-empirical higher-order polynomial approximations of the yield surface is a quasi standard operation with respect to industrial applications whereas the various crystal plasticity finite element methods increasingly gain prevalence as a quasi standard in the basic materials sciences. The dominance of empirical approaches in the industrial practice is due to the fact that they provide short computation times, allow for simple mechanical input data, and are flexible with respect to additional fit points obtained by texture information. The major drawback of empirical approaches is the absence of texture and anisotropy update. The dominance of the crystal plasticity finite element method in the basic sciences is due to its sound phys-

ical basis and the complete incorporation of texture and anisotropy update. The major disadvantage of these approaches are the long calculation times which presently exceed those obtained by use of the yield surface roughly by a factor of 50–100. An improvement in speed of the crystal plasticity formulations is attained by the recent introduction of the texture component crystal plasticity finite element method which differs from the speed of yield surface calculations only by a factor of 15–25.

Received: December 21, 2001

- [1] R. V. von Mises, *Zeitschr. Angew. Math. Mech.*, **1928**, 8, 161.
- [2] R. Hill, *Proc. Royal Society* **1948**, 193, 281.
- [3] R. Hill, *Mech. Phys. Solids* **1990**, 38, 405.
- [4] F. Barlat, J. Lian, *Intern. J. Plasticity*, **1989**, 5, 51.
- [5] W. F. Hosford, *The Mechanics of Crystals and Textured Polycrystals*, Oxford University Press **1993**.
- [6] U. F. Kocks, C. N. Tóme, H.-R. Wenk, *Texture and Anisotropy*, Cambridge University Press **1998**.
- [7] H.-J. Bunge, *Kristall u. Technik* (in German) **1970**, 5, 145.
- [8] P. Van Houtte, K. Mols, B. Van Bael, E. Aernoudt, *Texture and Microstructures*, **1989**, 11, 23.
- [9] A. Van Bael, P. Van Houtte, E. Aernoudt, F. R. Hall, L. Pillinger, P. Hartley, C. E. N. Sturgess, *J. Text. Microstruct.*, **1991**, 14–18, 1007.
- [10] D. Raabe, *Computational Materials Science*, Wiley-VCH, Weinheim **1998**.
- [11] D. Raabe, *Comp. Mater. Sci.*, **2000**, 19, 13.
- [12] K. Berner, B. Engl, U. Müller, V. Steininger, E. Till, *Stahl u. Eisen*, **1996**, 116, 52.
- [13] H. Aretz, R. Luce, M. Wolske, R. Kopp, M. Goerdeler, V. Marx, G. Pomana, G. Gottstein, *Modell. Simul. Mater. Sci. Eng.*, **2000**, 8, 881.
- [14] B. Beckers, G. Pomana, G. Gottstein, in *Proceedings of Conference on Constitutive and Damage Modeling of Inelastic Deformation and Phase Transformations*, A. S. Khan (Ed.), Neat Press, Fulton, Maryland, USA, **1998**, p. 305.
- [15] D. Piece, R. J. Asaro, A. Needleman, *Acta Metall.*, **1982**, 30, 1087.
- [16] R. J. Asaro, *Adv. Appl. Mech.*, **1983**, 23, 1.
- [17] R. C. Becker, *Acta Metall. Mater.*, **1991**, 39, 1211.
- [18] S. R. Kalidindi, C. A. Bronkhorst, L. J. Anand, *Mech. Phys. Solids*, **1991**, 40, 537.
- [19] Z. Zhao, F. Roters, W. Mao, D. Raabe, *Adv. Eng. Mater.* **2001**, 3, 984.
- [20] D. Raabe, Z. Zhao, F. Roters, *Steel Research*, **2001**, 72, 421.
- [21] K. Lücke, J. Pospiech, K. H. Virnich, J. Jura, *Acta Metall.*, **1981**, 29, 167.
- [22] K. Helming, R. A. Schwarzer, B. Rauschenbach, S. Geier, B. Leiss, H. Wenk, K. Ullemeier, J. Heinitz, *Z. Metallkd.*, **1994**, 85, 545.

Comparison of finite element and fast Fourier transform crystal plasticity solvers for texture prediction

This article has been downloaded from IOPscience. Please scroll down to see the full text article.

2010 Modelling Simul. Mater. Sci. Eng. 18 085005

(<http://iopscience.iop.org/0965-0393/18/8/085005>)

View [the table of contents for this issue](#), or go to the [journal homepage](#) for more

Download details:

IP Address: 60.229.237.211

The article was downloaded on 30/10/2010 at 05:32

Please note that [terms and conditions apply](#).

Comparison of finite element and fast Fourier transform crystal plasticity solvers for texture prediction

B Liu^{1,3}, D Raabe^{1,3}, F Roters¹, P Eisenlohr¹ and R A Lebensohn²

¹ Max-Planck-Institut für Eisenforschung, Max-Planck-Str. 1, 40237 Düsseldorf, Germany

² MST8-MS G755, Los Alamos National Laboratory, Los Alamos, NM, 87545, USA

E-mail: d.raabe@mpie.de (D Raabe) and b.liu@mpie.de (B Liu)

Received 16 December 2009, in final form 26 July 2010

Published 27 October 2010

Online at stacks.iop.org/MSMSE/18/085005

Abstract

We compare two full-field formulations, i.e. a crystal plasticity fast Fourier transform-based (CPFFT) model and the crystal plasticity finite element model (CPFEM) in terms of the deformation textures predicted by both approaches. Plane-strain compression of a 1024-grain ensemble is simulated with CPFFT and CPFEM to assess the models in terms of their predictions of texture evolution for engineering applications. Different combinations of final textures and strain distributions are obtained with the CPFFT and CPFEM models for this 1024-grain polycrystal. To further understand these different predictions, the correlation between grain rotations and strain gradients is investigated through the simulation of plane-strain compression of bicrystals. Finally, a study of the influence of the initial crystal orientation and the crystallographic neighborhood on grain rotations and grain subdivisions is carried out by means of plane-strain compression simulations of a 64-grain cluster.

(Some figures in this article are in colour only in the electronic version)

1. Introduction

Deformation texture modeling started with the Taylor full-constraints model (1938) [1] using the simplest approximation of equal strain partitioning in a grain aggregate. Owing to this stiff iso-strain formulation and the strong discrepancy between experiments and corresponding predictions this approach was later modified via a global relaxation approximation of some of these strain constraints [2, 3] leading to the relaxed-constraints Taylor models. Later variants, which can be referred to as grain-cluster or grain interaction models, considered local grain

³ Authors to whom any correspondence should be addressed.

neighborhood relaxations such as Van Houtte's 2-grain-cluster LAMEL model and the modified LAMEL model (ALAMEL model) [4, 5], a grain relaxation model proposed by Evers *et al* [6], and the 8-grain-interaction GIA model of Gottstein and co-workers [7, 8].

Other models cast the mean-field homogenization problem in the form of an ellipsoidal inclusion in an infinite matrix as originally suggested for elastic materials by Eshelby [9]. An extension of this approach to nonlinear constitutive response was suggested by Hill [10]. Molinari *et al* [11] and Lebensohn and Tomé [12] later proposed a self-consistent integral formalism which links effective and grain average stresses and strain rates.

The first full-field crystal plasticity calculations were performed by Peirce *et al* in 1982 [13] using a 2D crystal plasticity finite element method (CPFEM) simulation. The term 'full-field' indicates that both long-range and short-range grain interactions are considered, and the micromechanical fields resolved on a discrete grid. In the CPFEM case a variational solution is achieved for the equilibrium of the forces and the compatibility of the displacements using the principle of virtual work for a volume that is discretized into finite elements. The essential step which renders the deformation kinematics of this approach a crystal plasticity formulation is the fact that the velocity gradient is written in dyadic form (i.e. in terms of the sum of the contributions of the different active slip systems). This reflects the tensorial crystallographic nature of the underlying defects that lead to shear and consequently, to both shape changes (symmetric part) and lattice rotations (skew-symmetric part). These simulations were later extended to a polycrystalline arrangement by Harren *et al* [14, 15] using a 2D set-up with two or three slip systems. Becker performed simulations on the basis of the 12 slip systems of the face-centered cubic (FCC) crystal structure. Using a 3D model for the crystallographic degrees of freedom he calculated channel-die deformation of a columnar polycrystal aggregate [16] and of a single crystal [17]. Since then, CPFEM methods became increasingly popular, particularly to tackle sub-grain scale problems, using meshes with sub-grain resolutions and, in occasions, complex 2D and 3D grain arrangements [18–25].

Following the pioneering work of Suquet and co-workers [26, 27] for linear and nonlinear composites, Lebensohn [28] introduced an alternative full-field crystal plasticity formulation by applying a FFT-based algorithm in conjunction with Green's function method, to solve the governing equations for heterogeneous media (e.g. see Mura [29]). This approximation solves the equilibrium equations under the constraint of strain compatibility for materials with periodic microstructure, which can be generated by periodic repetition of a unit cell. This full-field crystal plasticity fast Fourier transform (CPFFT) approach provides an alternative to the CPFEM model with periodic boundary conditions [30]. In general, for the same spatial resolution, the CPFFT approach is a very efficient alternative compared with CPFEM with periodic boundary conditions. This higher numerical performance of CPFFT is related to the repetitive use of the efficient FFT algorithm, avoiding the time-consuming inversion of large matrices, needed under CPFEM. Although the exact reduction in computation time that it is obtained using CPFFT instead of CPFEM is obviously problem-dependent, it is typically from one to several orders of magnitude [30].

The aim of this work is to analyze and compare the predictions of the CPFFT and CPFEM models for deformation textures of FCC polycrystals. We simulate the rolling texture evolution of a 1024-grain representative volume element (RVE) representing an AA1200 aluminum polycrystal under plane-strain boundary conditions (i.e. an approximation of a rolling process) using the CPFFT and the CPFEM models. To further understand the different predictions of both models, the correlation between grain rotations and strain gradients is next investigated through the simulation of plane-strain compression of bicrystals at different discretization levels. Finally, a study of the influence of the initial crystal orientation and the crystallographic neighborhood on grain rotations and grain subdivisions is carried out by means of plane-strain

compression simulations of a 64-grain RVE with four important orientation components clustered in random order.

2. Comparison of the CPFEM and the CPFEM full-field model formulations

2.1. General

Constitutive models define the relation between the symmetric Cauchy stress tensor σ and the strain or strain-rate tensor at a material point level. The material points where the constitutive equations are actually solved can be the set of regular Fourier points, in the case of the CPFEM model; or the Gaussian integration points, in the case of the CPFEM model.

What distinguishes full-field crystal plasticity models from Taylor and grain-cluster approximations is that they solve the equilibrium equations ($\sigma_{ij,j} + f_i^V = 0$) numerically, rather than assuming Taylor-like iso-strain conditions (σ_{ij} is the stress and f_i^V the body force).

The CPFEM model used in this work is based on the Lippmann–Schwinger integral equation for the determination of the strain field in periodic heterogeneous materials [31]. The method was originally developed by Suquet and co-workers [26, 27] as a fast algorithm to compute the elastic and elastoplastic effective and local response of composites, and was later adapted by Lebensohn *et al* [28, 32, 33] to calculate also viscoplastic deformation of complex 3D polycrystalline aggregates.

The CPFEM model used in this comparison is based on the implementation of Kalidindi and Anand [23, 34, 35], which is based on a constitutive viscoplastic law and a phenomenological hardening model.

In this paper we only give a concise comparison of the two models concerning the constitutive formulations, the numerical framework used for solving the equilibrium equations. The same crystal plasticity constitutive equation and hardening law of the two models are briefly mentioned. More details are given in [33, 36].

2.2. CPFEM model: theoretical framework

The method relies on the fact that the local response of a heterogeneous medium can be obtained from convolution integrals between Green functions associated with the micromechanical fields of an equivalent linear homogeneous medium with eigenstrains, and a polarization field in which one collects the actual heterogeneity of the medium, including any possible nonlinearity of the local mechanical behavior. For periodic media, Fourier transforms can be used to reduce these convolution integrals in real space to a simple product in Fourier space between the polarization field and an appropriate kernel function. The FFT algorithm can be used to transform the polarization field into Fourier space and to anti-transform the aforementioned product back to real space. However, since the actual polarization field depends precisely on the *a priori* unknown mechanical fields, and the viscoplastic constitutive behavior determines a strong mechanical contrast in local properties, an iterative scheme based on augmented Lagrangians [27] needs to be implemented to obtain, upon convergence, a compatible strain-rate field and an equilibrated stress field, related to each other through the nonlinear constitutive equation.

The periodic unit cell representing the polycrystal is discretized into $N_1 \times N_2 \times N_3$ Fourier points, determining a regular grid in the Cartesian space $\{x^d\}$ and a corresponding grid in Fourier space $\{\xi^d\}$. A velocity gradient $V_{i,j}$ that can be decomposed into a symmetric strain-rate and a antisymmetric rotation rate, i.e. $V_{i,j} = \dot{E}_{ij} + \dot{\Omega}_{ij}$, is imposed to the unit cell. The local strain-rate field $\dot{\epsilon}_{ij}(\mathbf{x}) = \frac{1}{2}(v_{i,j}(\mathbf{x}) + v_{j,i}(\mathbf{x}))$ is a function of the local velocity field,

and both can be split into its average and a fluctuation term: $\hat{\epsilon}_{ij}(v_k(\mathbf{x})) = \hat{E}_{ij} + \tilde{\epsilon}_{ij}(\tilde{v}_k(\mathbf{x}))$, where $v_i(\mathbf{x}) = \hat{E}_{ij}x_j + \tilde{v}_i(\mathbf{x})$. The velocity fluctuation field $\tilde{v}_k(\mathbf{x})$ has to be periodic across the boundary of the unit cell, and the traction field antiperiodic, to meet equilibrium on the boundary between contiguous unit cells.

The local constitutive relation between the strain rate $\hat{\epsilon}_{ij}(\mathbf{x})$ and the deviatoric stress $\sigma'_{ij}(\mathbf{x})$ is given by the rate-sensitivity equation for single-crystal plasticity:

$$\hat{\epsilon}_{ij}(\mathbf{x}) = \sum_{s=1}^{N_s} m_{ij}^s(\mathbf{x}) \dot{\gamma}^s(\mathbf{x}) = \dot{\gamma}_o \sum_{s=1}^{N_s} m_{ij}^s(\mathbf{x}) \left(\frac{|m^s(\mathbf{x}) : \sigma'(\mathbf{x})|}{\tau_c^s(\mathbf{x})} \right)^n \text{sgn}(m^s(\mathbf{x}) : \sigma'(\mathbf{x})), \quad (2.2.1)$$

where m_{ij}^s , $\dot{\gamma}^s$ and τ_c^s are, respectively, the symmetric Schmid tensor, the shear rate and the threshold stress of slip system (s); n is the rate-sensitivity exponent, $\dot{\gamma}_o$ is the reference shear rate and N_s is the number of slip systems in the single crystal. With $p(\mathbf{x})$ being the hydrostatic pressure field, the Cauchy stress field can be written as

$$\sigma_{ij}(\mathbf{x}) = L_{ijkl}^o \hat{\epsilon}_{kl}(\mathbf{x}) + \varphi_{ij}(\mathbf{x}) - p(\mathbf{x}) \delta_{ij}. \quad (2.2.2)$$

The polarization field $\varphi_{ij}(\mathbf{x})$ is given by

$$\varphi_{ij}(\mathbf{x}) = \sigma'_{ij}(\mathbf{x}) - L_{ijkl}^o \hat{\epsilon}_{kl}(\mathbf{x}), \quad (2.2.3)$$

where L^o is the stiffness of a linear reference medium (note that the particular choice of L^o changes the rate of convergence of the numerical algorithm but not the converged results). Combining equation (2.2.2) with the equilibrium and the incompressibility conditions gives

$$\begin{cases} L_{ijkl}^o v_{k,lj}(\mathbf{x}) + \varphi_{ij,j}(\mathbf{x}) - p_{,i}(\mathbf{x}) = 0, \\ v_{k,k}(\mathbf{x}) = 0. \end{cases} \quad (2.2.4)$$

The auxiliary system for the determination of Green's functions is then given by

$$\begin{cases} L_{ijkl}^o G_{km,lj}(\mathbf{x} - \mathbf{x}') + H_{m,i}(\mathbf{x} - \mathbf{x}') + \delta_{im} \delta(\mathbf{x} - \mathbf{x}') = 0, \\ G_{km,k}(\mathbf{x} - \mathbf{x}') = 0. \end{cases} \quad (2.2.5)$$

After some manipulation, the convolution integrals that give the velocity and velocity-gradient deviation fields are

$$\tilde{v}_k(\mathbf{x}) = \int_{\mathbb{R}^3} G_{ki,j}(\mathbf{x} - \mathbf{x}') \varphi_{ij}(\mathbf{x}') d\mathbf{x}', \quad (2.2.6)$$

$$\tilde{v}_{i,j}(\mathbf{x}) = \int_{\mathbb{R}^3} G_{ik,jl}(\mathbf{x} - \mathbf{x}') \varphi_{kl}(\mathbf{x}') d\mathbf{x}', \quad (2.2.7)$$

Convolution integrals in direct space are products in Fourier space:

$$\hat{\tilde{v}}_k(\boldsymbol{\xi}) = (-i\xi_j) \hat{G}_{ki}(\boldsymbol{\xi}) \hat{\varphi}_{ij}(\boldsymbol{\xi}), \quad (2.2.8)$$

$$\hat{\tilde{v}}_{i,j}(\boldsymbol{\xi}) = \hat{\Gamma}_{ijkl}(\boldsymbol{\xi}) \hat{\varphi}_{kl}(\boldsymbol{\xi}), \quad (2.2.9)$$

where the symbol '^' indicates a Fourier transform. The Green operator in equation (2.2.9) is defined as $\Gamma_{ijkl} = G_{ik,jl}$. The tensors $\hat{G}_{ij}(\boldsymbol{\xi})$ and $\hat{\Gamma}_{ijkl}(\boldsymbol{\xi})$ can be calculated by taking Fourier transform to system (2.2.5) (see [33] for details), resulting in

$$\hat{G}_{ij}(\boldsymbol{\xi}) = A_{ij}^{-1}(\boldsymbol{\xi}), \quad (2.2.10)$$

$$\hat{\Gamma}_{ijkl}(\boldsymbol{\xi}) = -\xi_j \xi_l \hat{G}_{ik}(\boldsymbol{\xi}), \quad (2.2.11)$$

where $A_{ik}(\boldsymbol{\xi}) = \xi_l \xi_j L_{ijkl}^o$.

2.3. CPFEM model: numerical algorithm

Assigning initial values to the strain-rate field in the regular grid $\{\mathbf{x}^d\}$ (e.g. using a ‘Taylor’ guess: $\tilde{\varepsilon}_{ij}^{(0)}(\mathbf{x}^d) = 0 \Rightarrow \dot{\varepsilon}_{ij}^{(0)}(\mathbf{x}^d) = \dot{E}_{ij}$), and computing the corresponding stress field $\sigma'_{ij}{}^{(0)}(\mathbf{x}^d)$ from the local constitutive relation (equation (2.2.1)), gives an initial guess for the polarization field in direct space $\phi_{ij}^{(0)}(\mathbf{x}^d)$ (equation (2.2.3)), and its Fourier transform $\hat{\phi}_{ij}^{(0)}(\boldsymbol{\xi}^d)$.

Choosing the initial guess of an auxiliary stress field λ_{ij} (i.e. the Lagrange multiplier associated with the compatibility constraints) as $\lambda_{ij}^{(0)}(\mathbf{x}^d) = \sigma'_{ij}{}^{(0)}(\mathbf{x}^d)$, the iterative procedure based on augmented Lagrangians [27] reads as follows.

With the polarization field after iteration n being known, the $n + 1$ th iteration starts by computing the new guess for the kinematically admissible strain-rate deviation field:

$$\hat{d}_{ij}^{(n+1)}(\boldsymbol{\xi}^d) = -\hat{\Gamma}_{ijkl}^{\text{sym}}(\boldsymbol{\xi}^d)\hat{\phi}_{kl}^{(n)}(\boldsymbol{\xi}^d), \quad \forall \boldsymbol{\xi}^d \neq 0; \quad \text{and} \quad \hat{d}_{ij}^{(n+1)}(\mathbf{0}) = 0, \quad (2.3.1)$$

where $\hat{\Gamma}_{ijkl}^{\text{sym}}$ is the Green operator (equation (2.2.11)), appropriately symmetrized. The corresponding field in real space is thus obtained by application of the inverse FFT, i.e.

$$\tilde{d}_{ij}^{(n+1)}(\mathbf{x}^d) = \text{FFT}^{-1}[\hat{d}_{ij}^{(n+1)}(\boldsymbol{\xi}^d)] \quad (2.3.2)$$

and the new guess for the deviatoric stress field $\sigma'_{ij}{}^{(n+1)}$ is calculated from the set of nonlinear equations (omitting subindices):

$$\begin{aligned} \sigma'^{(n+1)}(\mathbf{x}^d) + L^o : \dot{\gamma}_o \sum_{s=1}^{N_s} m^s(\mathbf{x}^d) \left(\frac{m^s(\mathbf{x}^d) : \sigma'^{(n+1)}(\mathbf{x}^d)}{\tau_c^s(\mathbf{x}^d)} \right)^n \times \text{sgn}(m^s(\mathbf{x}^d) : \sigma'^{(n+1)}(\mathbf{x}^d)) \\ = \lambda^{(n)}(\mathbf{x}^d) + L^o : (\dot{E} + \tilde{d}^{(n+1)}(\mathbf{x}^d)) \end{aligned} \quad (2.3.3)$$

which can be efficiently solved by Newton–Raphson. The iteration is completed with the calculation of the new guess of the Lagrange multiplier field:

$$\lambda^{(n+1)}(\mathbf{x}^d) = \lambda^{(n)}(\mathbf{x}^d) + L^o : (\tilde{\varepsilon}^{(n+1)}(\mathbf{x}^d) - \tilde{d}^{(n+1)}(\mathbf{x}^d)). \quad (2.3.4)$$

Equations (2.3.3) and (2.3.4) in general guarantee the convergence of $\dot{\varepsilon}_{ij}$ and σ'_{ij} toward d_{ij} and λ_{ij} , respectively.

Upon convergence, the micromechanical fields (velocity, velocity gradient and stress fields) are assumed to be constant in a time interval Δt . The microstructure, e.g. the crystallographic orientation and the threshold stresses for slip, can be then updated for each Fourier point after each time increment. In particular, the new position of the Fourier points can be determined as $x_i = X_i + v_i \Delta t = X_i + (\dot{E}_{ij}x_j + \tilde{v}_i)\Delta t$. This update, however, would destroy the regularity of the Fourier grid after the very first time increment. Therefore, in what follows we use a simplified update scheme, neglecting the velocity fluctuation term: $x_i = X_i + \dot{E}_{ij}x_j \Delta t$. This results in an evolving regular Fourier grid, in which the distances between adjacent points change after each increment following the average stretching prescribed by the macroscopic deformation. The implications of this simplified updating scheme were discussed in [30] and, for the particular case of plane-strain of fcc materials, it was shown that only minor differences should be expected with respect to the more accurate morphologic evolution considering the velocity fluctuation term.

2.4. CPFEM model: theoretical framework

FEM models are based on the variational solution of the equilibrium of the forces using a weak form. Based on the principle of virtual work the basic equation reads

$$\int_V \sigma_{ij} \delta \varepsilon_{ij} \, dV = \int_V f_i^V \delta v_i \, dV + \int_S f_i^S \delta v_i \, dS, \quad (2.4.1)$$

where f_i^V is the body force, f_i^S is the surface traction, δv_i is the virtual velocity field, $\delta \dot{\epsilon}_{ij}$ is the virtual strain rate, $\dot{\epsilon}_{ij} = \frac{1}{2}(v_{i,j} + v_{j,i})$, V is the current volume and S is the surface bounding this volume.

The entire sample volume under consideration is discretized into elements, which is the reason why FEM is especially well suited for arbitrary geometries. The integrals in equation (2.4.1) can be split into integrals over the individual elements. That is each integral is split into a sum over N integrals, with N being the number of elements in the mesh. As the elements used in FEM have simple regular shapes, the individual element integrals can be easily evaluated numerically using, e.g., Gaussian quadrature.

In order to solve equation (2.4.1) the Cauchy stress σ_{ij} has to be calculated. In CPFEM models this is done via the generalized Hooke's law:

$$\sigma_{ij} = \frac{1}{J} F_{ik}^e S_{kl} F_{jl}^e \quad \text{and} \quad S_{ij} = C_{ijkl} \epsilon_{kl}^{G,*}, \quad (2.4.2)$$

where F_{ij}^e is the elastic part of deformation gradient F_{ij} , $J = \det(\mathbf{F}^e)$, S_{ij} is the second Piola–Kirchhoff stress, that is work conjugate to the elastic Green–Lagrange strain $\epsilon_{ij}^{G,*} = \frac{1}{2}(F_{ki}^e F_{kj}^e - \delta_{ij})$ and C_{ijkl} is the constant fourth-order elastic stiffness tensor. F_{ij}^e is calculated from the multiplicative decomposition of F_{ij}

$$F_{ij} = F_{ik}^e F_{kj}^p. \quad (2.4.3)$$

In order to do this one has to know the plastic deformation gradient F_{ij}^p , which evolves according to

$$\dot{F}_{ij}^p = v_{i,j}^p F_{ij}^p. \quad (2.4.4)$$

In the CPFEM the plastic velocity gradient $v_{i,j}^p$ is calculated from the slip rates $\dot{\gamma}^s$ on all active slip systems s :

$$v_{i,j}^p = \sum_{s=1}^{N_s} \dot{\gamma}^s m_i^s n_j^s. \quad (2.4.5)$$

where m_i^s is the slip direction and n_j^s the slip plane normal of slip system s .

2.5. CPFEM model: numerical algorithm

Crystal plasticity material models can be directly implemented into commercial FEM solvers in the form of user subroutines, e.g. HYPELA2 in MSC.Marc or UMAT/VUMAT in Abaqus. For implicit solvers the purpose of a material model is twofold: first, the stress σ_{ij} is calculated which is required to reach the final deformation gradient F_{ij} ; second, the Jacobian matrix, $J_{ijkl} = d\sigma_{ij}/d\epsilon_{jk}^G$, is calculated, where ϵ_{ij}^G is the total Green–Lagrange strain.

The stress calculation is implemented using a predictor–corrector scheme. Figure 1 visualizes the set-up of the clockwise loop of calculations to be performed. With an initial guess $v_{i,j}^{p,\text{guess}}$, the prediction $v_{i,j}^p$ is updated using a Newton–Raphson scheme until convergence is reached, i.e. the difference between $v_{i,j}^{p,\text{guess}}$ and $v_{i,j}^p$ falls below a prescribed threshold.

The Jacobian matrix is calculated numerically by perturbing the deformation gradient F_{ij} and determining the new resulting stress σ_{ij} .

2.6. Constitutive equation and hardening law

Both crystal plasticity models relate the shear rate on a system s to the stress acting on the system and the critical threshold stress (critical shear stress) of this system through a viscoplastic form

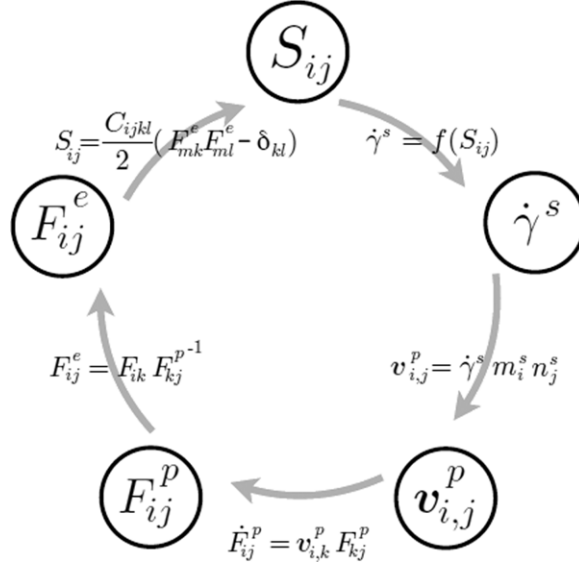


Figure 1. Clockwise loop of calculations during stress determination. Symbols: S_{ij} second Piola–Kirchhoff stress, $\dot{\gamma}^s$ shear rate, $v_{i,j}^p$ plastic velocity gradient, m_i^s slip direction, n_j^s slip plane normal, F_{ij}^p plastic deformation gradient, F_{ij}^e elastic deformation gradient, C_{ijkl} elasticity tensor, δ_{ij} Kronecker delta.

according to

$$\dot{\gamma}^s = \dot{\gamma}_0 \left| \frac{\tau^s}{\tau_c^s} \right|^{1/m} \text{sgn}(\tau^s), \quad (2.6.1)$$

where τ^s is the resolved shear stress on slip system s and m ($m = 0.1$) is the rate-sensitivity parameter, which is the reciprocal of n in equation (2.2.1).

For describing the evolution of the critical shear stress as a function of the accumulated preceding shears, both models use the hardening law based on the work of Brown *et al* [37].

$$\dot{\tau}_c^s = \sum_{s'} q^{ss'} h^{s'} |\dot{\gamma}^{s'}| \quad \text{and} \quad h^{s'} = h_0 \left(1 - \frac{\tau_c^{s'}}{\tau_s} \right)^a, \quad (2.6.2)$$

where $q^{ss'}$ ($q^{ss'} \equiv 1.0$) is the ratio matrix of latent hardening rate to self-hardening rate, τ_s ($\tau_s = 90$ MPa) is the saturation shear stress, h_0 ($h_0 = 400$ MPa) and a ($a = 2.25$) are constant parameters. The stress–strain curves calculated by both models are shown in figure 2.

3. Statistical texture evolution predicted by CPFFT and CPFEM: results and discussion

3.1. Starting texture and orientation mapping

The simulations started with a typical recrystallization texture of FCC metals containing a Cube orientation ($0^\circ, 0^\circ, 0^\circ$)⁴ with scatter about the rolling direction (RD) from Cube toward Goss ($0^\circ, 45^\circ, 0^\circ$), figure 3 left. The corresponding orientation distribution function (ODF) is constructed from 1024 equally weighted orientations [38]. The same spatial configuration of 1024 grains (figure 3 right) is used as starting configuration for both, the CPFEM and CPFFT simulations.

⁴ Bunge–Euler notation.

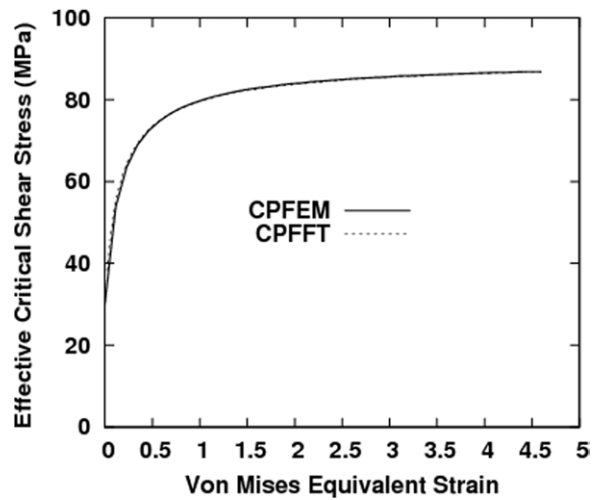


Figure 2. Evolution of the critical shear stress as a function of deformation in the two models.

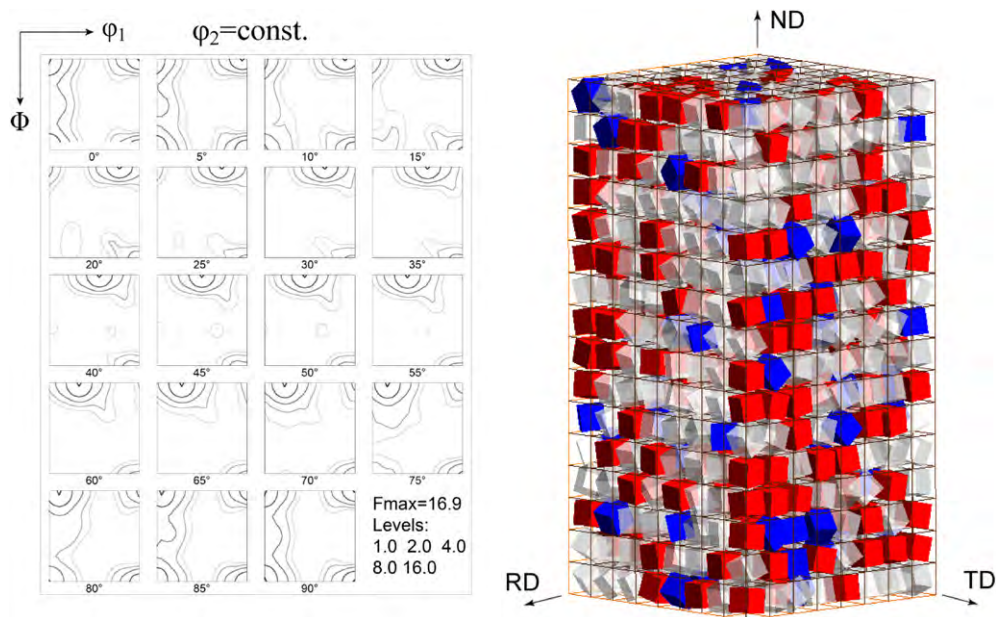


Figure 3. Initial texture and orientation mapping for the CPFFT and CPFEM simulations. The starting texture contains a Cube orientation ($0^\circ, 0^\circ, 0^\circ$) with some scatter about the RD from the Cube toward the Goss ($0^\circ, 45^\circ, 0^\circ$). Small cube symbols represent the crystallographic orientations. Red and blue colors indicate orientations within a 15° misorientation to Cube and Goss, respectively. The intermediate orientations are transparent.

The figure shows the unit cell and the sample reference frame, and the cube symbols represent the crystallographic orientations, which have been rotated about the sample axes accordingly. Red and blue colors indicate orientations that are within 15° misorientation to Cube and Goss, respectively. The other intermediate orientations are transparent. For the texture simulations the orientations are mapped onto the integration points for the CPFEM model and on the

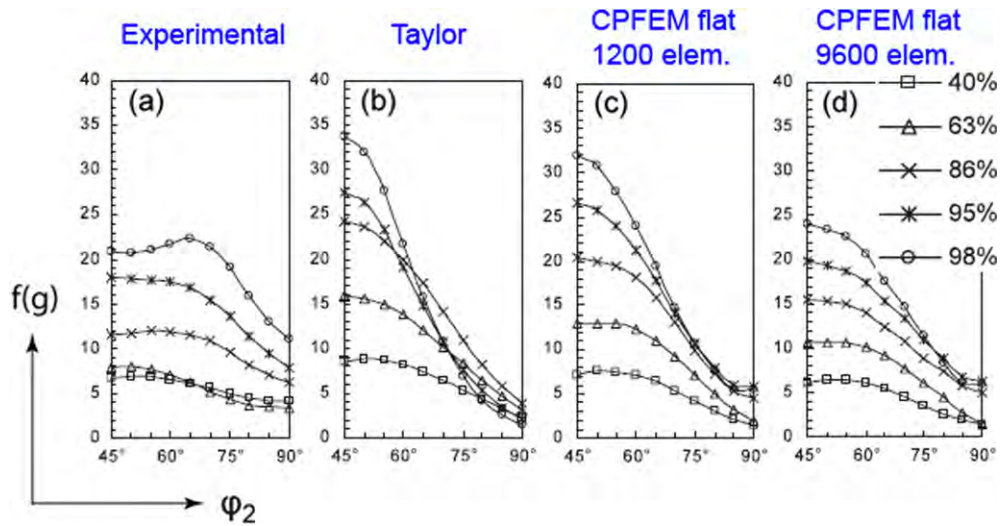


Figure 4. Rolling texture β -fiber, after Li *et al* [39]: (a) experimental results of aluminum alloys AA1200, (b) Taylor model, (c) CPFEM with flat surface boundary conditions (1200 elements, 1200 grains), (d) CPFEM with flat surface boundary conditions (9600 elements, 1200 grains).

Fourier points for the CPFEM model. The sample size and geometry ($8 \times 8 \times 16$) were chosen to approximate previous CPFEM texture simulations in the literature [39] which used 1200 grains. Also, the unit cell size and discretization was made compatible with the FFT algorithm. In the present CPFEM implementation, the FFT is performed by adopting the algorithm from [40], which requires that the number of Fourier points to be a power of two along each dimension.

3.2. Analysis of the predicted texture fibers and strain distributions

In what follows, the ODFs are calculated from the discrete orientations of the 1024-grain ensemble using spherical harmonics with a 7° Gaussian smoothing. This method was also employed in previous works used for comparison [5, 39, 41]. First, we compared the β -fiber predictions of our CPFEM calculations (periodic boundary conditions) with earlier ones (flat surface boundary conditions) by Li *et al* [39]. The overall CPFEM texture simulations with all surfaces flat, figure 4(c), yield predictions close to those of the Taylor model, figure 4(b), while the use of periodic boundary conditions, figure 5(a), allows the crystals more freedom during deformation and thus the results show more deviations to those of the Taylor model.

For comparison purposes, the CPFEM and CPFEM textures are presented in terms of β -fiber plots, which reveal an increase in intensity of the stable rolling orientations (copper ($90^\circ, 35^\circ, 45^\circ$), S ($59^\circ, 37^\circ, 63^\circ$) and brass ($35^\circ, 45^\circ, 0^\circ$)), figures 5(a)–(c); and Cube-RD fiber plots, figures 6(a)–(c), which show a decrease in the density of the starting orientations, namely a drastic decay of the Cube orientation and the metastability of the Goss orientation. In the CPFEM simulations the originally Cube oriented grains show higher rotation rates away from their initial orientation, but further on, the reorientation of these grains toward the stable plane-strain orientations (copper, S, brass) becomes slower (figures 5(b) and 6(b)) than in the corresponding CPFEM simulations (figures 5(a) and 6(a)). The CPFEM textures with different resolutions are nearly the same, figures 5(b), (c) and 6(b), (c), while this is not the case with CPFEM, figures 4(c) and (d). As the number of elements increased from 1 to 8

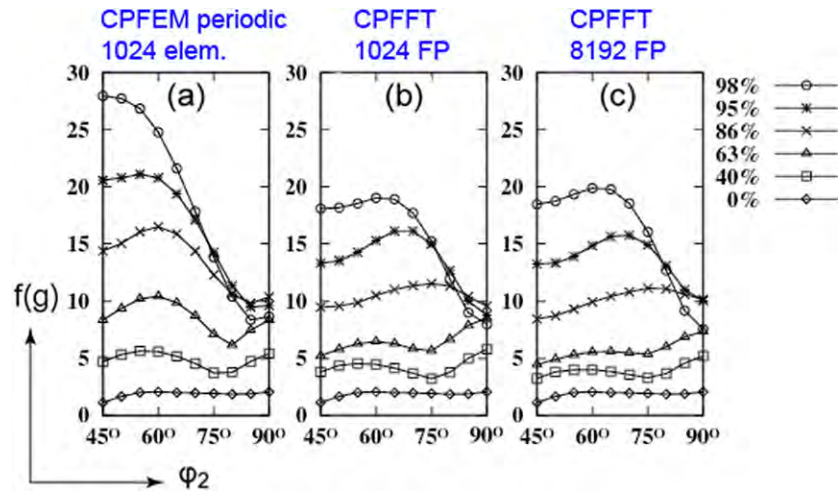


Figure 5. Rolling texture β -fiber, this work: (a) CPFEM with periodic boundary conditions (1024 elements, 1024 grains), (b) CPFFT (1024 Fourier points, 1024 grains), (c) CPFFT (8192 Fourier points, 1024 grains).

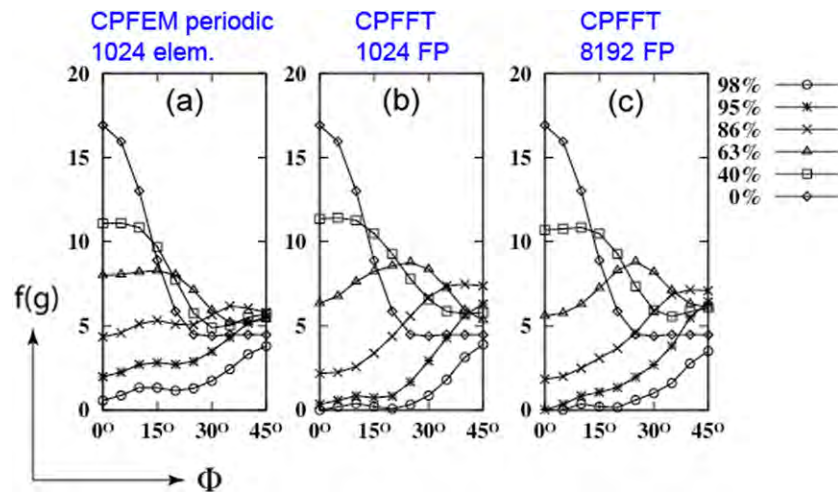


Figure 6. Rolling texture Cube-RD fiber: (a) CPFEM with periodic boundary conditions (1024 elements, 1024 grains), (b) CPFFT (1024 Fourier points, 1024 grains), (c) CPFFT (8192 Fourier points, 1024 grains).

per grain, a substantial drop in intensity of the copper component is observed, which makes the results deviate from the Taylor model calculations, figure 4(b), closer to the experimental results, figure 4(a). For the CPFFT simulation, strikingly, even at low resolution, the calculated β -fibers (figure 6(b)) match well the experimental results (figure 4(a)).

The strain distributions of the CPFEM and CPFFT simulations are given in figure 7. All the strain components have broader fluctuation ranges in the CPFFT simulations than in the CPFEM simulation. In the CPFFT case, with increasing resolution (1 Fourier point to 8 Fourier points per grain), the strain distributions become smoother especially for strain component

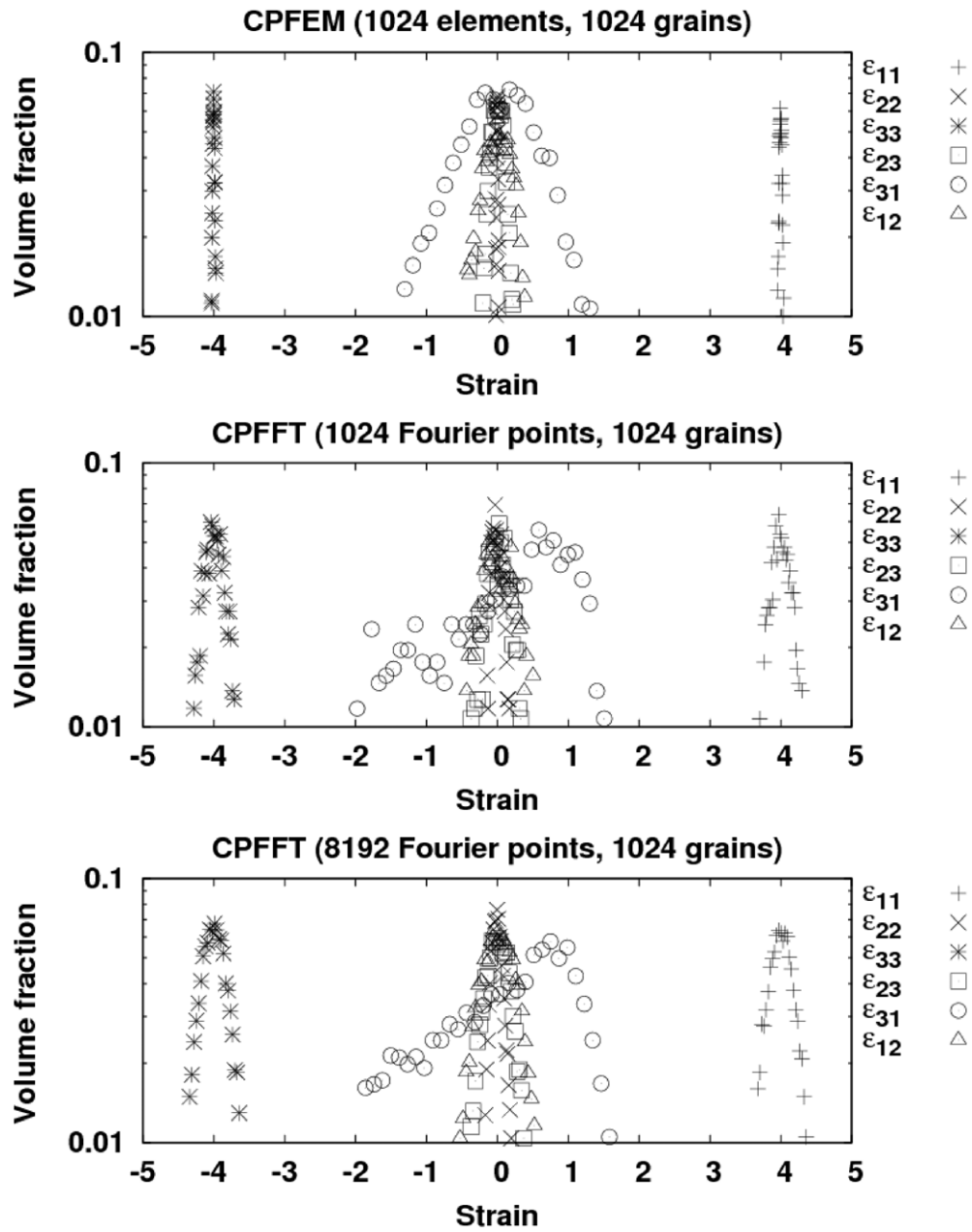


Figure 7. Strain distributions after plane-strain compression at 98% thickness reduction: CPFEM with periodic boundary conditions (1024 elements, 1024 grains), CPFPT (1024 Fourier points, 1024 grains), CPFPT (8192 Fourier points, 1024 grains).

ϵ_{31} , but the distribution widths for all strain components hardly change. With the same initial configuration and boundary conditions, using the same crystal plasticity constitutive equation and hardening law, the CPFEM and CPFPT simulations give different combinations of orientation and strain distributions.

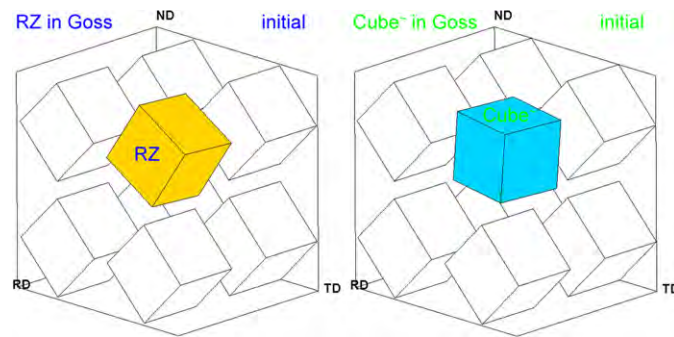


Figure 8. Initial configurations of the bicrystals.

The above comparison between the predictions of both models leads to the following questions:

- What causes the different textures and strain distributions as predicted by the two models?
- Why increasing the resolution has almost no effect on the textures and strain distributions predicted with CPFEM, but strongly affects the CPFEM results?

To start addressing these issues, let us first note that texture evolution is closely connected to strain distribution, in such a way that a sharp rolling texture with the copper component dominating the β -fiber corresponds to a strain distribution that does not deviate much from the macroscopic strain state. On the other hand, the local strain deviations from the macroscopic state have to be balanced by the surrounding material. In other words, how much the local strain can deviate from the average depends on how large are the strain gradients that can be accommodated. Thus, from figure 7, it can be concluded that, on average, the strain gradients are smaller and more sensitive to mesh refinement in the CPFEM simulations compared with the CPFEM case.

With these in mind, next section presents a study of the strain gradients predicted by CPFEM and CPFEM in the case of bicrystals, including the analysis of the role played, respectively, by the FE mesh and the Fourier grid refinements.

4. Strain gradients predicted by CPFEM and CPFEM for bicrystals: results and discussion

To investigate the difference between the CPFEM and CPFEM models in solving strain gradients, we simulate plane-strain compression of two bicrystals at 90% thickness reduction. The two grains of the first bicrystal are assigned with the RZ orientation ($32^\circ, 85^\circ, 85^\circ$) [42] and the Goss orientation ($0^\circ, 45^\circ, 0^\circ$). In the periodic sense, the RZ grain is surrounded by the Goss grain, figure 8(left). The second bicrystal is different from the first one in the way that the center grain is assigned with an initial orientation that is the Cube orientation ($0^\circ, 0^\circ, 0^\circ$) rotated 5° about ND and 5° about RD, which will be referred to as 'Cube~' ($5^\circ, 5^\circ, 0^\circ$) from now on, figure 8(right). The introduction of a RZ grain or a Cube~ grain surrounded by a Goss matrix gives relative high and low strain gradients across the bicrystals, respectively. The simulations were run with different resolutions: 1, 8, 64, 512 Fourier points or finite elements for the RZ and Cube~ grains and $1 \times 7, 8 \times 7, 64 \times 7, 512 \times 7$ Fourier points or finite elements for the surrounding Goss grain.

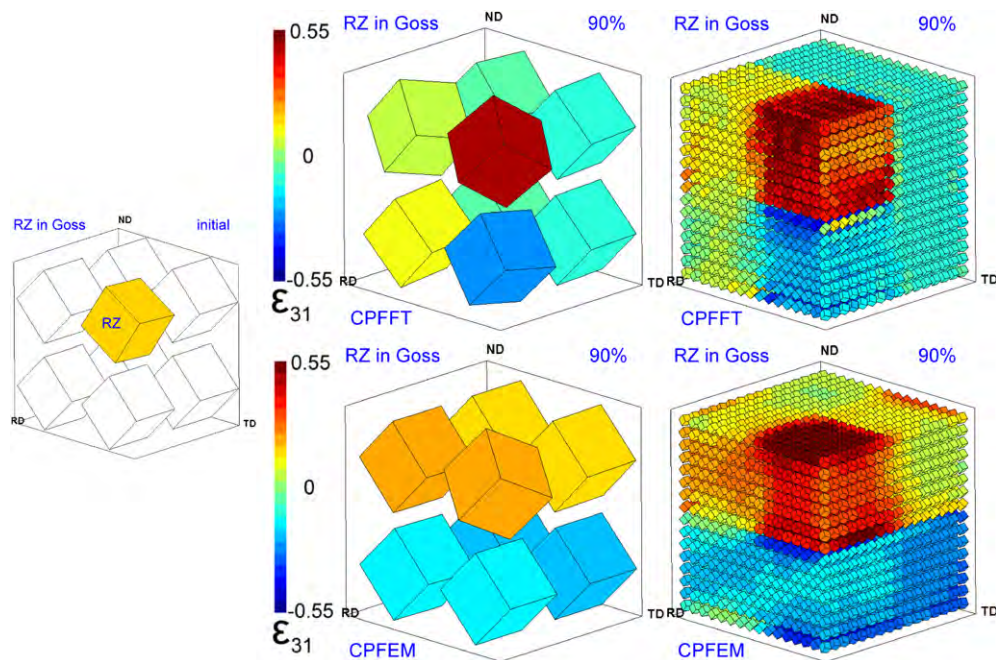


Figure 9. Final crystallographic orientations and strain states on the material points after plane-strain compression of a bicrystal (RZ in Goss) at 90% thickness reduction. The cube symbols are rotated according to the final orientations, and colored according to the values of strain component ϵ_{31} . The results correspond to the simulations run at the lowest resolution (1 Fourier point or element in the RZ grain and 1×7 Fourier points or elements in the Goss grain) (left) and at the highest resolution (512 Fourier points or elements in the RZ grain and 512×7 Fourier points or elements in the Goss grain) (right).

The results of these bicrystal simulations are presented in the following way:

- The final local crystallographic orientations are represented by the rotations of the small cubes, and the values of local shear strain component ϵ_{31} are represented by the color of those cubes. (In this paper RD, TD and ND of the sample are identified with directions 1, 2 and 3, respectively.) Using this convention the results of the simulations run with the lowest and highest resolutions are presented in figure 9 for the ‘RZ-in-Goss’ bicrystal, and in figure 11 for the ‘Cube~in-Goss’ case.
- The grain averages of ϵ_{31} are plotted with the consideration of the different volume fractions of the crystals (for the RZ and Cube~ grains: $\epsilon_{31} \times 1$, for the Goss grain: $\epsilon_{31} \times 7$). The strain plots obtained with different resolutions are presented in figure 10 for the RZ-in-Goss, and in figure 12 for Cube~in-Goss cases.

The differences between these CPFEM and CPFEM results reveal that the two methods lead to different combinations of grain rotations and strain fields. Specifically, the results of these bicrystal simulations show that

- For the RZ-in-Goss bicrystal, figure 9, CPFEM gives higher strain gradients and more diverse rotations than the CPFEM model at low resolution (1 Fourier point or element in the RZ grain, 1×7 Fourier points or elements in the Goss grain). At higher resolution, the bicrystal starts to split up into fragments, becoming a polycrystal. The strain gradients and grain rotation diversity calculated by both methods are comparable at high resolution

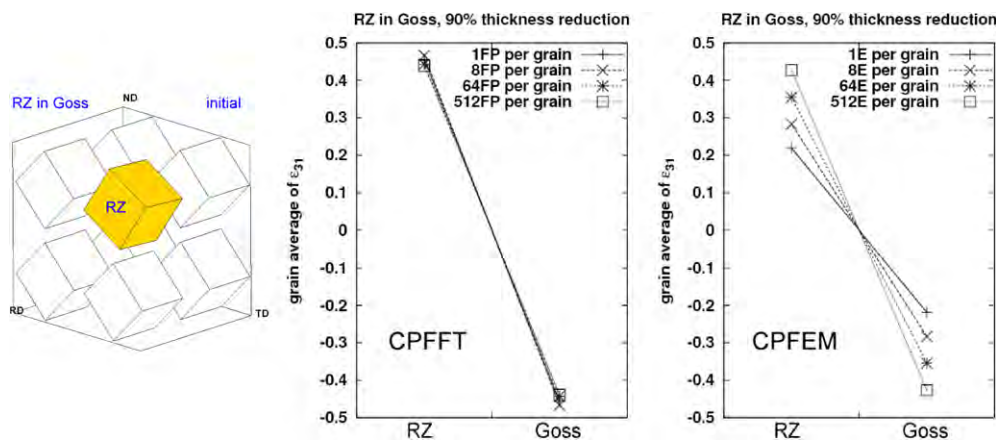


Figure 10. Plane-strain compression of a bicrystal (RZ in Goss) at 90% thickness reduction. The grain averages of strain component ϵ_{31} are plotted considering the different volume fractions of the crystals (for the RZ grain $\epsilon_{31} \times 1$, for the Goss grain $\epsilon_{31} \times 7$) for simulations run at different resolutions: 1, 8, 64, 512 Fourier points or elements in the RZ grain and 1×7 , 8×7 , 64×7 , 512×7 Fourier points or elements in the Goss grain.

(512 Fourier points or elements in the RZ grain, 512×7 Fourier points or elements in the Goss grain).

- For the Cube \sim -in-Goss case, figure 11, at low resolution, comparable strain gradients and grain rotations are obtained with CPFFT and CPFEM. As resolution increases, higher strain gradients and more diverse grain rotations are observed in the simulation results of both models. The differences in strain gradients between the CPFFT and CPFEM results become pronounced at high resolution.
- On average, the strain gradients across the bicrystals continuously rise with increasing resolution in CPFEM simulations, but hardly change in the CPFFT simulations, figures 10 and 12.

The CPFFT model calculates certain strain gradients at low resolution. The average strains can be captured even at the lower end of the resolution scale. This well explains why there is almost no resolution effect on the CPFFT simulation of the 1024 grain polycrystal in section 3. The CPFEM model gives the lowest strain gradient at low resolution. As resolution increases, the CPFEM simulations continuously approach higher strain gradients, and the calculated average grain strains grow accordingly. This explains why refined resolution strongly affects the CPFEM results.

We want to point out here that there is no real meaning in discussing the convergence of these bicrystal results as resolution increases, because, at large deformations, the crystals tend to split up, such that the initial bicrystal becomes different polycrystals in the simulations conducted at different resolutions.

5. Micro-texture predictions using the CPFFT model: results and discussion

One of the advantages of full-field models, such as CPFEM and CPFFT, over grain-cluster models is that they take into account the spatial configuration of the polycrystals and the grain interactions in the whole RVE [5, 7, 8, 43, 44]. This enables full-field models to predict intragranular reorientations during deformation. Although the related grain-cluster models

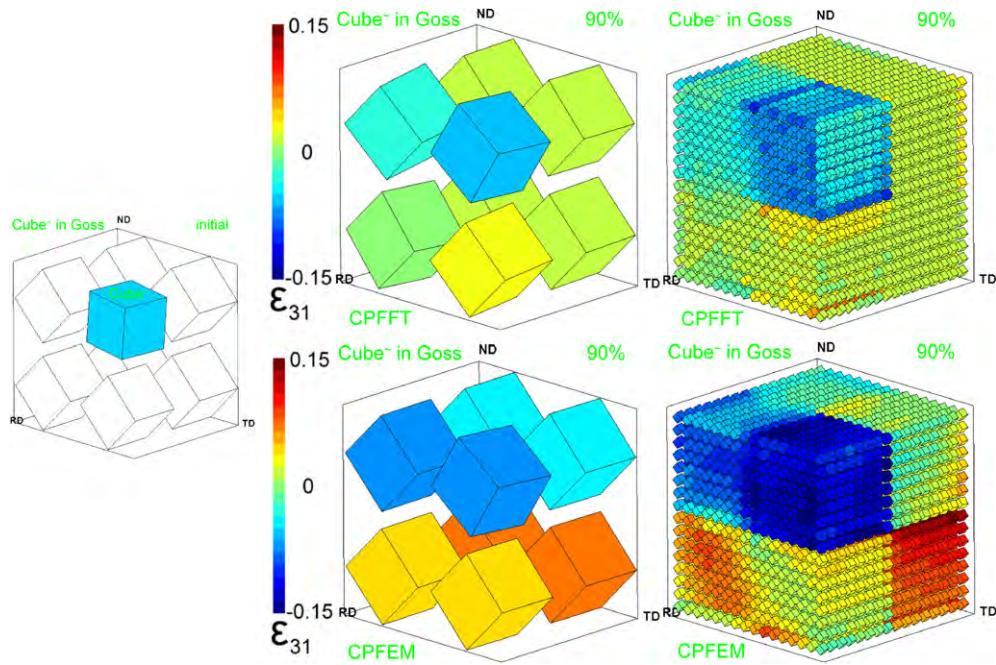


Figure 11. Final crystallographic orientations and strain states on the material points after plane-strain compression of a bicrystal (Cube[~] in Goss) at 90% thickness reduction. The cube symbols are rotated according to the final orientations, and colored according to the values of strain component ϵ_{31} . The results presented here are from the simulations run at the lowest resolution (1 Fourier point or element in the Cube[~] grain and 1×7 Fourier points or elements in the Goss grain) (left) and at the highest resolution (512 Fourier points or elements in the Cube[~] grain and 512×7 Fourier points or elements in the Goss grain) (right).

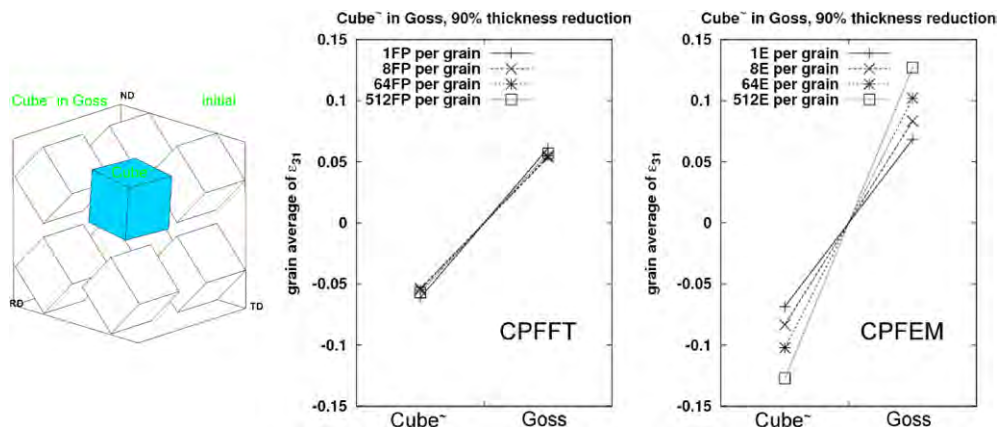


Figure 12. Plane-strain compression of a bicrystal (Cube[~] in Goss) at 90% thickness reduction. The grain averages of strain component ϵ_{31} are plotted considering the different volume fractions of the crystals (for the Cube[~] grain $\epsilon_{31} \times 1$, for the Goss grain $\epsilon_{31} \times 7$) for simulations run at different resolutions: 1, 8, 64, 512 Fourier points or elements in the Cube[~] grain and 1×7 , 8×7 , 64×7 , 512×7 Fourier points or elements in the Goss grain.

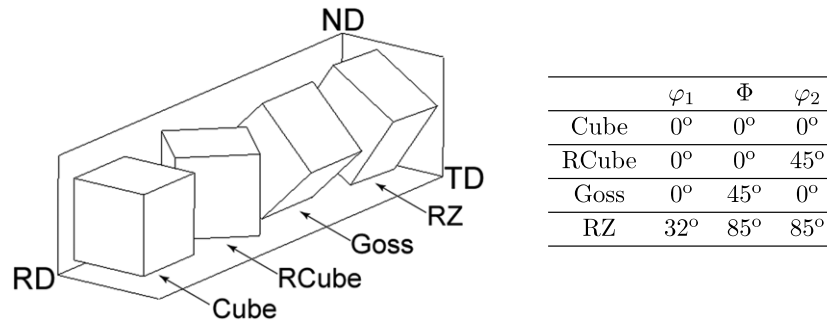


Figure 13. Crystallographic orientations chosen to construct a 64-grain RVE.

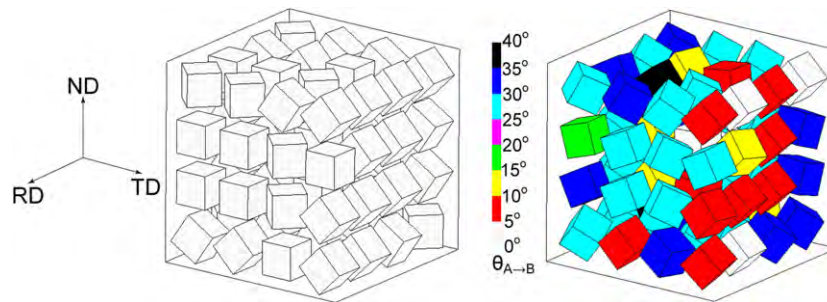


Figure 14. Crystallographic orientations of the 64-grain RVE before deformation (left) and after plane-strain compression at 90% thickness reduction (right) obtained in the case of one Fourier point per grain simulation. $\theta_{A \rightarrow B}$ is the misorientation between the starting orientation (A) and final orientation (B) for a single grain.

(e.g. GIA, ALAMEL) have been proven to be highly efficient for texture simulations, they have been less successful when applied at the single-crystal scale, as they do not account for the near- and far-field spatial arrangement of the crystals in the sample and the corresponding strain relaxations inside a wider cluster. When a single crystal is composed of more than one numerical unit, full-field models are able to simulate the orientation split-up inside one single grain [33, 42, 43, 45]. In the CPFEM model used in this work such split-up is due to grain interactions [33] while for the CPFEM model both intrinsic (grain interactions) and extrinsic mechanical conditions such as friction and complex externally imposed strain paths can enter the simulation, which in turn can lead to the fragmentation of originally homogeneously oriented grains [42, 45].

In this section we present a theoretical study on micro-texture evolution of a 64-grain RVE during plane-strain compression using the CPFEM approach. The sample is build up from four orientations (figure 13), arranged in random order (figure 14, left). The Cube, rotated Cube, Goss and RZ orientations have been chosen to study the initial orientation dependence and crystal neighbor influence of in-grain orientation split-up as analyzed earlier using CPFEM simulations in [42]. The choice of these four texture components is related to their different orientation stabilities under plane-strain loading [18, 42, 46, 47].

In previous CPFEM simulations on orientation stability, only single crystals and bicrystals have been investigated. In a 64-grain aggregate more grain-scale diversity is created by the grain neighborhood. The 50% thickness reduction used in the former study is extended to 90% in the current one. This is more revealing of the final stable texture components. The

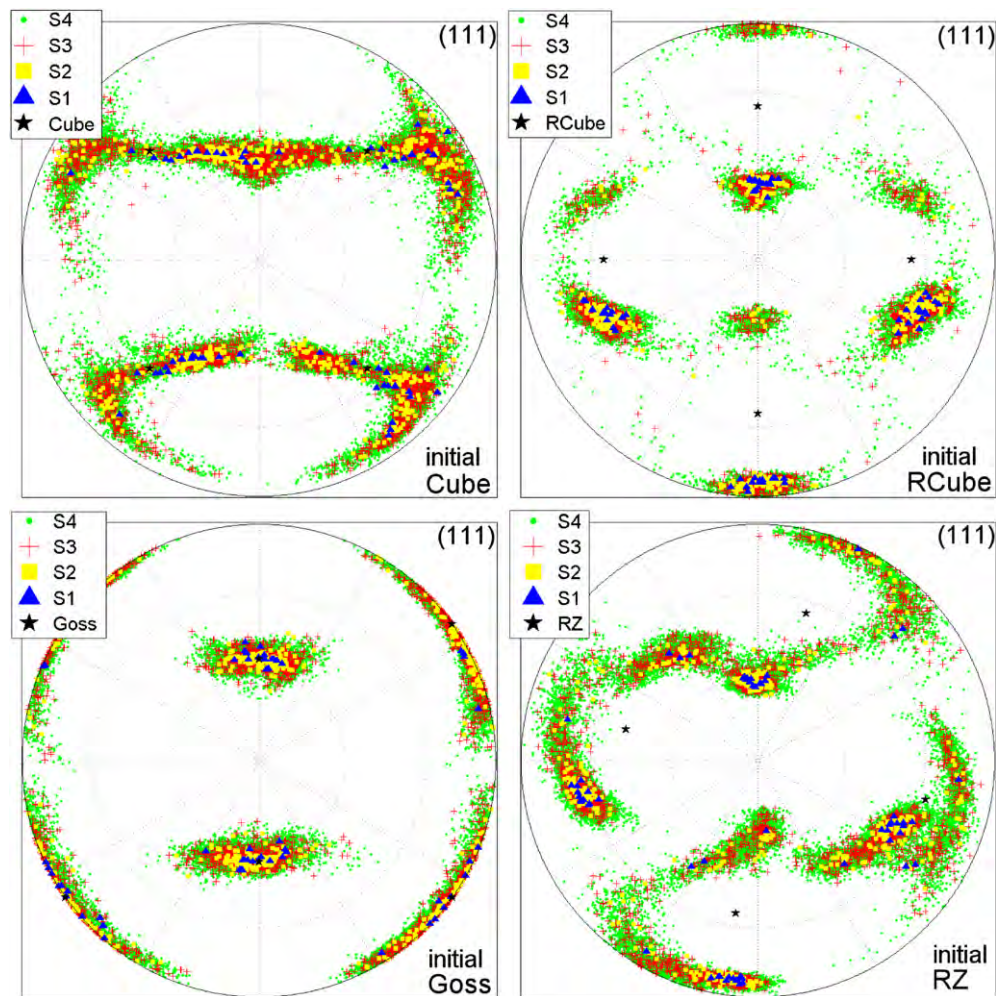


Figure 15. In-grain texture evolution inside the 64-grain RVE presented in the form of $\{111\}$ pole figures. The split-up and resulting reorientation distribution is shown individually for the four selected initial texture components Cube, rotated Cube, Goss and RZ; CPFPT; plane-strain compression; thickness reduction 90%: S1 (1 Fourier point per grain simulation), S2 (8 Fourier points per grain simulation), S3 (64 Fourier points per grain simulation), S4 (512 Fourier points per grain simulation). The grains that have identical initial orientation are put into the same $\{111\}$ pole figure, and the black stars mark the starting orientations.

simulations were run at four resolution levels, namely 1; $8(2 \times 2 \times 2)$; $64(4 \times 4 \times 4)$ and $512(8 \times 8 \times 8)$ Fourier points per grain. The results of all simulations are shown in figure 15. Grains with identical initial orientation are presented in the same $\{111\}$ pole figure. The black stars mark the starting orientations. The other markers are used to indicate the simulation results obtained at the different resolutions.

These results allow us to make a number of observations.

For the simulation with only one Fourier point per grain (marked by blue triangles in figure 15) the final orientation spread is due to the fact that the initially identically oriented grains have different neighbors in this 64-grain RVE. Depending on the initial orientation and grain neighborhood, the grain rotations can, hence, vary substantially. The results obtained for

Table 1. Misorientation ($\theta_{A \rightarrow B}$) between the starting orientation (A) and final orientation (B): statistics of 1 Fourier point per grain simulation (figure 14, right).

	$\max(\theta_{A \rightarrow B})$	$\min(\theta_{A \rightarrow B})$	$\text{mean}(\theta_{A \rightarrow B})$	$\Sigma(\theta_{A \rightarrow B}) (N = 16)$
Cube grains	38.4°	3.6°	21.0°	11.1°
RCube grains	33.3°	26.7°	29.0°	1.8°
Goss grains	22.9°	0.9°	8.8°	5.1°
RZ grains	34.5°	28.0°	30.0°	1.7°

Table 2. Misorientation ($\theta_{B \rightarrow C}$) between the final orientation (B) and the ideal texture component (C): statistics of 512 Fourier points per grain simulation; thickness reduction 90%.

	$\max(\theta_{B \rightarrow C})$	$\min(\theta_{B \rightarrow C})$	$\text{mean}(\theta_{B \rightarrow C})$	$\Sigma(\theta_{B \rightarrow C})(N = 16 \times 512)$
Cube grains to Goss(C)	60.0°	4.0°	22.9°	7.6°
RCube grains to Copper(C)	55.0°	0.4°	8.5°	4.6°
Goss grains to Goss(C)	43.6°	0.2°	10.2°	6.9°
RZ grains to S(C)	46.1°	0.7°	15.6°	8.2°

the calculation with one Fourier point per grain are additionally presented in figure 14(right), to make a direct comparison with the starting orientations in figure 14(left), using the same method by sample-axis rotations and color-coded misorientations as in figure 3(right).

When divided by the macroscopic von Mises strain (2.645, at 90% thickness reduction), the misorientation $\theta_{A \rightarrow B}$ (between the starting and final orientations) can be used as a measure of the grain rotation rate, and its standard deviation $\Sigma(\theta_{A \rightarrow B})$ can be used to indicate the neighbor sensitivity of the rotation rate.

$$\Sigma(\theta) = \sqrt{\frac{1}{N} \sum_{i=1}^N [\theta - \text{mean}(\theta)]^2}.$$

The maximum, minimum, mean, and standard deviation of the rotation angles for initially differently oriented grains are listed in table 1. On average, the rotation rates $\theta_{A \rightarrow B}$ follow the sequence $\theta_{A \rightarrow B}^{\text{RZ}} > \theta_{A \rightarrow B}^{\text{RCube}} > \theta_{A \rightarrow B}^{\text{Cube}} > \theta_{A \rightarrow B}^{\text{Goss}}$. Besides this global tendency, the rotation rates of Cube and Goss oriented grains are more sensitive to the influence of neighbor grains than those of RCube and RZ grains, following the sequence $\Sigma(\theta_{A \rightarrow B}^{\text{Cube}}) > \Sigma(\theta_{A \rightarrow B}^{\text{Goss}}) > \Sigma(\theta_{A \rightarrow B}^{\text{RCube}}) \simeq \Sigma(\theta_{A \rightarrow B}^{\text{RZ}})$.

For the simulations with more than one Fourier point in each grain, the intragranular misorientations are stimulated by the grain interactions. As it is shown in figure 15, at 90% thickness reduction, RCube oriented grains rotate into the copper orientation, RZ oriented grains rotate toward the S component, Cube grains rotate into the Goss orientation and Goss grains only rotate slightly. Based on these results we next calculated the misorientation ($\theta_{B \rightarrow C}$) between the simulated final orientations (B) and the closest ideal texture component (C) for the whole data set obtained from a simulation with 512 Fourier points per grain. From these misorientations we derived the maximum, minimum, mean and standard deviation as listed in table 2. The RZ and Cube grains show stronger intragranular orientation subdivisions than the Goss and RCube grains, as $\Sigma(\theta_{B \rightarrow C}^{\text{RZ}}) > \Sigma(\theta_{B \rightarrow C}^{\text{Cube}}) > \Sigma(\theta_{B \rightarrow C}^{\text{Goss}}) > \Sigma(\theta_{B \rightarrow C}^{\text{RCube}})$. We pick four initially differently oriented grains out of the 64-grain cluster from the 512 Fourier point per grain simulation. The final orientations of the Fourier points inside the

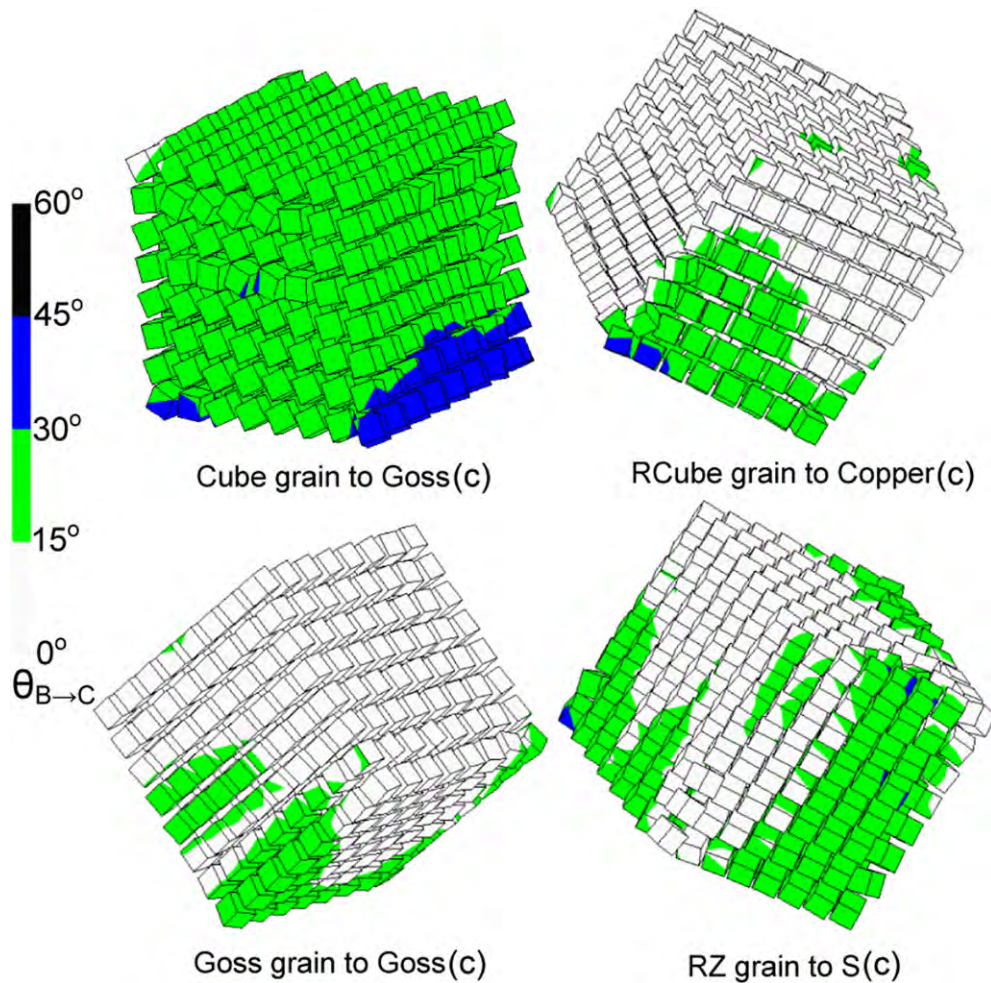


Figure 16. Example of in-grain orientation split-up in four grains inside the 64-grain RVE (512 Fourier points per grain calculation). $\theta_{B \rightarrow C}$ is the misorientation between the final orientation (B) and the ideal texture component (C). The reference ideal texture components (C) for initially differently oriented grains are given below the figures.

four grains are presented in figure 16 in terms of the small cube symbols. The material units (Fourier points) inside the initially Cube and RZ oriented crystals create upon loading more diverse in-grain rotation fields, than those inside the Goss grain. The RCube grains tend to split into two Copper components (equivalent under orthotropic sample symmetry). In figure 16, the misorientations between the final orientations and ideal texture components are color-mapped.

6. Conclusions

We simulated the statistical texture evolution of a FCC metal (plane-strain loading), and investigated the strain gradients predicted in bicrystals under the same deformation mode, with the full-field crystal plasticity Fast Fourier Transform and Finite Element models. Additionally

we conducted a grain-scale orientation fragmentation analysis using the FFT approach. The main conclusions are the following:

- Concerning the statistical texture evolution simulations of the 1024-grain ensemble:
 - In the CPFFT simulations Cube oriented grains show higher rotation rates away from their starting orientation and slower rotations at the later deformation stages toward stable plane-strain orientations (copper, S, brass) than in the CPFEM simulations.
 - With the same initial configuration and boundary conditions, using the same crystal plasticity constitutive equation and hardening law, the CPFEM and CPFFT simulations give different combinations of orientation and strain distributions.
- Concerning the strain gradient predictions in bicrystals:
 - The CPFFT model predicts certain strain gradients at low resolution. The average strains in the grains can be captured even at the lower end of the resolution scale. This explains that why there is nearly no resolution effect on the CPFFT simulation of the 1024 grain polycrystal.
 - The CPFEM model gives the lowest strain gradient at low resolution. As the resolution increases, the CPFEM simulations continuously approach higher strain gradients, and the calculated average strains in the grains grow accordingly. Thus, resolution strongly affects the CPFEM results.
- General comments on the texture predictions of the CPFFT and CPFEM models for engineering applications:
 - For the statistical texture evolution simulation with a sample size larger than one thousand grains like the ones in section 3, the orientation and strain distributions can be obtained at relatively low resolutions using the CPFFT model. For the CPFEM model, this would depend on the initial orientations inside the sample, which means higher resolution is needed when the initial orientation distribution tends to introduce higher strain gradients.
- Concerning micro-texture predictions of the 64-grain aggregate:
 - Plane-strain compression of the 64-grain RVE at 90% thickness reduction revealed that the RCube grains rotate toward the copper orientation; the RZ grains rotate close to the S orientation; the Cube grains rotate toward the Goss orientation; and the Goss grains only slightly rotate away from their initial orientation.
 - The rotation rates $\dot{\theta}_{A \rightarrow B}$ of grains with different initial orientations follow the following sequence: $\dot{\theta}_{A \rightarrow B}^{\text{RZ}} > \dot{\theta}_{A \rightarrow B}^{\text{RCube}} > \dot{\theta}_{A \rightarrow B}^{\text{Cube}} > \dot{\theta}_{A \rightarrow B}^{\text{Goss}}$.
 - The rotation rates of the Cube and Goss grains are more sensitive to the grain neighborhood than those of the RCube and RZ grains. The grain neighborhood dependence follows the sequence: $\Sigma(\dot{\theta}_{A \rightarrow B}^{\text{Cube}}) > \Sigma(\dot{\theta}_{A \rightarrow B}^{\text{Goss}}) > \Sigma(\dot{\theta}_{A \rightarrow B}^{\text{RCube}}) \simeq \Sigma(\dot{\theta}_{A \rightarrow B}^{\text{RZ}})$.
 - The Cube and RZ grains reveal larger in-grain rotation gradients after deformation than the Goss grains. The rotated Cube grains split into two equivalent copper components.

References

- [1] Taylor G I 1938 *J. Inst. Metals* **62** 307–24
- [2] Honeff H and Mecking M 1978 *Proc. ICOTOM 5 (Aachen, Germany)* ed G Gottstein and K Lücke (Berlin: Springer) p 265
- [3] Van Houtte P 1981 *Proc. ICOTOM 6 (Tokyo, Japan)* ed S Nagashima (Japan: ISIJ) p 428
- [4] Van Houtte P, Delannay L and Samajdar I 1999 *Textures Microstruct.* **31** 109

- [5] Van Houtte P, Li S, Seefeldt M and Delannay L 2005 *Int. J. Plast.* **21** 589
- [6] Evers L P, Parks D M, Brekelmans W A M and Geers M G D 2002 *J. Mech. Phys. Solids* **50** 2403
- [7] Crumbach M, Pomana G, Wagner P and Gottstein G 2001 *Proc. 1st Joint Int. Conf. on Recrystallization and Grain Growth (Aachen, Germany)* ed G Gottstein and D A Molodov (Berlin: Springer) p 1053
- [8] Schäfer C, Song J and Gottstein G 2009 *Acta Mater.* **57** 1026
- [9] Eshelby J D 1957 *Proc. R. Soc. A* **241** 376
- [10] Hill R 1966 *J. Mech. Phys. Solids* **14** 95
- [11] Molinari A, Canova G R and Ahzi S 1987 *Acta Metall.* **35** 2983
- [12] Lebensohn R A and Tomé C N 1993 *Acta Metall. Mater.* **41** 2611
- [13] Peirce D, Asaro R J and Needleman A 1982 *Acta Metall. Mater.* **30** 1087
- [14] Harren S V, Déve H and Asaro R J 1988 *Acta Metall. Mater.* **36** 2435
- [15] Harren S V and Asaro R J 1989 *J. Mech. Phys. Solids* **37** 191
- [16] Becker R 1991 *Acta Metall. Mater.* **39** 1211
- [17] Becker R, Butler J F, Hu H and Lalli L A 1991 *Metall. Trans. A* **22** 45
- [18] Beaudoain A J, Mecking H and Kocks U F 1996 *Philos. Mag. A* **73** 1503
- [19] Sarma G B and Dawson P R 1996 *Int. J. Plast.* **12** 1023
- [20] Sarma G B, Radhakrishnan B and Zacharia T 1998 *Comput. Mater. Sci.* **12** 105
- [21] Mika D P and Dawson P R 1998 *Mater. Sci. Eng. A* **257** 62
- [22] Bachu V and Kalidindi S R 1998 *Mater. Sci. Eng. A* **257** 108
- [23] Sachtleber M, Zhao Z and Raabe D 2002 *Mater. Sci. Eng. A* **336** 81
- [24] Zhao Z, Kuchnicki S, Radovitzky R and Cuitiño A 2007 *Acta Mater.* **55** 2361
- [25] Zhao Z, Ramesh M, Raabe D, Cuitiño A and Radovitzky R 2008 *Int. J. Plast.* **24** 2278
- [26] Moulinec H and Suquet P 1998 *Comput. Methods Appl. Mech. Eng.* **157** 69
- [27] Michel J C, Moulinec H and Suquet P 2000 *Comput. Modeling Eng. Sci.* **1** 79
- [28] Lebensohn R A 2001 *Acta Mater.* **49** 2723
- [29] Mura T 1987 *Micromechanics of Defects in Solid* 2nd edn (Dordrecht: Martinus Nijhoff)
- [30] Prakash A and Lebensohn R A 2009 *Modeling Simul. Mater. Sci. Eng.* **17** 064010
- [31] Zeller R and Dederichs P H 1973 *Phys. Status Solidi b* **55** 831
- [32] Lebensohn R A, Liu Y and Ponte Castañeda P 2004 *Acta Mater.* **52** 5347
- [33] Lebensohn R A, Brenner R, Castelnau O and Rollett A D 2008 *Acta Mater.* **56** 3914
- [34] Kalidindi S R, Bronkhorst C A and Anand L 1992 *J. Mech. Phys. Solids* **40** 537
- [35] Kalidindi S R 2004 *Continuum Scale Simulation of Engineering Materials* ed D Raabe *et al* (Berlin: Wiley-VCH) p 529
- [36] Roters F, Eisenlohr P, Hantcherli L, Tjahjanto D D, Bieler T R and Raabe D 2010 *Acta Mater.* **58** 1152
- [37] Brown S B, Kim K H and Anand L 1989 *Int. J. Plast.* **5** 95
- [38] Eisenlohr P and Roters F 2008 *Comput. Mater. Sci.* **42** 670
- [39] Li S, Van Houtte P and Kalidindi S R 2004 *Modeling Simul. Mater. Sci. Eng.* **12** 845
- [40] Press W H, Teukolsky S A, Vetterling W T and Flannery B P 1986 *Numerical Recipes* (Cambridge: Cambridge University Press)
- [41] Engler O 2002 *Adv. Eng. Mater.* **4** 181
- [42] Raabe D, Zhao Z, Park S-J and Roters F 2002 *Acta Mater.* **50** 421
- [43] Raabe D, Zhao Z and Mao W 2002 *Acta Mater.* **50** 4379
- [44] Eisenlohr P, Tjahjanto D D, Hochrainer T, Roters F and Raabe D 2009 *Int. J. Mater. Res.* **4** 500
- [45] Raabe D, Sachtleber M, Zhao Z, Roters F and Zaeferrer S 2001 *Acta Mater.* **49** 3433
- [46] Hölscher M, Raabe D and Lücke K 1994 *Acta Mater.* **42** 879
- [47] Raabe D, Zhao Z and Roters F 2004 *Scr. Mater.* **50** 1085

Microstructure-based Description of the Deformation of Metals: Theory and Application

Dirk Helm, Alexander Butz, Dierk Raabe, and Peter Gumbsch

Aiming for an integrated approach to computational materials engineering in an industrial context poses big challenges in the development of suitable materials descriptions for the different steps along the processing chain. The first key component is to correctly describe the microstructural changes during the thermal and mechanical processing of the base material into a semi-finished product. Explicit representations of the microstructure are most suitable there. The final processing steps and particularly component assessment then has to describe the entire component which requires homogenized continuum mechanical representations. A key challenge is the step in between, the determination of the (macroscopic) materials descriptions from microscopic structures. This article describes methods to include microstructure into descriptions of the deformation of metal, and demonstrates the central steps of the simulation along the processing chain of an automotive component manufactured from a dual phase steel.

INTRODUCTION

Industrial success in materials related technologies relies on the possibility to specifically engineer materials and products with improved performance. The key success factor is the ability to make these developments timely and at relatively low cost. This demands not only the rapid development of new or improved processing techniques but also better understanding and control of material structure, performance, and durability. Such control of materials involves multiple length and time scales and multiple processing stages or the coupling of processing and performance assessment. To achieve this,

How would you...

...describe the overall significance of this paper?

The paper gives an overview of different strategies to include the polycrystalline microstructure into the description of the deformation of metals. It discusses the integration of results from computational multi scale materials engineering into practical industrial applications. A process chain simulation of sheet metal components is used to illustrate the current state of the art.

...describe this work to a materials science and engineering professional with no experience in your technical specialty?

In this paper, numerical approaches are discussed to represent the microstructure evolution and the resulting effective properties of polycrystals and multiphase metallic materials. The results of the micro scale simulations are used to numerically model the process chain of a sheet metal component under consideration of the results from the previous process step.

...describe this work to a layperson?

The article describes different simulation methods to predict the evolution of the material properties of metals due thermal or mechanical processing. This knowledge is of high importance since this change of material properties typically occurs during the different process steps from a semi-finished part to the final component. Providing appropriate simulation tools allows virtually to develop and optimize the production process and to reduce cost and time consuming "trial and error" test. This simulation approach is illustrated for the production process of a sheet metal component for application in automotive industry.

the materials descriptions and the flow of information necessarily have to be based on materials microstructure characteristics. Such inclusion of materials specifics in engineering simulation still is one of the major challenges for the development of improved materials modeling and simulation.^{1,2}

The linkage between materials microstructure and materials properties is at the heart of materials modeling in general but very specifically so for the description of materials deformation. Multiscale approaches (Figure 1) are required to make the link from the discrete dislocations, grain and phase boundaries which constitute the materials microstructure, to the continuum plasticity descriptions appropriate at larger scales. While it may certainly be appropriate to investigate micro-components directly at the level of discrete defects, like the dislocation dynamics investigations of thin films,^{3,4} micro-pillars⁵ or micro-bending bars,⁶ large scale components mandate the final treatment of the component in a continuum mechanical framework.⁷ Although there have been many attempts to include the discrete dislocation behavior rigorously in continuum mechanical materials modeling,⁸ the mathematical frame for such inclusion has only recently been developed^{9,10} and is still far from being applicable. Consequently, the materials models are either effective materials descriptions or have come to be physically based to at least include some direct microstructural information. Similarly it is neither desirable nor intended to include the grain or phase morphology of a material explicitly in the materials modeling at large scale. One therefore either uses effective representations of texture or homogenization techniques to arrive

at continuum mechanical models. The first part of this manuscript describes these different modeling techniques for the continuum mechanical modeling of plastic deformation in single and polycrystalline materials.

In the second part of this manuscript, the applicability of modern microstructure-based modeling in industrial forming simulations is assessed.¹¹ The drive toward microstructure-based models comes, on one hand, from process simulation and the optimization of individual processing steps or the entire processing chain during manufacturing and, on the other hand, from the requirement of higher precision in the simulation of component manufacturing and component assessment. Figure 2 pictorially displays such a processing chain and the final component assessment.

Today, microstructure-based simulations are used, for example, in the process simulation of semi-finished parts in the aluminum industry.¹² This aids process optimization and the specific adjustment of materials properties of the sheet material. For aluminum, alloy development and the individual processes determining the microstructure are reasonably well understood and modeling is developed to a relatively high level.¹³ Other materials, and particularly the steels, are less well understood and detailed microstructural modeling is still rare. This is in part due to the many complex phase transformation phenomena and kinetic pathways involved.^{14,15} In the overall component design, which involves an assessment of the crash worthiness of automotive components, or even the shape, springback or property predictions of components out of the deep drawing and stretching steps, microstructural modeling is basically not yet employed. However, the perspectives for microstructure-based modeling in this field are great. It can, for example, correctly represent the anisotropic yield surface and its non-uniform evolution during deep drawing and thereby not only enable much more precise prediction of the local properties of a component but also allow for integrated product optimization through the entire process chain. As an application example of such integral materials modeling

we report here simulations of the final steps in the processing chain of a dual phase carbon manganese steel sheet, which is intended for use in automotive components.

CRYSTAL PLASTICITY

During the last decades, extensive experimental investigations on single crystals and the evolved physical knowledge about the occurring deformation mechanisms in metals has stimulated the development of appropriate constitutive theories in the framework of continuum mechanics. The continuum mechanical representation is restricted to suitable problems but at the same time the best way to represent certain parts of a complex process chain. An important ingredient when aiming at through-process models is the use of internal variable constitutive formulations that are capable of tracking history dependent behavior. Typical internal variables are dislocation density, grain size, and second phase dispersion. The use of external variables (such as strain) cannot describe inheritance of microstructures through a sequence of processes.

Finite Strain Single Crystal Plasticity

Kinematics

The kinematics of finite deformation¹⁶ describes a situation where a material point that is originally in a reference configuration is deformed to the current state by a combination of externally applied forces. The local changes in space are given by the deformation gradient, which transforms tangent vectors on material lines from the reference configuration in tangent vectors of material lines in the current configuration (Figure 3). In order to distinguish between elastic and plastic deformations, the idea of Kröner¹⁷⁻¹⁹ to incorporate a multiplicative decomposition of the deformation gradient into an elastic and plastic part is nowadays well established: The elastic part results from the reversible response of the lattice to external loads and displacements including rigid-body rotations while the plastic part of the deformation gradient is an irreversible permanent deformation that persists when all external forces and displacements

are removed. In this sense, transformation of the reference state by the plastic part of the deformation gradient leads to an intermediate configuration which is free from external stresses and which is generally considered to maintain a perfect lattice (Figure 4). The velocity of each material point of a body in motion forms a vector field measured in the current state. The spatial gradient of this velocity field describes the change in time of tangent vectors on material lines in the current configuration. The previously introduced multiplicative decomposition of the deformation gradient leads to an additive decomposition of the spatial velocity gradient into an elastic and plastic part. In general, the plastic part is influenced by elastic deformations. However, if the velocity gradient is expressed on the intermediate configuration, the resulting plastic part depends only on plastic deformations.

In the case of dislocation slip, the plastic part of the deformation gradient on the isoclinic intermediate configuration can be formulated as sum of the shear rates on all slip systems. The idea behind the isoclinic intermediate configuration is that the slip vectors and the normal vectors have the same orientation in the reference configuration and the intermediate configuration. Consequently, the rotational part of the plastic part of the deformation gradient is fixed and therefore only the push forward to the current configuration leads to changes in the orientation of the material substructure in form of the crystal lattice (Figure 4).

In addition to the dislocation slip, mechanically driven displacive transformations (i.e., twinning and martensitic phase transitions) play an important role in many metals (magnesium, titanium, modern steel grades like TRIP- and TWIP-steels, etc.). In general, there are several ways to incorporate the displacive transformations in the kinematics of crystal plasticity. The displacive transformations are incorporated in the form of additional slip systems²⁰⁻²³ or by using a multiple multiplicative decomposition of the deformation gradient,^{23,24} which consists of an elastic and plastic part and an additional part for representing the transition. Due to this, an additional intermediate configura-

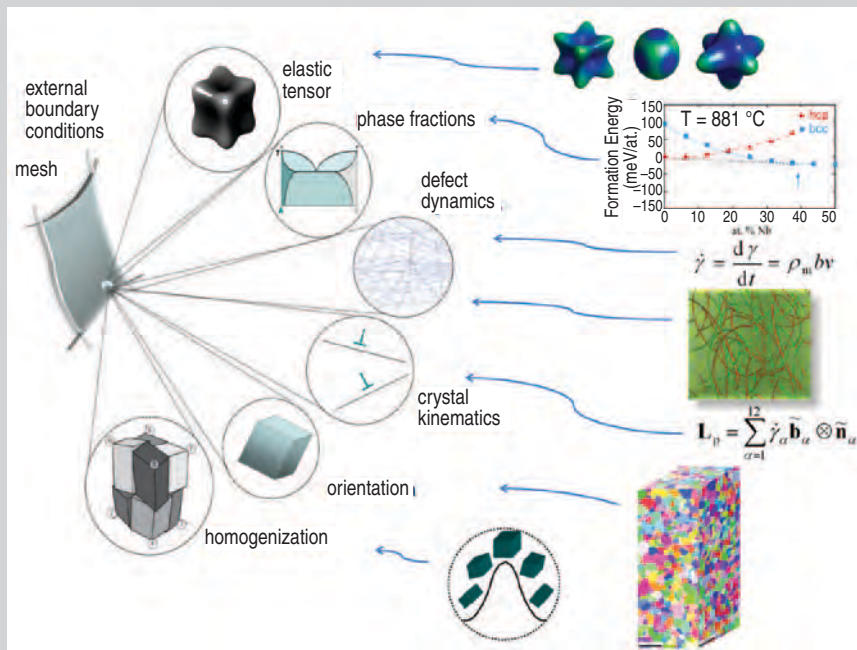


Figure 1. Scheme of a continuum mechanical framework for polycrystal-polyphase mechanics with various ingredients describing the material behavior indicating various options for choosing the adequate degree of microstructure coarse graining and homogenization.

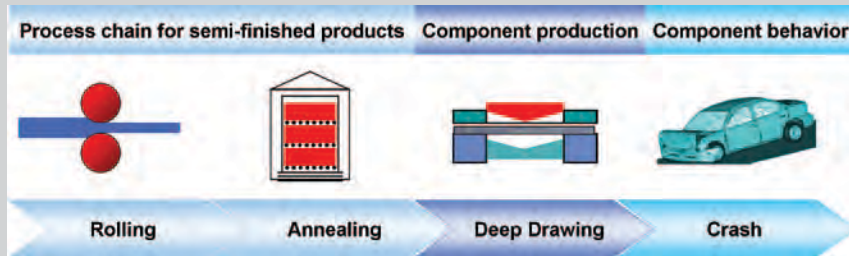


Figure 2. Process chain from the hot rolled sheet to the crashed part.

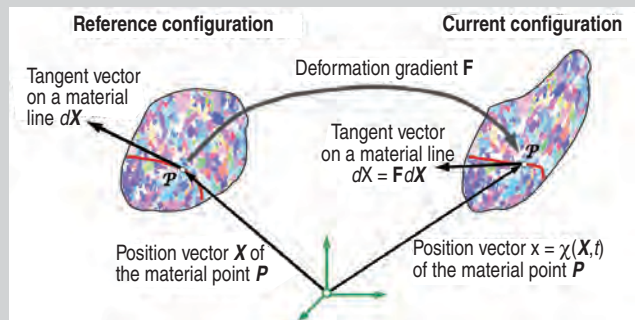


Figure 3. Representing finite deformations in the framework of continuum mechanics.

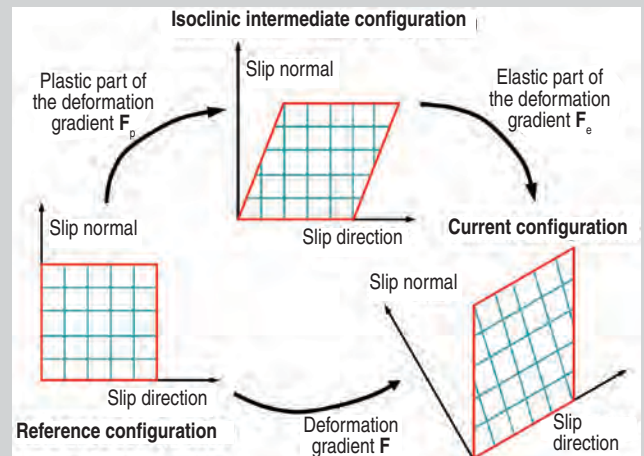


Figure 4. Representing finite plastic deformations by means of a multiplicative decomposition of the deformation gradient.

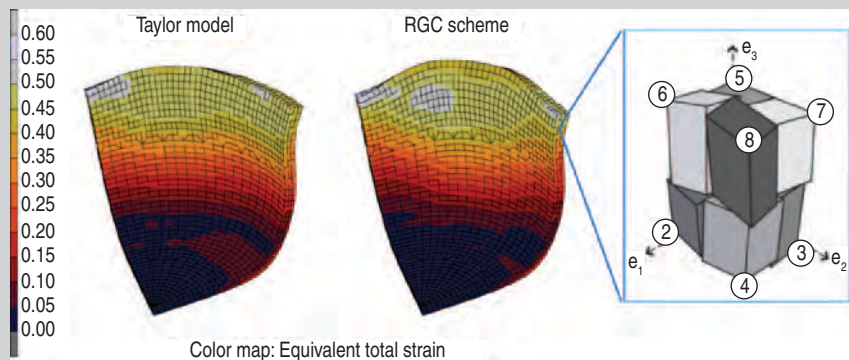


Figure 5. Right hand side: Example of a grain-cluster approximation (RGC⁵⁶) where the constraints are placed on the corners of the aggregate while internal relaxations are admitted; left hand side: two simulation runs using two different homogenization models. (Photo courtesy of D. Tjahjanto)

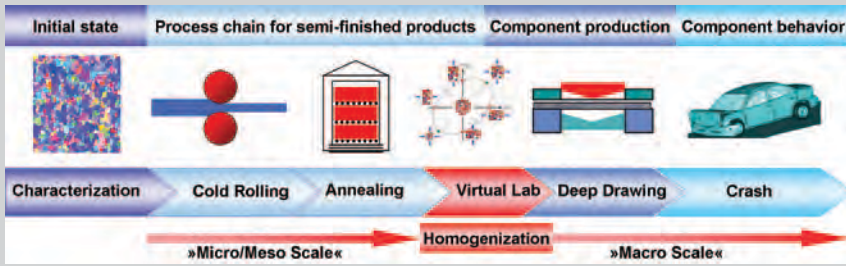


Figure 6. Modeling strategy for representing the process chain for sheet metal production.

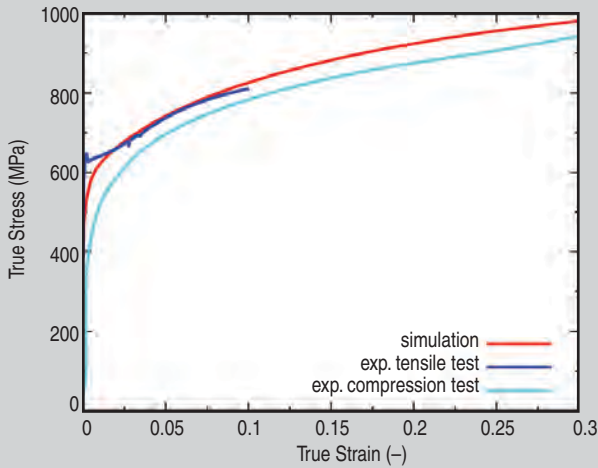


Figure 7. Tensile test on the hot rolled sheet. Comparison between experimental data and the calibrated microstructure model.

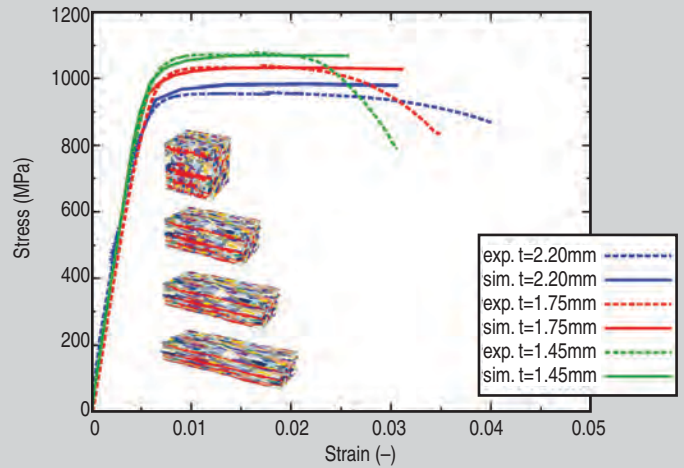


Figure 8. Tensile tests on the (hard, as rolled) cold rolled sheet (hard as rolled) for different degrees of rolling. The initial thickness of the hot rolled sheet is 3.5 mm.

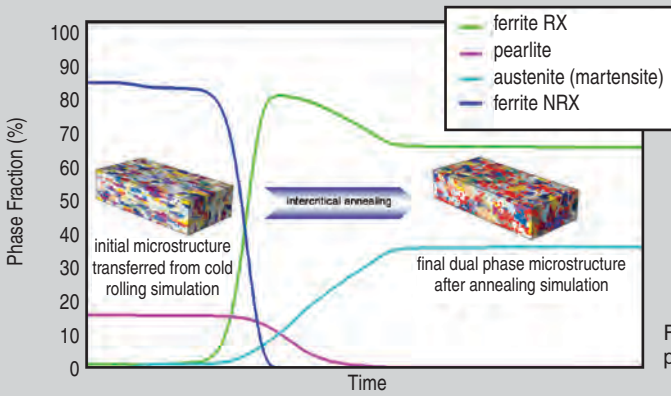


Figure 9. Simulation of the microstructure evolution during the annealing procedure.

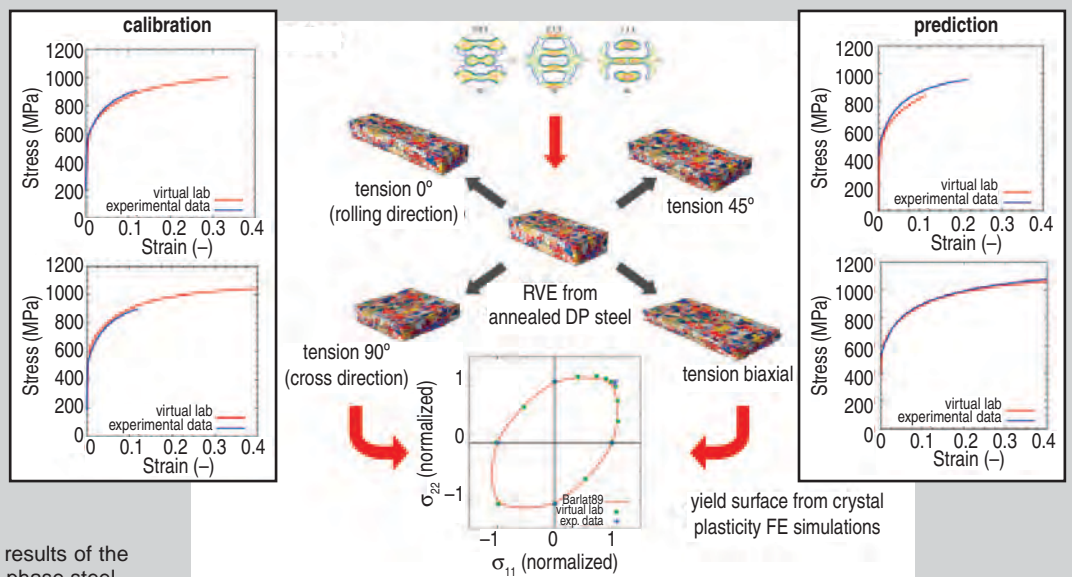


Figure 10. Application and results of the virtual laboratory on a dual phase steel.

tion arises.

Finally, it is worth mentioning that the sketched kinematic relations for representing the plastic deformations are identical for both phenomenological and physical based models.

Phenomenological Constitutive Models

Based on the kinematical relations for modeling the main deformation mechanisms in metals, different types of phenomenological models for representing crystal plasticity can be introduced. The most important constituents are the elasticity relation, the constitutive equations for representing the kinetic of slip or transition processes and the hardening behavior.

The anisotropic elastic behavior of crystalline structures can be incorporated by hypoelasticity,²⁵ Cauchy elasticity,^{21,26} or hyperelasticity.¹⁶ As long as the elasticity relation does not possess a strain energy function, as in the case of many hypoelastic formulations, it has been well discussed in the literature²⁷ that energy dissipation occur if closed cycles of deformation are considered. This is a strong disadvantage of such elasticity relations.

So far, the kinematic relation (Figure 4) describes only the geometrical aspects of the evolving plastic anisotropy. In addition, the kinetic of the plastic deformation on the glide systems (i.e., the shear or slip rate) must be defined. Due to the physical understanding, the shear rate on a slip system depends mainly on the resolved shear stress on the slip system and is often influenced by deformation rates. For representing the slip and in particular the slip rate,²⁸ concepts in the framework of viscoplasticity with yield limit^{16,29} and without yield limit,^{25,30} has been proposed and applied. In contrast to rate-independent plasticity models, the current yield point is influenced by the deformation rate.²⁸ Independent on which formulation is preferred, the relation between the resolved shear stress on the slip system in relation to the critical stress is the most important quantity for the amount of plastic slip.

In phenomenological theories, the evolution of the critical resolved shear stress is modeled by means of history dependent internal variables. Mostly, the strain hardening behavior is rep-

resented as a function depending on the accumulated slip.^{25,31} While this allows for the description of fundamental hardening phenomena including tension-compression asymmetries in basal textured magnesium alloys by means of a suitable twinning model,²⁰ the modeling of some anisotropic hardening phenomena like the Bauschinger effect requires additional internal variables, i.e. back stresses on the slip system.^{16,29,32}

The deformation of metals depends strongly on temperature and is accompanied by dissipation phenomena. From this point of view, modeling in the framework of continuum thermodynamics leads to valuable insights. In such thermodynamic frameworks,^{16,24,29,33} the energy storage phenomena are modeled by using a thermodynamic potential like a free energy function, which depends on the temperature, the elastic part of the deformation gradient, and internal variables. The evaluation of the Second Law of Thermodynamics leads to potential relations for the stress tensor and the entropy as well as a remaining dissipation inequality, which must be fulfilled by the evolution equations for the internal variables. For example, an important consequence of such finite strain thermodynamic considerations is that the projection of the Mandel stress tensor¹⁸ on the glide system in the isoclinic intermediate configuration is the driving stress for occurring slip.

Physically Based Models

In contrast to conventional viscoplastic hardening models, physically based constitutive formulations use internal variables that describe the material state and its history in terms of microstructure parameters. In the case of plasticity the most relevant microstructural state variable is the dislocation density.

When using dislocation-density based constitutive models, the individual shear rates on each glide system, expressed by the plastic part of the velocity gradient tensor, are coupled via the Orowan equation to the underlying density of mobile dislocations that carry this shear rate. The evolution of the total dislocation density (including both, mobile and immobile disloca-

tions) is described through a set of rate formulations that quantify annihilation, multiplication, immobilization, and mobilization events on each individual slip system in a statistical manner. Depending on the specific model design different types of dislocation classes can be defined together with their respective evolution equations and activation barriers reflecting the underlying dislocation processes. Typical examples are the use of edge versus screw dislocation kinetics or the use of dislocations in cell walls and in cell interiors. Details about such formulations and comparisons with experiments can be found in References 23 and 34.

Further parameters for characterizing the microstructure are for instance the grain size, second phase fractions, and precipitates. Some of these parameters (grain size, precipitates) can enter for instance into the mean free path equation for the mobile dislocations or as constants that quantify the increase in friction stress as a function of composition (solute). Alternatively, grains can be treated individually, where each grain is represented by a set of integration points of identical initial crystal orientation.

High second phase fractions above about 10 vol.% can be considered either in form of a full-field approximation where different phases occupy different finite elements or in an averaged form where the stress response from a two-phase assembly at one integration point is calculated by a separate homogenization model.

The use of physically based models is particularly relevant for precise stress, shape, and texture predictions for forming at small scales,³⁵⁻³⁷ under complex loading paths, for damage initiation,³⁸ for Bauschinger effects,^{39,40} and for the behavior of instable texture components.⁴¹ Fine details of the constitutive laws are less essential for simulating large scale forming problems with simple loading paths and microstructure history.

Representing the Behavior of Polycrystals

Polycrystalline and also multiphase metallic materials are of particular interest in technical applications. In this situation, the inhomogeneity in the

microstructure due to texture, precipitations, different phases, etc. requires suitable homogenization schemes for the transition from single crystals to polycrystals.

Mean-field Methods

A reasonable way to obtain the effective properties of a material is given by homogenization schemes on the basis of simplified assumptions about the material behavior and the morphology of the microstructure. In such mean-field approaches the microstructure can be considered as a system of an inclusion that is embedded in a matrix. The most basic assumptions would be either uniform stress or uniform deformation gradient among all phases or respectively grains present in the microstructure. These cases were suggested by Reuss⁴² and Voigt⁴³ for elasticity. The fully constrained Taylor⁴⁴ model for plasticity or the extension of Lin⁴⁵ for elasto-plasticity correspond to the uniform strain assumption. Both assumptions ignore the shape and specific local neighborhood of the inclusions and generally violate strain compatibility and stress equilibrium, respectively. More sophisticated mean-field assumptions make use of the Eshelby-solution⁴⁶ to the problem of an elastic ellipsoidal inclusion in an infinite elastic matrix.

Out of those, the most frequently employed are the self-consistent approach originally suggested by Kröner,⁴⁷ and the scheme introduced by Mori and Tanaka.⁴⁸ In the former method, each inclusion is treated as isolated within a matrix having the unknown integral stiffness of the compound. The latter approach embeds each inclusion into the original matrix but considers the average matrix strain to act as far-field strain on the overall composite. However, extension of such homogenization schemes from the linear to the non-linear case faces difficulties, most significantly because the stiffness (i.e., strain(rate)-sensitivity of stress) is typically inhomogeneous for a given phase due to its heterogeneous strain. The stiffnesses are usually homogenized by using the average strain per phase as a reference input into the respective constitutive law. In order to establish a link between stress and strain per

phase, secant (connecting total stress to total strain) and tangent (connecting stress increments to strain increments) formulations for the moduli are employed.⁴⁹ As an example, the viscoplastic self-consistent mean-field approach (VPSC) has been successfully applied to represent the texture evolution in different types of polycrystalline metals: zirconium alloys,⁴⁹ TWIP-steels,⁵⁰ and tungsten.⁵¹ Recent developments incorporate elasticity in the model⁵² enabling a more accurate description of the material behavior.

An alternative set of mean-field polycrystal approaches are the grain-cluster models. They represent an intermediate approach between the mean-field schemes and full-field solutions. They reduce the high computational cost of the latter by restricting the degrees of freedom to a small number of regions with (typically) homogeneous strain inside each region. Those areas are grains or phase, thus extending the mean-field approaches by taking into account direct neighbor-neighbor interactions among the constituents of a polycrystalline and potentially also multiphase aggregate. The introduction of grain aggregates allows relaxation of the assumption of homogeneous strain in each constituent (Taylor)—which generally led to an overestimation of the polycrystalline strength and rate of texture evolution—by enforcing compatibility only in an average sense for the aggregate as a whole. Typical examples of such models were suggested by Van Houtte,^{53,54} Gottstein,⁵⁵ and Eisenlohr⁵⁶ (Figure 5). The reasonable numerical effort for solving mean-field problems enables the coupling of the homogenization schemes in finite element algorithm,^{7,56-58} for solving more complex initial boundary value problems like the deep drawing of a cup (see Figure 5) or study the texture evolution during rolling.⁵⁷

Full-field Methods

Full-field models of crystal mechanics pursue strategies for solving initial boundary value problems of polycrystalline unit cells. In contrast to the mean-field methods, full-field methods provide a more realistic representation of the stress and strain state in each grain and also the accompanied gradi-

ents, along with an accurate description of the grain morphology, an improved quantitative description of the texture, and a reasonable representation of the interaction between the considered constituents (i.e., grains, phases, etc.). Most of the current numerical treatments of the full-field homogenization schemes are based on the finite element method. Examples on this approach were given by References 29, 59–61 for material science applications as well as References 22 and 62 for simplified bulk metal forming processes like rolling and wire drawing. Without appropriate strategies such full-field approximations are usually too time consuming for applications in through-process modeling. To remedy this problem fast Fourier transform (FFT) based methods can be applied.⁶³ In comparison to the high computational demand of FE based methods, FFT based full-field solutions require much less computer times.⁶⁴

APPLICATION OF MULTISCALE MODELS FOR SOLVING ENGINEERING PROBLEMS

Virtual Laboratory

In the industrial practice of simulating complex forming operations, the prediction of exact shapes, material flow, thinning, wrinkling, earing, and springback effects is a challenge, particularly when materials with complex textures and microstructures are involved. In the simulation packages that are currently in commercial use, for instance, in the automotive industry, only empirical constitutive laws are available. As these formulations provide only limited empirical access to the material anisotropy and heterogeneity they do not properly take into account the effects of microstructure and texture and their evolution during deformation. The crystal plasticity finite element method (CPFEM) bridges the gap between the polycrystalline texture and macroscopic mechanical properties and opens the path to a more profound consideration of metal anisotropy in commercial forming and process simulations.

The example presented in this section is an application of the CPFE method for the concept of virtual mate-

rial testing (virtual laboratory) using a representative volume element (RVE) approach. By using such numerical test protocols it becomes possible to determine the actual shape of the yield locus as well as corresponding anisotropy coefficients (i.e., Lankford parameters, r -values) directly through CPFЕ simulations, and to use this information to calibrate empirical constitutive models used, for example, in the automotive industry. Along with standard uniaxial tensile tests, other strain paths can be simulated, such as biaxial tensile, compressive or shear tests. The analysis of loading condition which can not be realized experimentally (like biaxial compression of sheet metal) is also of interest to extend the experimental available data. For practical application, the homogenized results obtained from the virtual lab can be processed in the same manner as conventional experimental results. In the present example the use of the CPFЕ method for virtual testing is demonstrated for a dual-phase C-Mn steel grade where the parameters of an empirical yield surface function were calibrated by the full-field crystal plasticity predictions (Figure 10).

Representation of Process Chains

While simulation solutions for single process steps are applied successfully to virtually study the ability to process or service parts, a unified approach that reuses knowledge and results from previous steps along the production chain is still an exception. Especially the gap between numerical steel design and corresponding simulation techniques in sheet metal forming and crash simulation is a challenging topic for industrial applications.

In this example,⁶⁵ a process chain simulation is presented that covers the consecutive stages of production of a dual phase steel DP800 material. It starts with the hot rolled strip which is followed by cold rolling, heat treatment, deep drawing and finally the analysis of the crashworthiness of the deep drawn component. An important aspect to take into account is the microstructure evolution during the different process steps for an appropriate modeling of the material behavior.

Depending on the process step, different simulation strategies on different length scales are applied (Figure 6).

The first process step to be simulated is cold rolling. Here, a full field simulation approach (RVE) in combination with a CPFЕ model is used. Different experimental analysis procedures were carried out to account for the initial state of the hot rolled sheet material. Micrographs were used to analyze the ferritic-pearlitic microstructure. To obtain a realistic distribution of the pearlite phase within the ferrite matrix, a statistical reconstruction scheme based on Reference 66 was applied. EBSD data are used to consider a realistic initial texture. Finally, the parameters of the single crystal plasticity material model are calibrated using macroscopic tensile and compression tests (Figure 7).

A prescribed deformation was applied on the RVE-model to simulate the cold rolling process. Three different degrees of rolling were considered with final sheet thicknesses of 2.20, 1.75 and 1.45 mm. According to real tensile test on the as rolled material, similar virtual tests were performed on the rolled RVE-models. Figure 8 shows the very good agreement between the tensile test and the prediction of the model. The hardening behavior can be predicted independently from the applied deformation.

During the subsequent thermal treatment the final dual phase steel microstructure composed of ferrite and martensite is obtained. The corresponding simulation (Figure 9) aim at describing the microstructure change (phase transition, recrystallization and recovery) due to the annealing procedure. The simulation of the thermal treatment is carried out by a cellular automaton.⁶⁷ The morphology of the cold rolled RVE model is mapped onto a regular grid. Data concerning the grain number, the orientation of the crystal lattice and the accumulated plastic strain were provided from the rolling simulation to define the initial state for the annealing simulation. The accumulated plastic strain is used to estimate the dislocation density which acts as a driving force within the annealing simulation.

For practical application of deep drawing simulations, models which directly consider the microstructure are

not appropriate due to the high numerical cost and the complexity of the material description. Usually, deep drawing simulations are continuum-based which describe the yielding and hardening behavior with phenomenological models. For this reason, the obtained data from the annealing simulation were homogenized using the virtual lab as described in the preceding section. The obtained macroscopic uniaxial stress-strain curves are used—similar to experimental data—to adjust the parameter of the phenomenological plasticity models. Here, the Barlat89⁶⁸ yield function is applied to describe the initial yielding of the dual phase steel. In Figure 10 this procedure is illustrated. The yield points obtained from the virtual lab and the Barlat89 yield locus which is calculated from experimental data do agree very well. Depending of the number of virtual tests, more complex yield functions with more parameter can also be fitted. After the determination of the material behavior by means of the virtual laboratory, the resulting material parameters are used to calibrate macroscopic models for complex deep drawing simulation.⁶⁹

Finally, the crashworthiness of the deep drawn component is virtually analyzed. To obtain accurate failure predictions, the load history from the previous deep drawing process is considered. Therefore, the local thinning of the sheet and the actual hardening of the material at the end of the deep drawing simulation is mapped to the crash simulation.⁷⁰

CONCLUSIONS

From an initial microstructure, the cold rolling of the initial ferritic-pearlitic microstructure of a C-Mn steel sheet was evolved in a CPFЕ simulation to give the texture changes and a grain-specific deformation. This information was sufficient to feed the simulation of the recrystallization processes during heat treatment. With the dual phase microstructure after recrystallization, virtual testing of the deformation behavior was performed. This required two simple calibration experiments but then nicely predicted multiaxial deformation behavior. In the subsequent deep drawing and crash simulations one then has access to local changes in

the mechanical properties of a component, which goes far beyond classical component analysis.

On the basis of appropriate numerical treatments, the discussed constitutive theories are able to represent the microstructure evolution and the resulting effective properties of complex polycrystalline and also multiphase metallic materials. This results in a deeper insight into the process and the interactions between the process steps. This knowledge will help to optimize individual process steps and also to improve the complete process chain. Once established, the modeling along the processing chain allows for both virtual process development and component assessment in unprecedented detail and with unprecedented precision.

ACKNOWLEDGEMENTS

Financial support from the German Ministry for Education and Research (BMBF Grant 03X0501) and joint support by the Fraunhofer and Max Planck Societies is gratefully acknowledged.

References

1. P. Gumbsch, in *Handbook of Materials Modeling*, ed. S. Yip (Dordrecht, Netherlands: Springer Verlag, 2005), pp. 2713–2718.
2. D. Raabe, F. Roters, F. Barlat, and L.-Q. Chen, editors, *Continuum Scale Simulation of Engineering Materials: Fundamentals–Microstructures–Process Applications* (Weinheim, Germany: Wiley-VCH, 2004).
3. G. Dehm, T.J. Balk, B. Von Blanckenhagen, P. Gumbsch, and E. Arzt, *Zeitschrift für Metallkunde*, 93 (2002), pp. 383–391.
4. B. Von Blanckenhagen, E. Arzt, and P. Gumbsch, *Acta Materialia*, 52 (2004), pp. 773–784.
5. J. Senger, D. Weygand, P. Gumbsch, and O. Kraft, *Scripta Materialia*, 58 (2008), pp. 587–590.
6. C. Motz, D. Weygand, J. Senger, and P. Gumbsch, *Acta Materialia*, 56 (2008), pp. 1942–1955.
7. D. Raabe and F. Roters, *Intern. J. Plast.*, 20 (2004), pp. 339–361.
8. E. Kröner, *Int. J. Solids and Structures*, 38 (2001), pp. 1115–1134.
9. T. Hochrainer, M. Zaiser, and P. Gumbsch, *Philosophical Magazine*, 87 (2007), pp. 1261–1282.
10. S. Sandfeld, T. Hochrainer, P. Gumbsch, and M. Zaiser, *Philosophical Magazine*, 90 (2010), pp. 3697–3728.
11. D. Raabe, P. Klose, B. Engl, K.-P. Imlau, F. Friedel, and F. Roters, *Adv. Eng. Mater.*, 4 (2002), pp. 169–180.
12. O. Engler and J. Hirsch, *Mat. Sci. Eng. A*, 336 (2002), pp. 249–262.
13. L. Neumann, R. Kopp, A. Ludwig, M. Wu, A. Bührig-Polaczek, M. Schneider, M. Crumbach, and G. Gottstein, *Mater. Sci. Eng.*, 12 (2004), pp. S19–S31.
14. N. Peranio, Y.J. Li, F. Roters, and D. Raabe, *Mater. Sci. Eng. A*, 527 (2010), pp. 4161–4168.
15. R. Song, D. Ponge, D. Raabe, J.G. Speer, and D.K. Matlock, *Mater. Sci. Eng. A*, 441 (2006), pp. 1–17.
16. P. Haupt, *Continuum Mechanics and Theory of Materials* (Berlin: Springer, 2002).
17. E. Kröner, “Allgemeine Kontinuumstheorie der Versetzungen und Eigenspannungen,” *Archive for Rational Mechanics and Analysis*, 4 (1959), pp. 273–334.
18. J. Mandel, “Plasticité Classique et Viscoplasticité,” CISM Course Vol. 97 (1971).
19. E. Lee and D. Liu, *J. Applied Physics*, 38 (1967), pp. 19–27.
20. A. Staroselsky and L. Anand, *Int. J. Plasticity*, 19 (2003), pp. 1843–1864.
21. S.R. Kalidindi, *J. Mechanics and Physics of Solids*, 46 (1998), pp. 267–271.
22. A. Prakash, S.M. Weygand, and H. Riedel, *Computational Materials Science*, 45 (3) (2009), pp. 744–750.
23. F. Roters, P. Eisenlohr, L. Hantcherli, D.D. Tjahjanto, T.R. Bieler, and D. Raabe, *Acta Mater.*, 58 (2010), pp. 1152–1211.
24. S. Turteltaub and A.S.J. Suiker, *J. Mechanics and Physics of Solids*, 53 (2005), pp. 1747–1788.
25. R.J. Asaro, in *Advances in Applied Mechanics Volume 23*, ed. John W. Hutchinson and Theodore Y. Wu (Amsterdam, the Netherlands: Elsevier, 1983), pp. 1–115.
26. A. Ma, F. Roters, and D. Raabe, *Acta Mater.*, 54 (2006), pp. 2169–2179.
27. J. Lubliner, *Plasticity Theory* (New York: Macmillan Publishing, 1990).
28. J.R. Rice, *J. Applied Mechanics*, 37 (1970), p. 728.
29. G. Cailleaud, O. Diard, F. Feyel, and S. Forest, *Technische Mechanik*, 23 (2003), pp. 130–145.
30. J.W. Hutchinson, *Proc. R. Soc. Lond. A*, 10 (348) (1976), pp. 101–127.
31. E. Voce, *J. Inst. Met.*, 74 (1948), pp. 537–562.
32. J. Harder, *Int. J. Plasticity*, 15 (1999), pp. 605–624.
33. M.E. Gurtin, *J. Mechanics and Physics of Solids*, 48 (2000), pp. 989–1036.
34. A. Ma, F. Roters, and D. Raabe, *Acta Mater.*, 54 (2006), pp. 2181–2194.
35. Z. Zhao, M. Ramesh, D. Raabe, A. Cuitino, and R. Radovitzky, *Int. J. Plast.*, 24 (2008), pp. 2278–2297.
36. F. Siska, S. Forest, and P. Gumbsch, *Computational Materials Science*, 39 (2007), pp. 137–141.
37. F. Siska, D. Weygand, S. Forest, and P. Gumbsch, *Computational Materials Science*, 45 (2009), pp. 793–799.
38. T.R. Bieler, P. Eisenlohr, F. Roters, D. Kumar, D.E. Mason, M.A. Crimp, and D. Raabe, *Int. J. Plast.*, 25 (2009), pp. 1655–1683.
39. E. Demir and D. Raabe, *Acta Mater.*, 58 (2010), pp. 6055–6063.
40. T. Walde, P. Gumbsch, and H. Riedel, *Steel Research International*, 77 (2006), pp. 741–746.
41. D. Raabe, Z. Zhao, S.-J. Park, and F. Roters, *Acta Mater.*, 50 (2002), pp. 421–440.
42. A. Reuss, *Z. Angew. Math. Mech.*, 9 (1929), pp. 49–58.
43. W. Voigt, *Wied. Ann.*, 38 (1889), pp. 573–587.
44. G.L. Taylor, *J. Inst. Met.*, 62 (1938), pp. 307–324.
45. T.H. Lin, *J. Mechanics and Physics of Solids*, 5 (1957), pp. 143–149.
46. J.D. Eshelby, *Proc. Roy. Soc. Lond. A*, 241 (1957), pp. 376–396.
47. E. Kröner, *Z. Phys.*, 151 (1958), pp. 504–518.
48. T. Mori and K. Tanaka, *Acta Metall.*, 21 (1973), pp. 571–574.
49. R.A. Lebensohn and C.N. Tomé, *Acta Metall. et Mater.*, 41 (1993), pp. 2611–2624.
50. A. Prakash, T. Hochrainer, E. Reissacher, and H. Riedel, *Steel Research International*, 79 (2008), pp. 645–652.
51. M. Rodriguez Ripoll, E. Reissacher, and H. Riedel, *Computational Materials Science*, 45 (2009), pp. 788–792.
52. H. Wang, P.D. Wu, C.N. Tomé, and Y. Huang, *J. Mechanics and Physics of Solids*, 58 (2010), pp. 594–612.
53. P. Van Houtte, L. Delannay, and I. Samajdar, *Texture Microstruct.*, 31 (1999), pp. 109–149.
54. P. Van Houtte, S. Li, M. Seefeldt, and L. Delannay, *Int. J. Plast.*, 21 (2005), pp. 589–624.
55. C. Schäfer, J. Song, and G. Gottstein, *Acta Mater.*, 57 (2009), pp. 1026–1034.
56. P. Eisenlohr, D.D. Tjahjanto, T. Hochrainer, F. Roters, and D. Raabe, *Int. J. Materials Research*, 100 (2009), pp. 500–509.
57. T. Walde and H. Riedel, *Mater. Sci. and Eng. A*, 443 (2007), pp. 277–284.
58. I. Tikhovskiy, D. Raabe, and F. Roters, *Mater. Sci. Eng. A*, 488 (2008), pp. 482–490.
59. D. Raabe, M. Sachtleber, Z. Zhao, F. Roters, and S. Zaefferer, *Acta Mater.*, 49 (2001), pp. 3433–3441.
60. A.J. Beaudoin, H. Mecking, and U.F. Kocks, *Philos. Mag. A*, 73 (1996), pp. 1503–1517.
61. M. Sachtleber, Z. Zhao, and D. Raabe, *Mater. Sci. Eng. A*, 336 (2002), pp. 81–87.
62. J. Ocenasek, M. Rodriguez Ripoll, S.M. Weygand, and H. Riedel, *Computational Materials Science*, 39 (2007), pp. 23–28.
63. R.A. Lebensohn, *Acta Mater.*, 49 (2001), pp. 2723–2737.
64. A. Prakash and R.A. Lebensohn, *Model. Sim. Mater. Sci. Eng.*, 17 (2009), 064010.
65. A. Butz, S. Lossau, B. Springub, and F. Roters, *Int. J. Mater. Forming*, 3 (Suppl. 1) (2010), pp. 73–76.
66. C. Yeong and S. Torquato, *Phys. Rev. E*, 57 (1998), pp. 495–506.
67. D. Raabe, *Ann. Rev. Mater. Res.*, 32 (2002), pp. 53–76.
68. F. Barlat and J. Lian, *Int. J. Plasticity*, 5 (1989), pp. 51–56.
69. S. Lossau and B. Svendsen, “Forming Simulations Based on Parameters Obtained in Microstructural Cold Rolling Simulations in Comparison to Conventional Forming Simulations” (Presented at the 7th LS-DYNA User Conference, Salzburg, Austria, 2009), C-1-01.
70. F. Feukamm, M. Feucht, A. Haufe, and K. Roll, *Proc. 7th Int. Conf. Numerical Simulation of 3D Sheet Metal Forming Processes* (Zurich Switzerland: ETH Zurich, Institute of Virtual Metallurgy, 2008), pp. 805–810.

Dirk Helm, Alexander Butz, and Peter Gumbsch are with Fraunhofer Institute for Mechanics of Materials IWM, Wöhlerstr. 11, 79108 Freiburg, Germany; Dierk Raabe is with Max-Planck-Institute for Iron Research, Max-Planck-Str. 1, 40237 Düsseldorf, Germany. Gumbsch is also with the Institute for Applied Materials IAM, Karlsruhe Institute of Technology KIT, Kaiserstraße 12, 6131 Karlsruhe, Germany. Dr. Helm can be reached at dirk.helm@iwm.fraunhofer.de.